Growth and structure of yttrium sesquioxide epitaxial films

by

Scott Elliott Webster

M.A.Sc., The University of British Columbia, 2005
B.Sc.E., Queen's University, 2002

A THESIS SUBMITTED IN PARTIAL FULFILLMENT
OF
THE REQUIREMENTS FOR THE DEGREE OF

DOCTOR OF PHILOSOPHY

in

The Faculty of Graduate Studies

(Physics)

THE UNIVERSITY OF BRITISH COLUMBIA

(Vancouver)

March 2012

Abstract

The use of molecular beam epitaxy as a method for producing solid state host crystals for planar waveguide lasers has been investigated. Single crystal yttrium sesquioxide with a very high degree of structural order has been grown on R-plane sapphire substrates.

The $(01\bar{1}2)$ Al_2O_3 substrates were annealed in air at 1150 °C to generate atomically smooth surfaces with parallel atomic steps. This process was important for maximizing structural quality and minimizing surface roughness of the grown Y_2O_3 film. A critical-thickness-like phenomenon was discovered, where the Y_2O_3 would grow in regions with near structural perfection at the beginning of growth. In thicker films, the x-ray diffraction peaks became wider, indicating less crystalline uniformity. The maximum equivalent "critical thickness" achieved was 7 nm for a film grown at 800 °C with a growth rate of 20 nm/hr. The highly ordered material may be present in one uniform layer or distributed in smaller regions throughout the thin film.

Y_2O_3 films on Al_2O_3 were annealed in air at temperatures up to 1400 °C to study interdiffusion. By analyzing x-ray diffraction measurements, we found that Al migrated from the substrate into the Y_2O_3 film with an approximate activation energy for bulk diffusion of 3.0 eV. Diffusion on the Y_2O_3 surface was estimated to have an activation energy of (0.5 ± 0.3) eV from atomic force microscopy images. After annealing, the presence of $Y_4Al_2O_9$, $YAlO_3$, and $Y_3Al_5O_{12}$ phases was confirmed using x-ray diffraction and photoluminescence measurements.

Attempts were made to use molecular hydrogen gas and gallium as surfactants during growth to improve film properties. No conclusive benefit was observed.

Y_2O_3 film surface roughness was observed to increase roughly proportionally to the square root of film thickness. A 600 nm thick waveguide layer grown under optimal conditions had a root-mean-square roughness of 5.8 nm. This level of roughness could cause scattering loss at the waveguide core-cladding interface that is problematic for practical applications.

Preface

Some of the work presented in this thesis has been published previously, as detailed below. The work was done in collaboration with my research supervisor, Dr. Tom Tiedje, who provided significant advice. My research was part of a larger project conducted with my fellow PhD students Raveen Kumaran and Shawn Penson. However, except as described below, the work presented here is my own.

In section 2.1, the scratching of the annealed substrates was performed by Shawn Penson. I was responsible for the remainder of the work in this section. Portions of section 2.4.2 have been previously published in an article titled "Molecular beam epitaxy growth of neodymium-doped yttrium aluminum perovskite" by R. Kumaran, S.E. Webster, S. Penson, Wei Li, and T. Tiedje in the *Journal of Crystal Growth* (Elsevier), **311**:2191–2194, 2009. I created the schematic diagram and performed all of the integrating sphere measurements, which have not been previously published, as well as aided in the preparation of the manuscript.

Wei Li performed the waveguide mode measurements described in section 3.3.2.2. Portions of section 4.1 have also been previously published in an article titled "Structural analysis of thin epitaxial Y_2O_3 films on sapphire" by S.E. Webster, R. Kumaran, S. Penson, and T. Tiedje in the *Journal of Vacuum Science and Technology B* (American Vacuum Society), **28**:C3A20–C3A23, 2010. I performed the work and wrote the manuscript while consulting with my co-authors for advice.

Table of Contents

List of Tables

List of Figures

Acknowledgements

Thanks to all of my fellow mbelab members, past and present. In particular I'd like to thank Raveen Kumaran, Wei Li, and Shawn Penson for many helpful discussions on the oxide MBE project. Thanks to Anders Ballestad and Dan Beaton for sharing an "office" with me, to Eric Nodwell and Kevin Mitchell for computer support, and to Jim Mackenzie for his endless technical expertise.

Thanks to my PhD committee, Joshua Folk, Nicholas Ingle, and David Jones for working through the process with me, and especially to my supervisor Tom Tiedje for innumerable helpful conversations and much advice.

Two free and open source software packages have been particularly useful in my work: Gri, the scientific graphics programming language used to make many of the plots in this thesis (http://gri.sourceforge.net), and Gwyddion, the software used for all the AFM data analysis and figure preparation (http://gwyddion.net). Thanks to the authors and contributors for their work on these programs.

Thanks to Michael Forbes for help with LaTeX formatting and to Iva Cheung for copy editing and stylistic editing of a draft of this thesis. Thanks also to Iva Cheung and Jeff Mottershead for being great friends. Thanks to my parents for not losing touch despite geographical challenges.

Finally, thanks most of all to my family, Anne and Joël Webster, for their love and support, and for keeping me sane throughout my degree.

for Anne

1 Introduction

Research in epitaxial growth of oxides is typically divided into several categories, including oxide semiconductors such as zinc oxide;[1–3] correlated-electron oxides such as high-T_c superconductors;[4] and high-κ dielectrics such as hafnium oxide.[5] This work focuses on another category—that of oxide "solid state" laser host materials.[6] Solid state laser materials typically include oxides and fluorides that serve as hosts for lanthanide or transition metal ions. The laser transitions are between electron energy levels of the ions. Interest in solid state laser materials has increased recently, as there is a trend to replace many other types of lasers with diode-pumped solid state devices. Inexpensive diode pumps and improvements in solid state technology have made these light sources more attractive. Epitaxial growth is suitable for creating solid state materials in a planar waveguide configuration. Waveguide lasers benefit from low thresholds and high gain due to reduced mode volume, as well as improved thermal properties resulting from a higher surface area–to-volume ratio.[7]

This chapter proceeds with a discussion of oxide materials in general and continues with an introduction to our crystal growth technique of choice: molecular beam epitaxy (MBE). After a review of MBE growth of oxides, we focus on Y_2O_3, our chosen host crystal. We then introduce several important materials characterization techniques used to analyze our samples and finally present the hypotheses and goals of the project.

1.1 Oxides

Oxides are extremely common compounds, composing over 99% of the earth's crust, with about half being SiO_2 and the other half metal oxides.[8] Oxygen's high electronegativity, second only to fluorine, leads to reactivity and is partially responsible for the ubiquity of oxides. Bonding in oxides varies and can be ionic, as in MgO, for example; covalent, as in SiO_2; metallic, as in ReO_3; or a combination of the above. In some layered structures van der Waals forces are also important. Nevertheless, the traditional ionic model of bonding may be the most useful, at least as a starting point; most metal oxide structures consist of metal cations surrounded by oxygen anions.[9]

Formula	Coordination	Name	Symmetry	Example
M_2O	2: linear	cuprite	cubic	Cu_2O
MO	6: octahedral	rock salt	cubic	MgO
	4: tetrahedral	wurtzite	hexagonal	ZnO
M_2O_3	6: octahedral	corundum	trigonal	Al_2O_3
	6: distorted	bixbyite	cubic	Y_2O_3
MO_2	8: cubic	fluorite	cubic	ZrO_2
	6: octahedral	rutile	tetragonal	TiO_2
AMO_3	M: 6, A: 12	perovskite	cubic	$SrTiO_3$

Table 1: Some example metal oxide structures. M represents a metal element. Table inspired by Henrich and Cox.[9]

If we view oxides as traditional ionic compounds, then there will be little orbital overlap between the ions, giving a high effective mass for charge carriers. This leads to slow charge motion, and coupling to local effects of the lattice. The polarizability of the O^{2-} ion decreases screening lengths, further emphasizing local properties.[10]

Oxides crystallize in many different structures, including rock salt, wurtzite, fluorite, rutile, corundum, and perovskite. Associated with these structures are a variety of coordination arrangements. The most common is octahedral, where each metal ion is surrounded by six oxygen ions at the vertices of an imaginary octahedron. Table 1 shows details about some example oxide structures.

Oxides have a wide variety of electronic, magnetic, optical, thermal, and structural properties. The properties of many oxides can also change dramatically in the presence of crystalline defects or deviations from their stoichiometric compositions. Interest in transition metal oxides has been very high in recent years amongst both theorists and experimentalists, owing to correlated-electron effects. Understanding the properties of these materials requires taking into account the interactions between electrons, making them difficult to model. These properties include such things as electrical conductivity but also exotic phenomena like high-T_c superconductivity and colossal magnetoresistance. A vast effort has been made to study these materials with much success, but a full understanding is still out of reach.

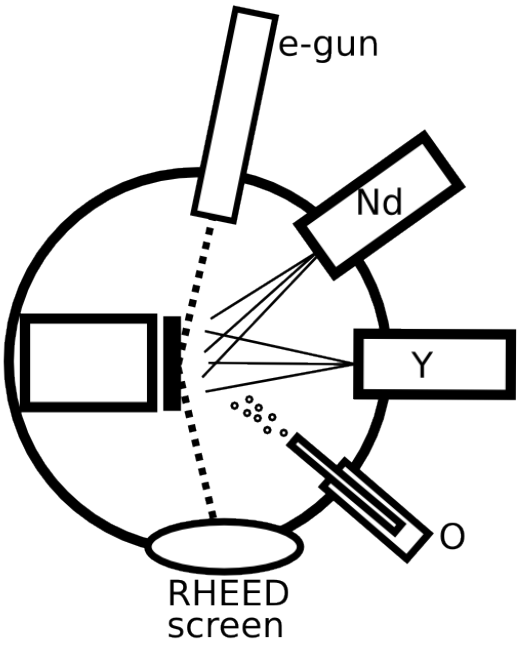

Figure 1: Schematic diagram of an MBE system. Thermal effusion cells for yttrium and neodymium are shown, along with a plasma source for oxygen. An electron gun and fluorescent screen for RHEED are also shown.

1.2 MOLECULAR BEAM EPITAXY

MBE is essentially a refined version of vacuum evaporation. Typically, thermal beams of atoms or molecules land on a heated substrate under high- or ultra-high-vacuum conditions, with pressures less than 1×10^{-5} torr. The beams are created by heating materials in a crucible or otherwise releasing the substances into the chamber. When the substrate is crystalline, and the deposited atoms arrange themselves into a crystalline arrangement influenced by the substrate, the growth is said to be epitaxial. The high-vacuum environment helps to keep the crystals "clean" and allows the molecular beams to travel without colliding with background gas molecules. The heated substrate allows deposited atoms to diffuse to crystal lattice sites. Figure 1 shows a schematic diagram of an MBE system.

Growth by MBE is slow, usually at rates below 10 µm/h, with 0.1–1 µm/h being typical. While this brings practical limitations on film thickness, it leads to excellent control over the growth process, including the ability to create sharp interfaces in multilayer structures. By opening and closing shutters that block the molecular beams, abrupt

changes can be made in crystal composition. The slow growth rate is also ideal for *in situ* monitoring. Reflection high energy electron diffraction (RHEED) is used to provide real-time information about the crystal structure of the film surface. Light scattering and reflectometry can give information about surface roughness and film thickness. Optical monitoring is discussed further in section 2.4.1.

MBE was developed mostly for semiconductor growth, especially III-V semiconductors, such as GaAs. The primary use of MBE is in research, as it is relatively expensive. It does see commercial application, however, in cases where there is no viable alternative, such as for producing GaAs-based transistors for wireless communication.[11]

Joyce[12] and Arthur[13] have written review papers on the subject of molecular beam epitaxy. Kaiser provides a brief but more general review of thin film growth.[14] The study of the actual physics of the crystal growth process is an entire research field unto itself. Pimpinelli and Villain's work provides a good introduction.[15]

1.3 OXIDE MBE

As the MBE technique became more refined, interest spread from semiconductors to other materials systems, including oxides. The number of publications related to oxide MBE started to rise in the 1980s, increased drastically throughout the 1990s, and has been high to the present. Crystalline oxides can possess almost every possible property in solid state physics, including magnetism, colossal magnetoresistance, ferroelectricity, and superconductivity. It was interest in the latter, high-T_c superconductivity, that drove a large part of the development of oxide MBE. Oxygen sublattices shared between numerous oxides point towards epitaxy as a method of producing these materials, and the purity and control possible with MBE is very appealing for the study of many phenomena.[16]

MBE is additionally enticing because of its ability to generate sharp interfaces. While bulk oxides can exhibit the fascinating properties listed above, even further opportunity exists in the study of oxide interfaces. Oxide heterostructures can be more difficult to grow than their semiconductor counterparts because some of the components can be difficult to oxidize, and the epitaxy can rely on surfaces terminated at specific ionic planes. When these difficulties are overcome, there exists opportunity to investigate new and unexplored physics.[10]

1.3.1 *Technical considerations*

The main equipment change required to prepare a semiconductor MBE system for oxide growth is the addition of an oxygen source. The simplest solution is to introduce O_2 gas to the chamber through a controlled leak valve. This is an effective method for some materials systems; however, in many cases O_2 is not reactive enough to fully oxidize the crystal components. There are several options for increasing the reactivity of oxygen, including using a thermal cracker source, an ozone source, or a plasma source. The infrastructure required for ozone systems is more substantial than the other two options and it is thus an unpopular choice. Plasma sources are more prevalent than thermal crackers because they can handle higher oxygen flow rates and therefore provide more flexibility. The plasma source operates by using a radio-frequency signal or piezoelectric sparker to ignite a plasma, ionizing the molecules and accelerating the resulting charged particles to sustain the effect. This produces more reactive excited oxygen species such as O_2^+ and atomic oxygen, O.

Another issue with oxide MBE is the presence of oxygen in the chamber along with hot filaments—*e.g.* in the substrate heater, ion gauges, thermal cells, RHEED gun, and residual gas analyzer (RGA). Oxygen gas could crack on these hot surfaces and cause damage, reducing filament lifetimes. While oxygen-resistant materials and components are now becoming more readily available, it appears from our experience that at reasonable O_2 pressures, below about 1×10^{-5} torr, for instance, oxygen damage is not a major concern. While some components may fail more quickly than in oxygen-free environments, major changes to maintenance schedules are not likely required for research systems. Some RHEED guns are also equipped with differential pumping ports to lower the pressure near the filament.

The oxygen gas used during growth could lead to additional challenges in terms of maintaining chamber vacuum integrity. Cryopumps are effective at pumping oxygen but can become loaded quickly. Additional pumping may be required depending on the application. If liquid nitrogen is used to cool cryopanels in the chamber, pressure bursts may occur subsequent to growth as condensed gasses evaporate if the panels are not continually kept cold.

1.3.2 *Previous work*

In this section we will review some recent publications related to oxide MBE. In addition to the papers by Mannhart[10] and Reiner[16] cited above, Schlom *et al.* have written a review paper about engineering oxide films using MBE.[17] Below are details of work on more specific materials systems.

In the field of oxide semiconductors, Chambers has written a thorough review of the MBE technique.[18] Look[1] and Özgür *et al.*[2] provide reviews of ZnO materials and devices. ZnO is arguably the most important oxide semiconductor being studied, with interest spurred by several factors, including a 60 meV exciton binding energy that is attractive for optical devices. Thermal fluctuations are unable to depopulate the exciton state because the binding energy is much larger than kT at room temperature. Reliable p-type doping remains elusive but would be a major development for optoelectronics. Many groups are using MBE to grow ZnO films.[19–22] Another interesting oxide semiconductor is EuO. Its ferromagnetic properties make it appealing for possible use as an electron injector in spintronic devices. EuO also exhibits colossal magnetoresistance.[23, 24]

In 1987, Webb *et al.* published an important paper on the MBE growth of high-T_c superconductors using $DyBa_2Cu_3O_{7-x}$ on $SrTiO_3$ as an example system.[25] Several subsequent papers from related groups were also published.[26, 27] MBE has become a standard technique for high-T_c superconductor research. In a similar vein, Ingle *et al.* have published an investigation into the role of epitaxy in the growth of the correlated oxide $SrCu_2O_3$.[4] Tokura and Nagaosa published a review of orbital physics in transition metal oxides that is relevant to much of the work in correlated-electron physics.[28]

Rispens and Noheda wrote about the use of MBE to grow ferroelectric $PbTiO_3$ on $SrTiO_3$.[29] Beyond ferroelectricity is the study of multiferroics, materials that exhibit at least two ferroic properties, including ferroelectricity, ferromagnetism, and ferroelasticity. MBE allows new avenues of exploration into these properties through the growth of high-quality heterostructures.[30]

James Speck's research group at the University of California at Santa Barbara has described the MBE growth of the transparent conducting oxides SnO_2, In_2O_3, and Ga_2O_3.[31–33] Víllora has also written about MBE-grown Ga_2O_3.[34]

Finally, Mackenzie, and Grivas and Eason, have published reviews of oxide films as media for waveguide lasers.[7, 35] This class of

materials would serve as a motivation for our investigation of Y_2O_3, described below.

1.4 YTTRIUM SESQUIOXIDE

Yttrium sesquioxide, also known as yttria, with chemical formula Y_2O_3, is a common refractory ceramic. It is used as a phosphor, as a source of yttrium in the preparation of other compounds, as a sintering aid, and also in optical components.[36] Y_2O_3 has the cubic bixbyite structure shown in figure 2, with a lattice constant of 10.604 Å. The unit cell has 48 oxygen atoms and 32 yttrium atoms, with 8 yttrium atoms at one type of site and 24 at another.[37] The structure is "fluoritelike," with Y on the Ca site and O on the F site, except that only 75% of the F sites are occupied. Another way to consider the structure is as follows: Imagine that the unit cell is broken up into 64 smaller cubes in a $4 \times 4 \times 4$ arrangement. There are yttrium atoms at the centre of half of these cubes. The oxygen atoms sit at six of the eight cube vertices, giving an approximately octahedral coordination. The difference between the two yttrium sites lies in which vertices the oxygen atoms occupy. The bond lengths for the eight yttrium atoms on the first type of site are all 2.261 Å, while the bond lengths for the other yttrium site differ, and there are two bonds each with lengths of 2.249, 2.278, and 2.336 Å.[36] Figure 3 shows diagrams of the two different sites.

Xu *et al.* performed density functional theory calculations using the local density approximation and estimated a band gap for Y_2O_3 of 4.54 eV.[36] This is likely an underestimate;[38] Bordun states that the band gap is 5.65 eV at room temperature.[39] Xu *et al.* show that Y_2O_3 is partially covalent with equivalent charges of 2.09 and −1.39 for the yttrium and oxygen ions, respectively.

Y_2O_3 has a melting point of 2430 °C, a thermal conductivity of $0.27\,\mathrm{W\,cm^{-1}\,K^{-1}}$, and a coefficient of linear thermal expansion of $7 \times 10^{-6}\,\mathrm{K^{-1}}$. The thermal conductivity is double that of yttrium aluminum garnet (YAG), while the expansion coefficient is the same.[40] Y_2O_3 has a low-frequency dielectric constant of 18 and an index of refraction of 1.9 at a wavelength of 1 µm.[41, 42]

1.4.1 *Y_2O_3 crystal growth*

Y_2O_3 crystals are difficult to grow from a melt because of their high melting point. The most popular techniques for producing Y_2O_3 films are the sol-gel method[43–47] and pulsed laser deposition (PLD).[48–54]

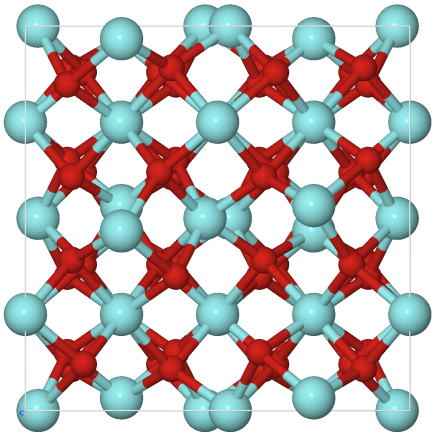

(a)

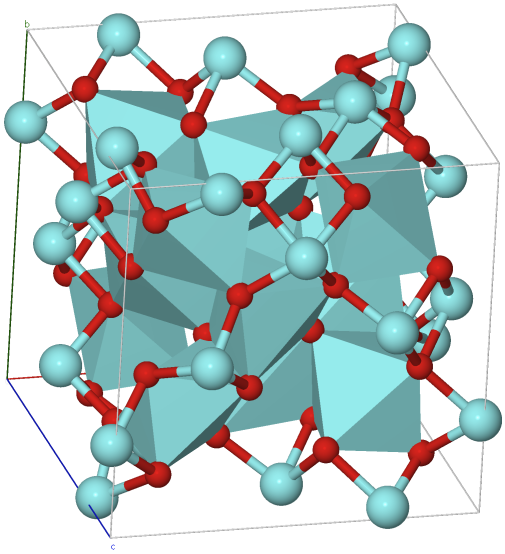

(b)

Figure 2: The Y_2O_3 crystal structure. The large cyan atoms are yttrium, and the smaller red atoms are oxygen. Subfigure (a) shows a view directly towards one of the cube faces; (b) shows a projected view with oxygen polyhedra.

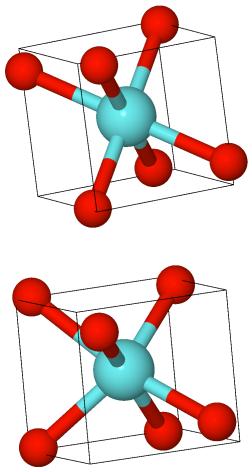

Figure 3: The two types of yttrium site in the Y_2O_3 crystal structure, with yttrium represented by the large cyan atoms and oxygen by the small red atoms. There are eight yttrium atoms with the upper configuration, which has equal bond lengths, and 24 of the bottom configuration with unequal bond lengths. If Y_2O_3 had the fluorite crystal structure, there would be only one type of Y site, with oxygen atoms at all eight corners of the cube.

The films grown by PLD are generally single crystal, while the sol-gel films are usually polycrystalline. Y_2O_3 crystals have also been grown from nanopowders,[55] using the micro-pulling-down method,[56] via a solvothermal process,[57] by sputtering,[58] and by a vapour-phase atomic layer deposition technique.[59]

Much of the above prior work is focused on optical properties, often including information regarding rare-earth doping. Many authors also include structural characterization data, and some analyze dielectric properties. PLD has proven a reliable technique for rare-earth-doped Y_2O_3 deposition on Si. Other substrates have also been used, including Al_2O_3,[53] $LaAlO_3$,[49] and MgO.[50] While optical emission and waveguided modes have been demonstrated, no lasing action has been shown in thin films.

1.4.1.1 Y_2O_3 MBE

Several groups have grown Y_2O_3 by molecular beam epitaxy or very similar methods. Their studies have mostly focused on structural and dielectric properties, in hopes of using Y_2O_3 as a dielectric on Si. In 1989, Fukumoto *et al.* grew {111}-oriented Y_2O_3 on Si (100) and Si (111) at 800 °C.[60] They used an electron-beam (e-beam) source with

a Y_2O_3 charge and released O_2 gas into their chamber to provide additional oxygen. They performed basic structural analysis and also reported that they could grow {100} Y_2O_3 on Si (100) if they used a thin yttria-stabilized zirconia buffer layer. About a decade later, Kwo *et al.* grew Y_2O_3 and Gd_2O_3 films on Si (100) for dielectric purposes and reported that their Y_2O_3 had {110} orientation.[61, 62] They also used an e-beam Y_2O_3 source but provided no additional source of oxygen. Their substrate temperature was 550 °C, and they showed that the use of an intentionally miscut substrate could suppress twinning in the Y_2O_3 film.

Cho *et al.* were similarly interested in using Y_2O_3 as an insulator on silicon and grew high-quality layers of {111} Y_2O_3 on Si (111) at 500 °C.[63, 64] They used an e-beam source loaded with yttrium metal and molecular oxygen gas, and reported very sharp spikes in x-ray diffraction ω scans. Apostolopoulos *et al.* reported {110} Y_2O_3 growth on Si (100) around the same time.[65]

More recently, Nieh *et al.* published results on high-quality Y_2O_3 films similar to those grown earlier by Cho, as well as Si (111)/Y_2O_3 (111)/Si (111) heterostructures.[66, 67] They used a relatively high substrate temperature of 780 °C, similar to that used by Fukumoto. Borschel *et al.* also reported Si/Y_2O_3/Si structures but at a lower substrate temperature of 625 °C.[68]

Tsuchiya *et al.* reviewed the status of epitaxial Y_2O_3 growth and wrote about their success in depositing {111} Y_2O_3 on Al_2O_3 (0001).[69] They used a high-temperature conventional effusion cell loaded with yttrium metal and molecular oxygen gas as material sources and conducted extensive transmission electron microscopy analysis. Their interest was more general than previous authors; they were exploring the possibilities of Y_2O_3 in oxide heterostructures. Chang *et al.* reported that they were able to stabilize a monoclinic phase of Y_2O_3 by growing on GaN.[70] The monoclinic phase usually appears only at high pressures above 10 GPa.

Our research group has also published several studies on MBE-grown Y_2O_3.[41, 71, 72] Most of the work performed by the other groups above has focussed on the use of Y_2O_3 as a dielectric. My work instead concentrates on the basics of Y_2O_3 crystal growth, hopefully providing information that will be useful for a variety of applications.

1.5 MATERIAL CHARACTERIZATION TECHNIQUES

1.5.1 *Atomic force microscopy*

Atomic force microscopy (AFM) is a surface imaging technique that measures the force between the sample and a probe to generate a view of the topography of the surface. A cantilever probe with a sharp tip on the end is caused to oscillate at a fixed frequency and then brought near the sample. As the tip gets very close to the sample, the amplitude of the cantilever vibration changes. This change is measured by a laser reflecting off the top of the probe. The probe is then scanned across the sample in a grid pattern and a feedback control system moves the sample up and down to maintain a constant cantilever oscillation amplitude. The sample-probe motion is performed by piezoelectric elements, allowing very fine control and sub-nanometre resolution. This type of imaging is called *tapping mode*, in contrast with *contact mode*, where the probe tip is continuously in "contact" with the surface. Figure 4 shows a schematic diagram of an AFM system. Figure 9 shows some example AFM images.

1.5.2 *Photoluminescence*

Photoluminescence (PL) is the phenomenon of a material emitting light as a result of the absorption of other light. For materials characterization purposes one usually directs a laser beam onto a sample and then measures any light emitted as a result with a spectrometer. By filtering out the wavelength of the pump laser, a clean emission spectrum can be recorded, giving information about the sample. The pump wavelength is often chosen to cause a certain excitation in the material. In the context of solid state laser materials, we are interested in exciting rare-earth dopant electron energy levels. The emission spectrum gives us information about those levels and the effects of the host material. In particular, crystalline host materials will exhibit sharp emission lines at specific wavelengths, while disordered materials lead to more continuous spectra. The strength of the lines will be roughly proportional to the amount of rare earth present, up until a limit, at which point interactions between the atoms reduce PL efficiency. Different crystal structures shift the pure atomic line positions in different ways, allowing PL to be used to identify which materials are present in a sample. Figure 46 shows some example PL data.

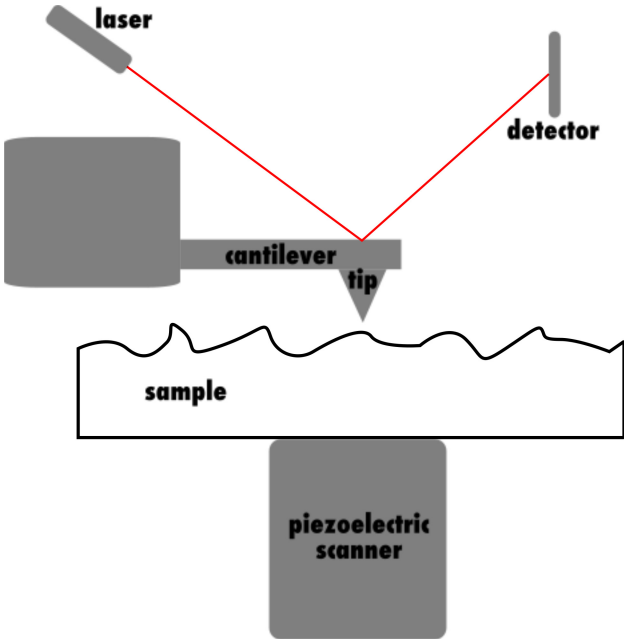

Figure 4: A schematic of an atomic force microscope system. Forces between the tip and sample cause deflection of the cantilever, which is measured by monitoring the deflection of a laser beam. This allows the generation of a surface topography image when the sample is moved sequentially by the piezoelectric scanner.

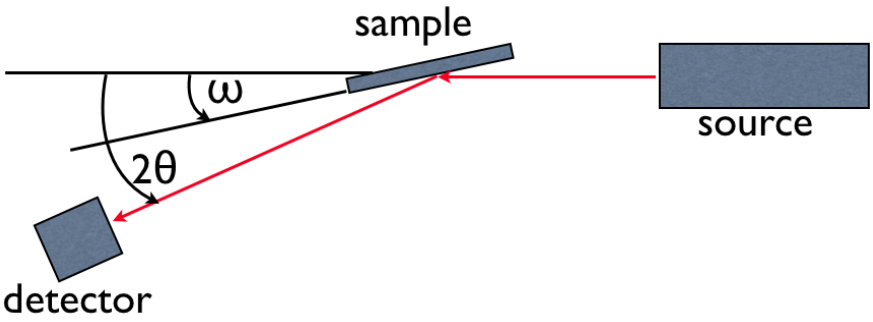

Figure 5: A schematic of an x-ray diffraction system. ω is the angle between the sample stage surface and the incident x-ray beam. 2θ is the angle between the x-ray beam and the detector. Adjusting ω and 2θ and therefore rotating the sample and moving the detector allows different measurements to be made. In this configuration, with the angle of the incident beam (with respect to the sample surface) equal to the angle of the diffracted beam, diffraction can occur from atomic planes parallel to the sample surface.

1.5.3 *X-ray diffraction*

X-rays are electromagnetic radiation with wavelengths between about 0.01 and 10 nm. By using x-rays with wavelengths on the same order as interatomic spacings in a crystal, around 0.1 nm, diffraction experiments can be performed, probing the periodic nature of the crystal lattice. Constructive interference of elastic scattering of x-rays by electrons in the crystal leads to strong diffraction under conditions given by Bragg's law:

$$n\lambda = 2d \sin\theta, \tag{1.1}$$

where n is a positive integer, λ is the x-ray wavelength, d is the spacing of crystal planes, and θ is the angle between the crystal planes and the x-rays.[73] This relation forms the basis of materials characterization studies using x-ray diffraction. By using a fixed-wavelength x-ray source and mounting the sample on a goniometer, we can adjust θ to gather information about the crystal planes present in the sample. Figure 5 shows a schematic diagram of an x-ray diffraction experiment.

The simplest type of measurement is to vary the θ angle systematically while recording the diffracted intensity. This allows you to determine at what plane spacings, d, you satisfy the diffraction condition in equation 1.1. Performing this type of scan requires rotating the sample stage, *i.e.* the angle ω, while simultaneously moving the detector, 2θ. Referring to figure 5, we see that 2θ will have to increase at twice the rate of ω due to the geometry of the apparatus. This

type of x-ray measurement is called an ω–2θ scan. The sample stage angle ω can differ from the diffraction angle θ because in practice the diffracting planes are not parallel to the sample stage. This can be due to a small misalignment related to the mounting procedure, or because measurements are intentionally being made on atomic planes that are not parallel to the sample surface. Another type of x-ray scan is the ω scan, sometimes called a rocking curve. Here the 2θ detector position is fixed, meaning that diffraction is being probed at a fixed plane spacing. The ω angle of the sample is varied, allowing measurement of how planes with the selected spacing are oriented with respect to the surface.

A useful concept for the analysis of x-ray diffraction is the reciprocal lattice. The reciprocal lattice is the Fourier transform of the crystal lattice. Extended periodic crystal planes in real space are transformed to discrete points in reciprocal space. A geometric representation called the Ewald construction can be used to examine diffraction in terms of reciprocal space.[73] Figure 6 shows an example of the Ewald representation. We draw a vector k_i, representing the incident x-ray beam, with length $1/\lambda$, at an angle to the horizontal axis corresponding to the angle between the beam and crystal surface, ω, and place the tip at the origin of reciprocal space. Now we draw a circle centred at the tail of this vector with radius $1/\lambda$. Any reciprocal lattice point that lies on this so-called Ewald circle will cause a diffracted beam, k_d, to be emitted in the direction between the centre of the circle and the reciprocal lattice point. The strength of the emitted beam is dependent on a number of factors, including the structure factor, which takes into account the atomic scattering cross-section and the geometry of the crystal. The true Ewald construction should be in three dimensions with an analogous Ewald sphere, but the two-dimensional picture is easier to visualize.

The right side of figure 6 shows the motion in reciprocal space corresponding to the ω–2θ and ω scans described above. An ω–2θ scan varies the length of the scattering vector Δk, which is equal to $1/d$, and therefore detects diffraction at varying plane spacings d. An ω scan changes the angle of the scattering vector with respect to the sample surface, detecting the orientation of the planes with respect to that surface. This allows the measurement of how much the crystal plane tilt varies throughout the sample. The reciprocal lattice points corresponding to crystal planes that are parallel to the sample surface lie along the k_z axis in reciprocal space.

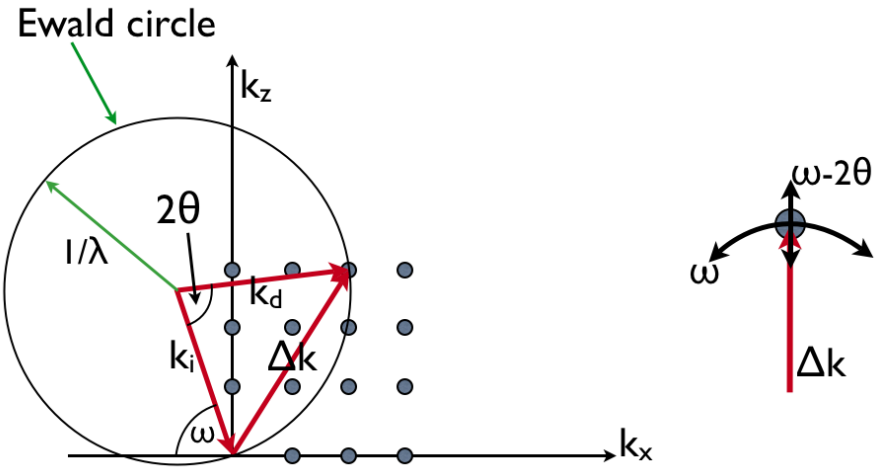

Figure 6: The Ewald construction of diffraction in the reciprocal lattice. k_i and k_d are the wave vectors of the incident and diffracted beams, respectively, and Δk is the scattering vector. Diffraction occurs when a reciprocal lattice point lies on the circumference of the Ewald circle, which has a radius inversely proportional to the x-ray wavelength. The image at right depicts the motion of ω–2θ and ω x-ray scans (described in the text) in reciprocal space.

1.5.3.1 *Reciprocal space maps*

The types of scans mentioned above, ω–2θ and ω, result in a plot of diffracted intensity versus angle. They are essentially measuring a single line through reciprocal space (as shown in figure 6). To maximize signal strength, usually only a relatively large slit, on the order of 1°, is placed in front of the detector. This means that the "line" through reciprocal space is somewhat wide and the measured intensity is actually an average over a range of diffraction conditions. In order to get a more accurate view of the reciprocal space picture, a technique called *reciprocal space mapping* can be employed. The slit in front of the detector is replaced with a high-angular-resolution analyzer crystal system that samples only a very small point in reciprocal space. Then a series of scans is performed, tracing out a two-dimensional grid in reciprocal space. After the data is collected, a contour plot or image map can be made to display the results. This can give a much clearer view of the reciprocal space representation, but the tradeoff is that the measurements are very long, up to days, depending on the circumstances. Figure 7 shows a schematic reciprocal space view of the individual scans involved in creating a reciprocal space map. This

example depicts the usual choice of a series of ω–2θ scans, as used throughout this thesis, but theoretically other choices could be made, depending on the software used to control the x-ray diffractometer. Figure 31 shows a reciprocal space map plotted directly with real-space angular axes. This clearly shows how the diffractometer was oriented during the collection of each data point. Figure 56 shows a more typical reciprocal space map with reciprocal space axes, where the diffractometer angles have been converted to reciprocal lattice units using the following equations, which are based on the geometry shown in figure 6.

$$-k_x = \frac{1}{\lambda}\big(\cos\omega - \cos(2\theta - \omega)\big) \tag{1.2}$$

$$k_z = \frac{1}{\lambda}\big(\sin\omega + \sin(2\theta - \omega)\big) \tag{1.3}$$

In the case where the diffracting planes are parallel to the sample surface, and any tilt due to sample mounting has been accounted for, we have $\omega = \frac{2\theta}{2}$ and therefore

$$k_x = 0 \tag{1.4}$$

$$k_z = \frac{2\sin\omega}{\lambda}, \tag{1.5}$$

which can be recognized as an rearrangement of Bragg's law, equation 1.1, with $k_z = 1/d$.

1.5.3.2 *X-ray reflectivity*

A related characterization technique is x-ray reflectivity. In this case, rather than diffracting the x-ray beams off the crystal planes, much shallower, grazing incidence angles are used, resulting in an optical-like reflection. The scattering vector is smaller, and therefore the real-space length scale probed is larger. Most substances have indices of refraction slightly less than 1 in the x-ray wavelength regime. This means that total external reflection will occur below some critical angle. A typical critical angle would be around 0.3°, corresponding to an index of refraction around 0.99999. Measuring this critical angle with x-ray reflectivity allows one to estimate the density of the sample.[74]

For a sample with multiple distinct layers, such as an epitaxial film on a substrate, interference oscillations can be seen in the reflectivity beyond the critical angle. The period of these oscillations is related to the layer thicknesses and can be calculated using a standard optical

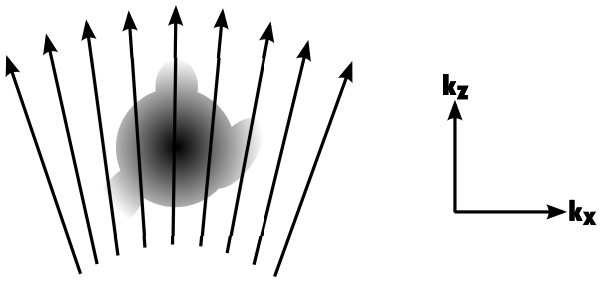

Figure 7: A depiction of the reciprocal space mapping procedure. A series of scans, shown here as arrows, are performed to record the intensity of diffraction over a region of reciprocal space. In this example a series of ω–2θ scans are shown. Each scan started with the same 2θ value, but a different ω sample tilt. During the scans both ω and 2θ axes were moved as usual, resulting in straight lines pointing away from the origin of reciprocal space. The greyscale shape represents an unusual reciprocal lattice point (in contrast with the simple circles in figure 6) that was being studied in more detail. In reality the scans would have to be much closer together to fully capture the fine structure of the spot.

multilayer analysis. The oscillations will be damped out at higher angles by substrate-epilayer interfacial roughness, and the overall reflectivity will drop more quickly as the angle is increased if the epilayer is rough.[74] Figure 53 shows an x-ray reflectivity scan. X-ray reflectivity curves can be modelled using computer software. By comparing the experimental measurement to a theoretical prediction, estimates of sample properties can be made, including, as mentioned above, densities, thicknesses, and roughnesses.

1.5.4 *Transmission electron microscopy*

Transmission electron microscopy (TEM) is another useful characterization technique. TEM can provide information about crystal structures from electron diffraction patterns, and can also be used to produce images with far greater than optical resolution. Unfortunately the hardnesses of Y_2O_3 and sapphire increase the difficulty of TEM sample preparation. My colleague Shawn Penson has performed some TEM measurements on Y_2O_3 films grown in our lab, but they were unavailable for inclusion in this thesis. When the results are published they will likely provide more insight into the Y_2O_3 crystal growth process.

1.6 HYPOTHESES AND GOALS

A fundamental question addressed by this thesis is as follows: "Is MBE a suitable technique for growing optically active Y_2O_3 waveguides?" We start with a number of hypotheses. We will find that suitable Y_2O_3 crystals can be grown by MBE and that the structure and surface properties of the crystal can be influenced by a number of factors. These factors include the starting substrate surface, growth conditions, use of a surfactant, and post-growth annealing. We will also find that rare-earth dopants, specifically Nd, can be incorporated successfully, *i.e.* in such a way that they radiate efficiently, in the MBE-grown film. We will show that the properties of the crystals can be understood and modelled with theory, such that informed decisions can be made regarding adjustment of the growth procedure.

In light of the above, we have the following goals: to grow high-structural-quality single-crystal Nd:Y_2O_3 films with smooth surfaces as a model system for solid state planar waveguide lasers and to understand the process of the crystal formation and learn how to reproducibly create the films by controlling the growth process. As the work progressed, some modifications to, and excursions from, these goals also occurred, and these will be discussed.

1.7 OUTLINE OF THESIS

Following this introduction, we present four additional chapters with primary content. Chapter 2 covers substrate preparation and some details of the growth apparatus. Chapter 3 provides results on post-growth annealing of Y_2O_3 films. Chapter 4 discusses the use of x-ray diffraction to analyze the Y_2O_3 films. Finally, chapter 5 contains the results of our use of surfactants during sample growth. After a brief conclusion and bibliography, the appendices provide additional details of aspects of the above and describe subsidiary topics, including our attempts to grow Al_2O_3 and Ga_2O_3 on Al_2O_3 substrates.

2 Substrate preparation and molecular beam epitaxy techniques

The starting crystal surface can play a crucial role in epitaxial growth. In this chapter we will discuss our substrate preparation methods and also some specialized growth techniques used in our experiments.

2.1 substrate annealing

Sapphire was the primary substrate material used for our crystal growths. Sapphire is the corundum phase of aluminum oxide and is often written as α-Al_2O_3. The corundum structure has a three-fold symmetric rotational axis and is part of the trigonal crystal system and rhombohedral lattice system. Usually an equivalent hexagonal lattice is used to describe the sapphire structure for convenience. The hexagonal unit cell has three times the volume and three times as many atoms as the rhombohedral cell. Sapphire substrates are generally available in four orientations. In hexagonal four-index notation they are: A $(11\bar{2}0)$, C (0001), M $(10\bar{1}0)$, and R $(01\bar{1}2)$. These primary orientations are depicted in figure 8.

The substrates were annealed because experiments showed that annealing yielded several benefits. RHEED patterns from annealed substrates, and from Y_2O_3 films grown on those substrates, were significantly easier to see on the fluorescent screen in the MBE, AFM measured surface morphology was smoother, and x-ray diffraction film peak widths were narrower, indicating superior crystal quality. For instance, in one comparison of two 1000 nm thick Y_2O_3 films on annealed and unannealed R-plane sapphire with otherwise similar growth conditions, the film grown on the annealed substrate had an ω–2θ x-ray peak width of 0.014° compared with 0.049° for the unannealed sample; an ω x-ray peak width of 0.75° compared with 1.1°; and an AFM-measured root-mean-square (RMS) surface roughness of 8 nm compared with 20 nm. These differences represent significant improvements.

Sapphire substrates were obtained from several vendors and on receipt were annealed at 1150 °C for 9 hours in air. The wafers were placed in an alumina box before being loaded into a Lindbergh box furnace. Annealing sapphire is known to produce atomic steps on the surface.[75] Figure 9a shows a typical as-received sapphire wafer

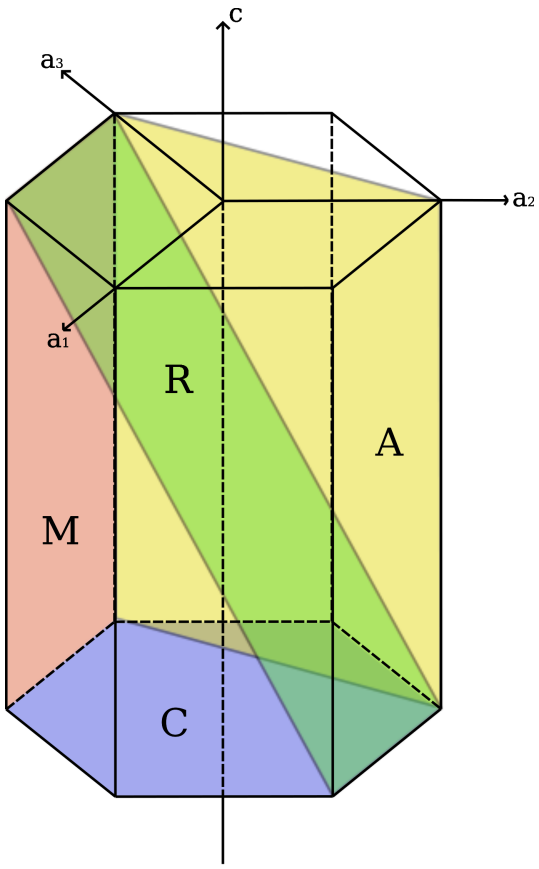

Figure 8: Commonly available orientations of sapphire substrates: A $(11\bar{2}0)$, C (0001), M $(10\bar{1}0)$, and R $(01\bar{1}2)$. In this diagram the equivalent planes $(0\bar{1}10)$ for M and $(\bar{2}110)$ for A are shown for clarity. The a lattice parameter is 4.758 Å and the c lattice parameter is 12.99 Å.

surface imaged by a Digital Instruments Nanoscope III AFM. Figure 9b shows a substrate surface after annealing, with obvious atomic steps. The spacing between atomic steps corresponds to the miscut of the wafer. The miscut is defined as the deviation of the normal of the polished surface from the ideal normal to the desired crystal plane. All of the wafers used were nominally flat and most had miscuts of less than 0.1°.

Since our starting sapphire substrates were finely polished, the surfaces after annealing consisted of uniform parallel steps. When a less perfectly polished YAG substrate was annealed, the result was numerous islands, as shown in figure 10.

To further investigate the surface changes during annealing, several sapphire substrate pieces were intentionally scratched with 15 μm polycrystalline diamond particles. The surfaces were then imaged with an AFM. Subsequently the samples were annealed and re-imaged. To enable successful scanning of the same spot on the sample before and after the annealing step, a diamond scribe was used to scratch an "X" into the surface of the sapphire. Careful positioning of the sample in the AFM allowed the end of one of the legs of the "X" to be found.

A series of scratched and unscratched C- and R-plane sapphire substrates were measured before and after annealing for 48 hours at 1500 °C. All samples had previously undergone the standard nine-hour, 1150 °C anneal and were annealed again for two hours at 1150 °C immediately after the scratching process. This helped to clean the surface and therefore improved the quality of the images of the scratches taken before the 1500 °C anneal.

The unscratched C-plane substrate exhibited step bunching, as seen in figure 11, where individual atomic steps, each one sixth of the c-axis lattice constant high, merge into taller steps with heights that are integer multiples of the single-step height. This has been reported previously in the literature.[75, 76] The amount of step bunching is much higher after the anneal at 1500 °C, with steps up to 12 units high (2.6 nm) visible in figure 11b. In contrast, the unscratched R-plane sample seen in figure 13 showed little change, though there did appear to be some concentration of material at the step edges. This has not been reported previously for sapphire. Material building up at step edges has been seen on other surfaces, such as iridium, and could be caused by a potential well on the upper side of the step.[77] Figure 12 shows section lines from the AFM images in figure 11 that illustrate the step bunching effect.

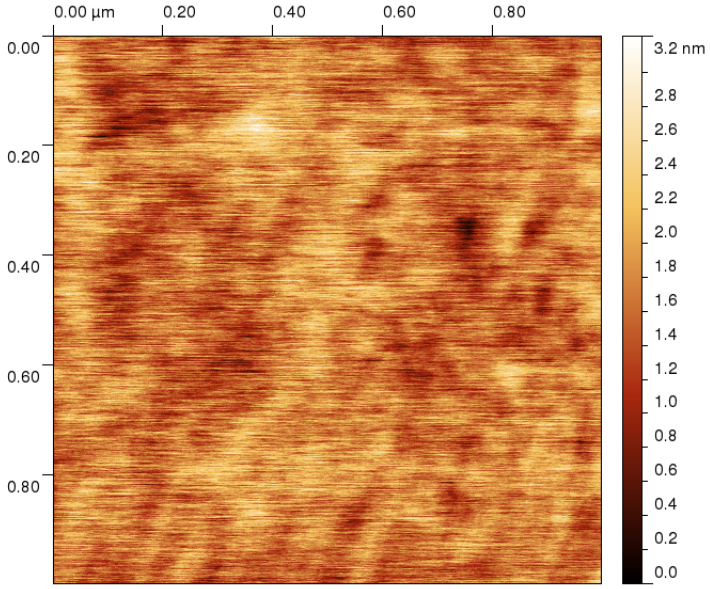

(a) On receipt

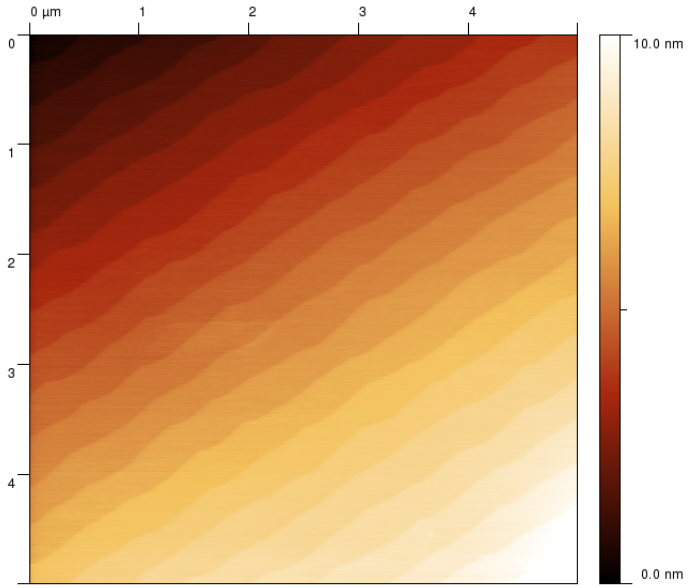

(b) After annealing

Figure 9: AFM images of sapphire substrates. (a) On receipt from the manufacturer. The horizontal striations are imaging artifacts. Very little detail is visible on the finely polished surface. (b) After annealing in air at 1150 °C for 9 hours. Atomic steps are plainly visible.

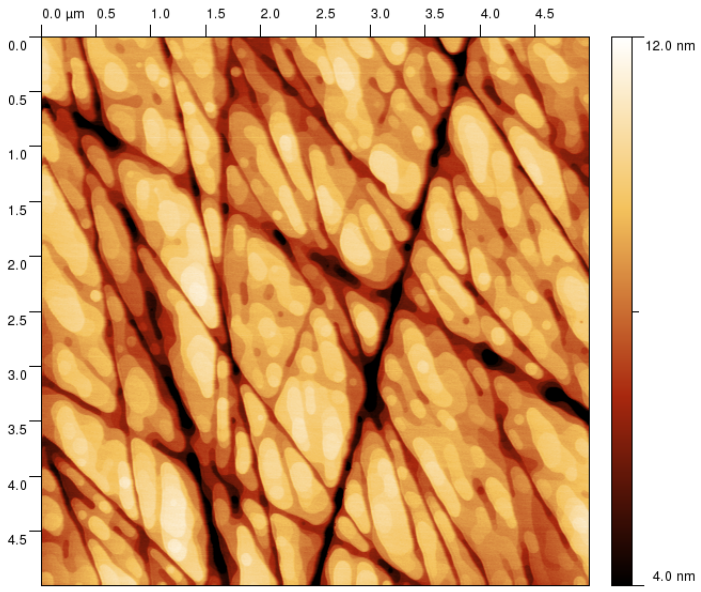

Figure 10: An AFM image of a YAG substrate surface after annealing for nine hours at 1150 °C in air. Scratches present on the surface before annealing are responsible for the patterning. Image courtesy Miriam Gantert.

Step bunching could be indicative of a positive Ehrlich-Schwoebel barrier,[15] the energy required for an adatom to move over a step edge in the "downhill" direction. If the sapphire was evaporating, then more atoms would leave from wider steps, and this potential barrier would make it preferential for those atoms to detach from the uphill side of a terrace because detaching from the downhill step edge would require overcoming the barrier.[15] This would cause wider steps to become wider still, and eventually all the steps could bunch together in pairs. Then the process could repeat, leading to quadruple-height steps, and so on. Van *et al.* confirm the preference for steps that are even-multiples of the minimum step height and also discuss other possible rationales for step bunching. They calculate an activation energy for diffusion of 2 eV and by comparing with other literature conclude that surface diffusion is the most likely transport mechanism.[75] Our temperature of 1500 °C could be high enough for evaporation, though the vapour pressures in the Al-O system depend on the environment.[78] Deformation of the alumina box holding the samples in the furnace was noted after our annealing process.

Since the step edges were still quite straight after the long high-temperature treatment, we can assume that the annealing temperature

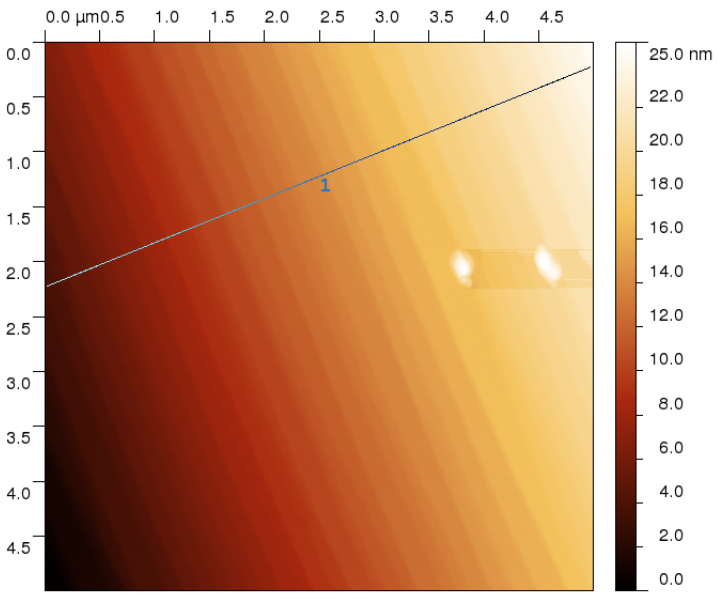

(a) Before

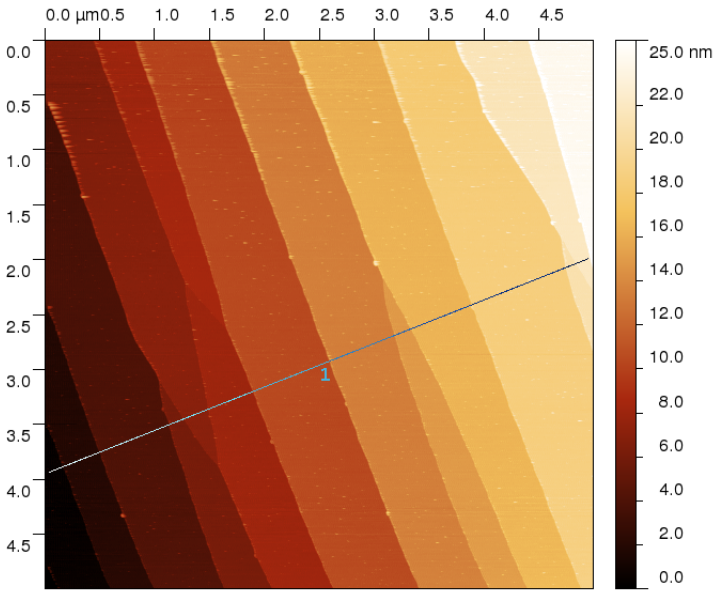

(b) After

Figure 11: AFM images of an unscratched C-plane sapphire substrate (a) after annealing at 1150 °C for nine hours and (b) after annealing at 1500 °C for 48 hours. Individual atomic steps have coalesced into taller multiple-height steps through a process known as step bunching. The lines indicate the positions of the section profiles shown in figure 12.

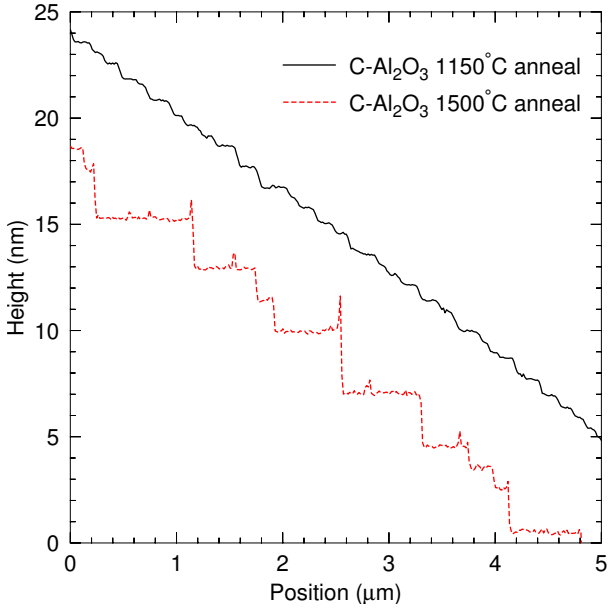

Figure 12: Section profiles from the AFM images of the unscratched C-Al_2O_3 substrates shown in figure 11. Significant step bunching is present in the sample annealed at 1500 °C (dashed, red).

was below the roughening transition temperature. This is the temperature at which the line tension of a step edge vanishes. At higher temperatures extra energy is required to maintain straight steps; the natural result is roughening. This allows us to put a very rough lower limit on the step edge energy of 0.11 eV, using the relationship from Pimpinelli and Villain:[15]

$$T_R \approx \frac{E_{step}}{k_b \ln 2}, \tag{2.1}$$

where T_R is the roughening transition temperature, E_{step} is the step edge energy, and k_b is the Boltzmann constant. This approximation comes from finding the temperature at which the Helmholtz free energy, $F = U - TS$, is zero, using a simple expression for the step edge entropy per unit length, $S = \ln 2$.[15] Our value for the step edge energy is approximately the same as the *upper* limit derived from the results of Park *et al.*, who reported that 1620 °C was above the roughening transition for alumina powder.[79]

The changes in the scratched samples after high-temperature annealing were more dramatic. Figures 14 and 16 show standard AFM images of the results. Figures 15 and 17 show the same results, but

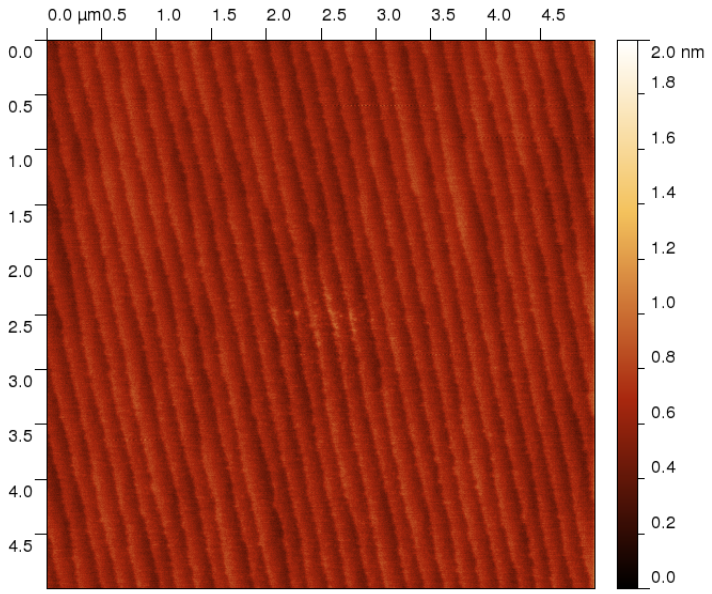

(a) Before

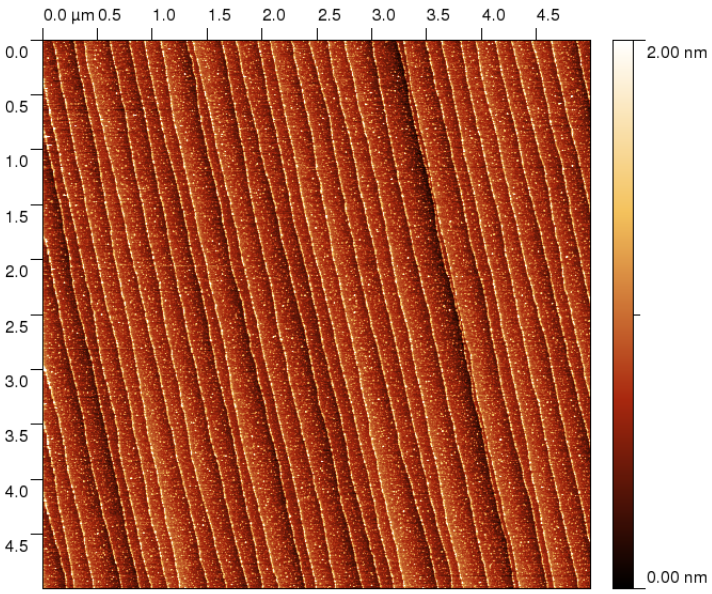

(b) After

Figure 13: AFM images of an unscratched R-plane sapphire substrate (a) after annealing at 1150 °C for nine hours and (b) after annealing at 1500 °C for 48 hours. Material appears to have gathered at the step edges. Unlike in figure 11, these images are displayed without the atomic step faces parallel to the page to emphasize small differences using the colour scale.

now the raw amplitude of the AFM cantilever is displayed. This is essentially the derivative of the standard surface height image and serves to highlight the step edges. The scratches are filled in to varying degrees after the 1500 °C anneal and significant rounding of the terraces has taken place. On the R-plane sample, material concentrated itself on the step edges, in the same way as for the unscratched R-plane substrate.

Understanding how the sapphire surfaces change during annealing is helpful for finding optimal substrate preparation procedures. In our case we found that an anneal at 1150 °C was sufficient to generate atomically stepped surfaces without excessive step bunching on C-plane substrates. Annealing at higher temperatures may be beneficial if scratches are present on the starting surface. With less drastic scratches than our test samples it may be possible to completely smooth the substrate with an end result of straight step edges.

2.2 SUBSTRATE CLEANING

The 50 mm diameter sapphire wafers were processed prior to being diced with a diamond saw into 1 cm by 1 cm squares. The processing included the annealing described in section 2.1 and also coating the back side of the substrate with chromium and molybdenum to aid with substrate heating as discussed in section 2.4.2. During dicing the top growth surface of the substrate was covered with sticky wafer-handling film. This protected the surface from most contamination during dicing. After removal of the film the surface appeared clean to the unaided eye, but AFM imaging proved impossible, likely due to remnant contamination from the sticky film.

Epitaxial growth depends on the "communication" between the substrate and epilayer, and for this reason having a clean starting surface to prevent any interference in this "conversation" is a logical desire. For our experiments a variety of cleaning protocols were evaluated.

The initial method was to place the substrates in a wafer carrier and then into a beaker containing acetone, which was subsequently placed on a hotplate. The acetone was heated and the substrate kept in the beaker for five minutes after it came to a boil. Then the substrates were transferred to a room-temperature methanol bath in a different beaker for five minutes before finally being rinsed in de-ionized water and blown off with dry nitrogen gas. The acetone was intended to remove organic material, and the methanol rinse was used to remove

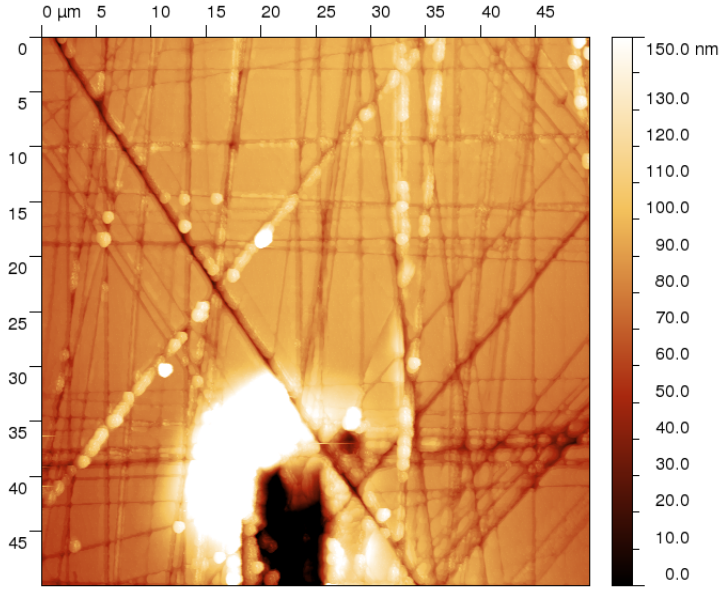

(a) Before

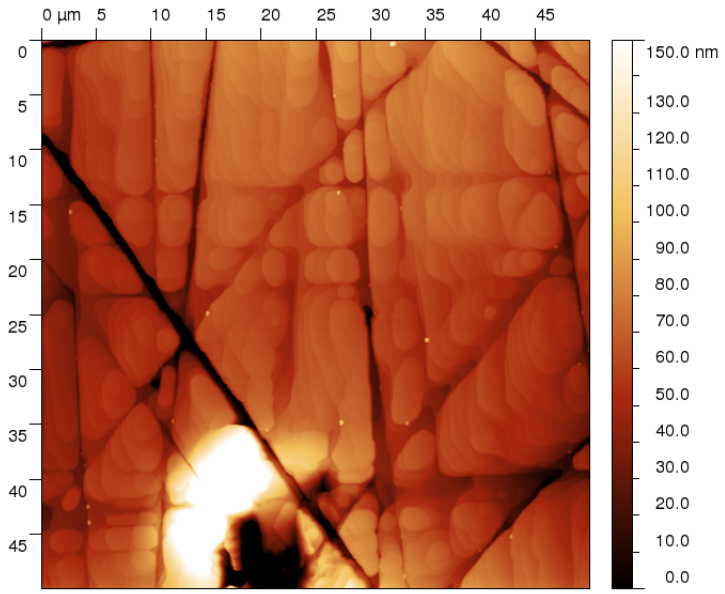

(b) After

Figure 14: AFM images of a scratched C-plane sapphire substrate (a) after annealing at 1150 °C for 11 hours and (b) after annealing at 1500 °C for 48 hours. Step edges have become rounded and the scratches have filled in to varying degrees.

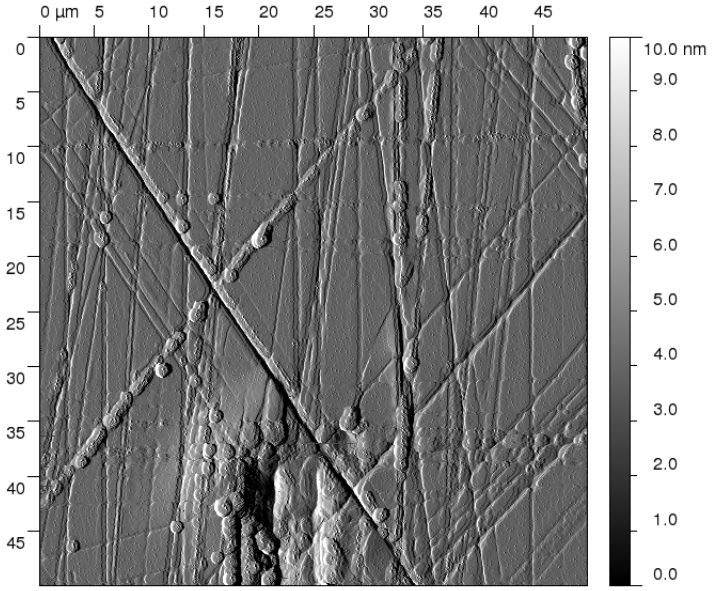

(a) Before

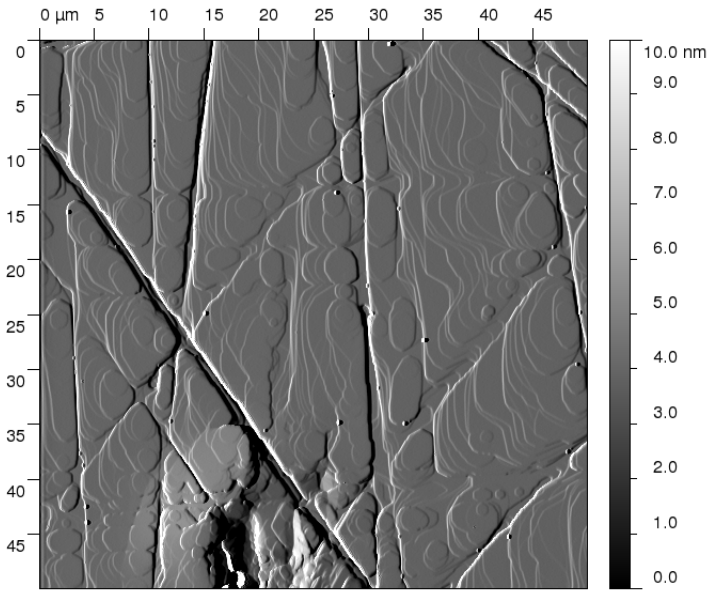

(b) After

Figure 15: Amplitude AFM images of the scratched C-plane sapphire substrate shown in figure 14 (a) after annealing at 1150 °C for 11 hours and (b) after annealing at 1500 °C for 48 hours. Step edges have become rounded and the scratches have filled in to varying degrees.

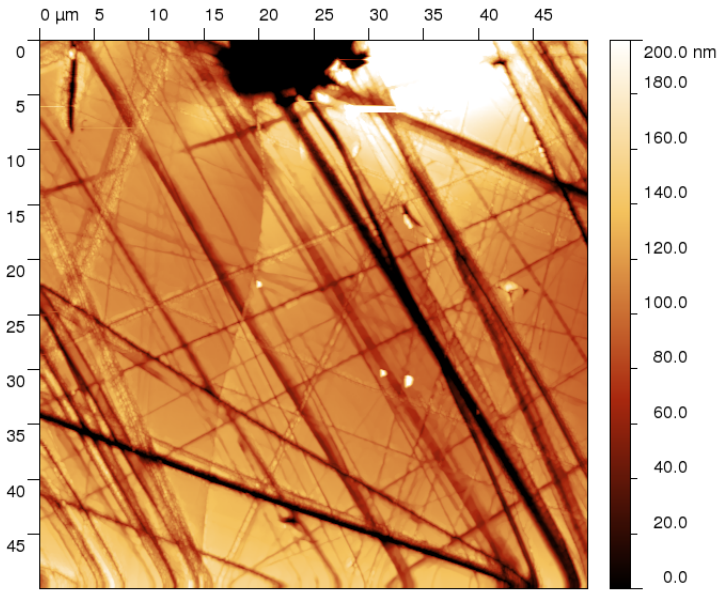

(a) Before

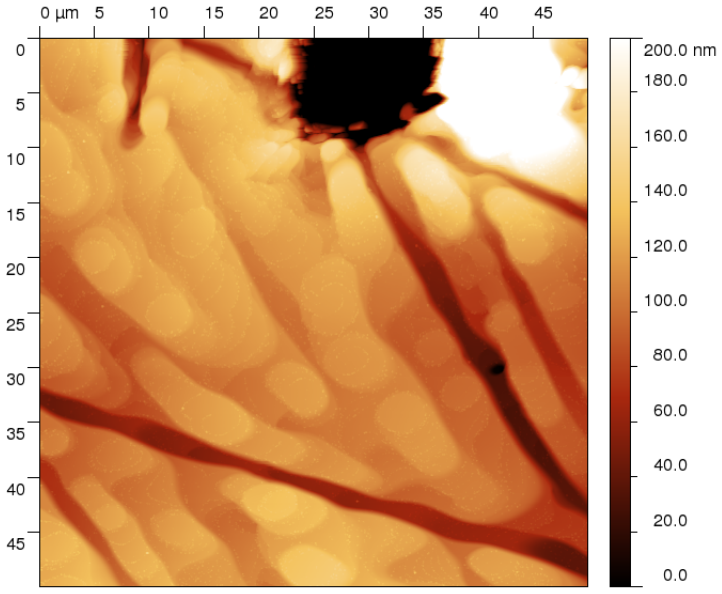

(b) After

Figure 16: AFM images of a scratched R-plane sapphire substrate (a) after annealing at 1150 °C for 11 hours and (b) after annealing at 1500 °C for 48 hours. Significant step edge rounding and scratch filling has occurred, along with material concentration at the step edges, as seen in the unscratched sample in figure 13b.

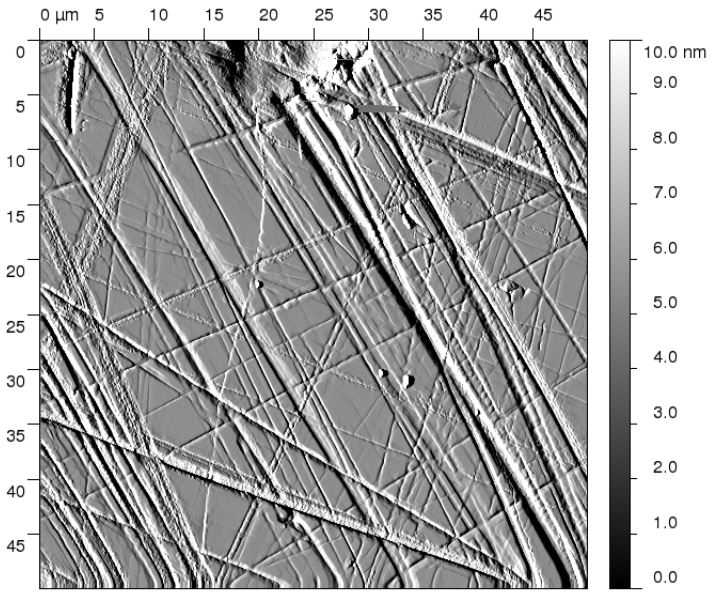

(a) Before

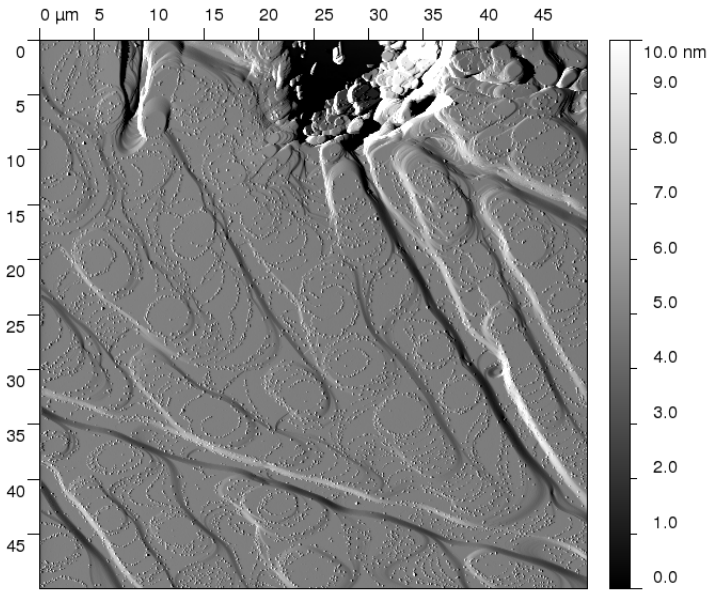

(b) After

Figure 17: Amplitude AFM images of the scratched R-plane sapphire substrate shown in figure 16 (a) after annealing at 1150 °C for 11 hours and (b) after annealing at 1500 °C for 48 hours. Significant step edge rounding and scratch filling has occurred, along with material concentration at the step edges, as seen in the unscratched sample in figure 13b.

acetone residues as it was thought to be a less contaminated solvent. Unfortunately AFM images of samples cleaned with this method would often show numerous spots left behind on the substrate. Figure 18a shows an example of a substrate cleaned with this method. The spots are smaller than a typical dust particle that is occasionally seen in AFM.

A variation on the above method was to add the use of an ultrasonic cleaner and/or micro organic soap. The soap, from Allied High Tech Products, was intended to help remove general contamination and the ultrasonic to provide a stronger cleaning action. Results were inconclusive; occasionally the AFM images would show cleaner surfaces, but other times no change was seen. On one occasion there appeared to be a reaction between the soap and one of the solvents that caused excessive contamination on the surface in the form of a white translucent film, but this could have also been from some other unknown source.

Ozone cleaning was also investigated. Here ultraviolet light is used to generate ozone inside a box containing the substrate. The ozone reacts with contaminants on the surface, disassociating them into molecules such as CO_2, H_2O, and N_2.[80] As shown in figure 18b, this treatment resulted in a great improvement in the cleanliness of the substrate surface.

Wet etching can also be used for sapphire substrate preparation. A substrate was dipped in a solution of H_3PO_4:H_2SO_4 1:3 heated to 150 °C for 10 minutes and then rinsed in de-ionized water and blown dry with N_2. Figure 19a shows an AFM image of a substrate that was etched as described. This surface is similarly clean to the ozone-treated sample. Substrates etched at lower temperatures did not turn out clean. Unfortunately the etching process dissolves the back surface metallization used for heating purposes, so this technique is not ideal. Metallization after etching is possible but increases total processing time, since it is slightly more difficult to coat many small substrate squares than it is to coat one large wafer, and further processing after cleaning is not optimal from a general cleanliness perspective. Ideally the substrates would be loaded into the MBE chamber immediately after cleaning.

While various epitaxial samples showed characteristic "spots" or "spikes" on the surface that were thought to possibly originate from surface contamination, no correlation could be made between cleaning method and the presence, or lack, of these features in the grown films. This led us to believe that the act of heating the substrate in the MBE growth chamber could be removing the dirt and rendering

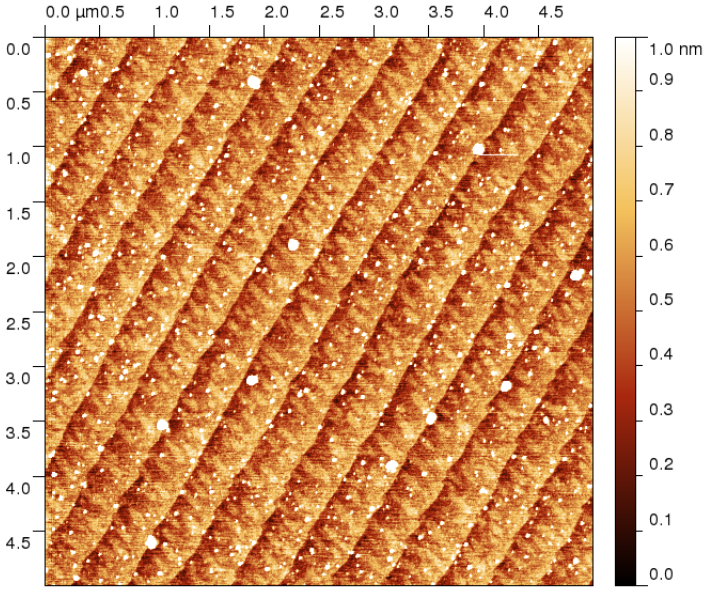

(a) Solvent cleaned

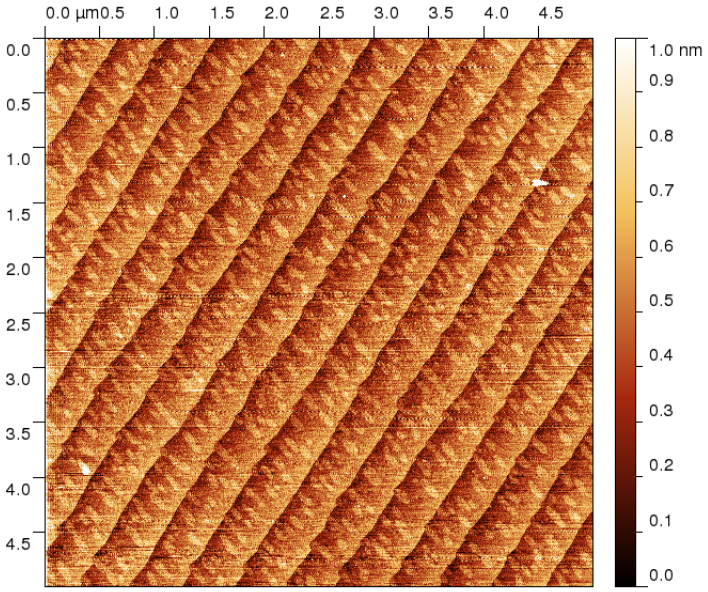

(b) Ozone cleaned

Figure 18: AFM images of annealed sapphire substrates after cleaning. (a) Cleaned with acetone and methanol. The bright white spots are residual dirt left behind after cleaning. (b) Cleaned with ozone treatment. The small "islands" on the steps appear to be a feature of the substrate itself.

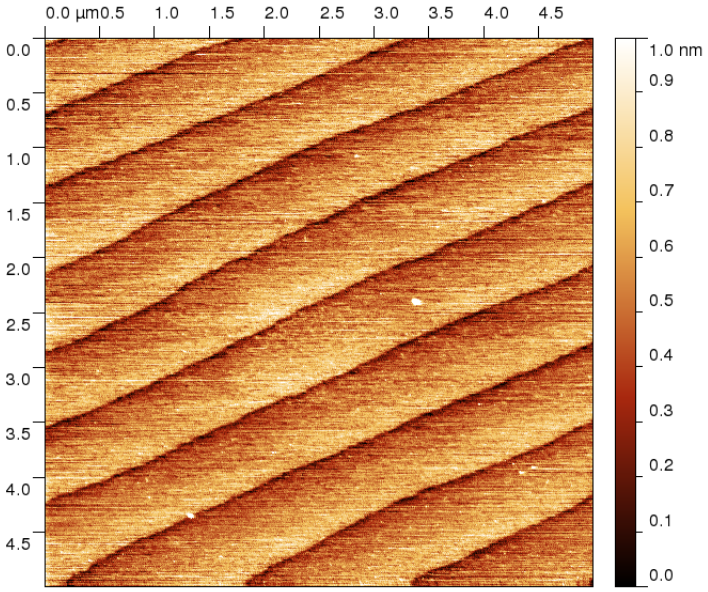

(a) Acid etched

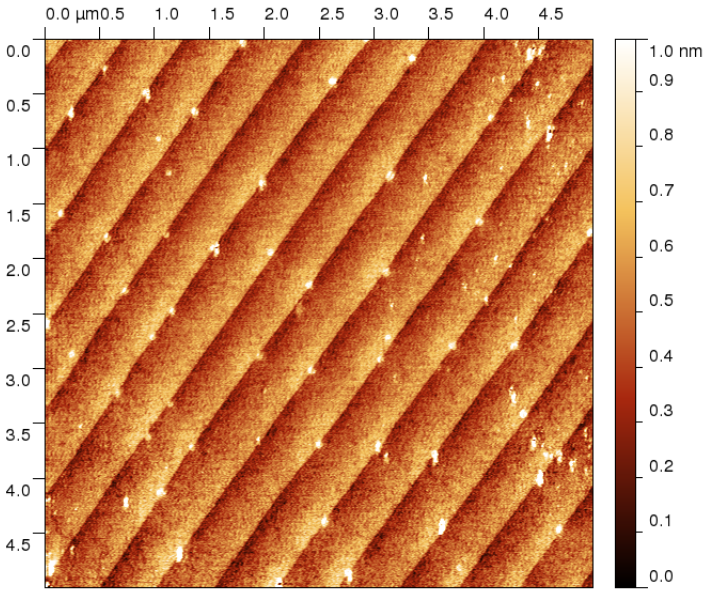

(b) Heat cleaned

Figure 19: AFM images of annealed sapphire substrates after cleaning. (a) Wet etched in a 1:3 solution of H_3PO_4:H_2SO_4 for 10 minutes at 150 °C. (b) Cleaned solely by heating in the MBE to around 800 °C for 15 minutes.

cleaning unnecessary. Therefore, a sample was loaded into the MBE in an unclean state and heated to approximately 800 °C and left for 15 minutes. Figure 19b shows an AFM image of the substrate after this treatment. This partially clean result may indicate that heating does help with substrate preparation. The presence of oxygen before the growth begins may be additionally beneficial. It is also possible that the oxide growths we have performed are not particularly sensitive to surface cleanliness or that the level of contamination present after heat cleaning is low enough to have a negligible effect.

The ideal cleaning strategy remains perhaps somewhat elusive. Ozone cleaning seems to show the most promise, but subsequent measurement with the AFM provides the most certainty that the substrate is truly clean. This adds time to the processing workflow but may be beneficial in ruling out surface contamination as a problem. Pre-growth AFM images can be useful in other instances as well, for comparing atomic steps before and after growth, for example. Regardless of the cleaning method, or lack thereof, care must be taken to avoid accidentally adding contamination during the procedure.

2.3 SUBSTRATE STRUCTURAL CHARACTERIZATION

This section describes techniques used to analyze the physical structure of the substrates before growth. The same methods can also be used to perform analysis on the sample after the epitaxial film is grown.

2.3.1 *AFM step height measurements*

When dealing with surfaces made up of atomic steps, such as one of our annealed substrates, it is natural to want to measure the height of those steps. While this may seem to be a quantity that is easy to extract from AFM images, it turns out that it isn't quite that simple, as described below. In this section we present practical information to aid in the step height measurement process.

2.3.1.1 *Basic image processing*

Usually the captured AFM image is not very ideal and needs to be processed. Often this includes median correction, where the median value of each row in the image is set to be the equal, and x/y polynomial correction, where a curved surface is fit to, and subtracted from, the data in order to flatten the image. It is also usually advantageous

to rotate the image so that step edges run along the y-axis. In fact, it is advantageous if the sample is scanned in this orientation, with the fast-axis motion perpendicular to steps, since it makes the tip transition between steps more abrupt. Finally the data is tilted so that the steps are flat, creating a staircase profile.

2.3.1.2 *Step height extraction*

Once the image has been processed, the most obvious way to find step heights is to extract a section line running perpendicular to the step edges from the data. Unfortunately the result is often very noisy, making it difficult to determine the true z-position, and therefore height, of each step surface. Additionally, small tilts remaining in the data result in incorrect step heights. Figure 12 shows two example section profiles. In the top profile it is difficult to distinguish between the many steps and they do not appear to be flat. Even in the bottom profile that shows significant step bunching and well defined steps, the differences in height between the terraces do not exactly match the expected integer multiples of atomic units, suggesting errors in image acquisition or processing.

An alternative method to determine step height is to create a histogram of z-values in the image. For an ideal surface the histogram would consist of a series of spikes at the heights of each step. For less ideal surfaces the spikes would be broadened into a series of peaks. The separation of these peaks would give the step height. Unfortunately both the section-line and histogram methods are quite sensitive to undetected image tilt. That is, if the image appears to be level, with all the atomic steps flat, but is in reality slightly tilted, it is quite easy to think that everything is fine and proceed to determine an inaccurate step height. Looking at the two-dimensional image is not a good way to determine flatness and, as mentioned above, section lines are often noisy.

To further analyze this issue, a Matlab program was written to create height histograms for various image tilts. The results were plotted in a colour-intensity map, with the histograms running along the x-axis and the different tilts along the y-axis. At the "correct" tilt, the histogram will be maximally sharp, and as you move away from that point, the histogram will broaden and the peak positions will shift.

Figure 20 shows both a simulated ideal stepped surface and a real annealed R-plane sapphire surface. Figure 21 shows the tilt-histogram

maps corresponding to the surfaces in figure 20. As mentioned above, each row in the maps is a height histogram of the surface for the corresponding y-axis tilt value. The colour represents the histogram value. In figure 21a the histogram is maximally sharp at zero tilt, as expected. On this row, the distance between the peaks in the histogram give the correct step height of 1 Å. The distance between the optimal tilt, zero in this case, and the "neck" in the upper part of the figure is the wafer miscut. Here it matches the expected 0.06°. Figure 21b shows the tilt-histogram plot corresponding to the real surface in figure 20b. The maximally sharp histogram appears to be slightly below the zero mark on the y, or tilt, axis but it is hard to tell, illustrating the pitfall of this method.

As can be seen from the real histogram results in figure 21b, it can be difficult to tell when the image is properly tilted, since there is not a major visible difference between the shape of the histogram for a range of tilts near the ideal value. This could lead to an incorrect step-height determination because the resultant step height value does vary in this range. It is quite normal to see a good-looking histogram with strong peaks even when the sample data is tilted and the histogram peak separation is misleading.

There is no particularly easy solution to this problem, but understanding it helps in avoiding errors. In particular the section profiles should always be double checked to be truly flat. AFM software often provides a method for highlighting data of a certain height. By changing the selected height systematically, it may be possible to tell if the steps are flat. This is described further below, in section 2.3.1.3.

Suzuki *et al.* have published a reference on step-height measurement and AFM standards.[81] A fairly robust procedure for preparing the sample data is described, though it may not be possible to duplicate exactly with all AFM software. Their paper describes the use of a silicon surface with steps to calibrate the AFM z-axis. An alternative reference standard is an 8 nm step sample available from VLSI Standards Inc. (model no. SHS-80QC) for approximately $3000.

2.3.1.3 *Recommended protocol*

The recommended best practice is to use the Gwyddion software package, available for free at `http://gwyddion.net`, and, after doing the basic image clean-up described in section 2.3.1.1, add a mask to as large an area of a step as is possible. Then fit a plane to the masked area on that step and apply the correction to the image; a choice must

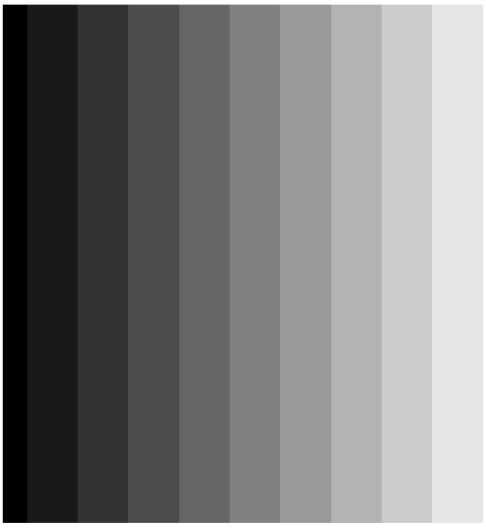

(a) Simulated

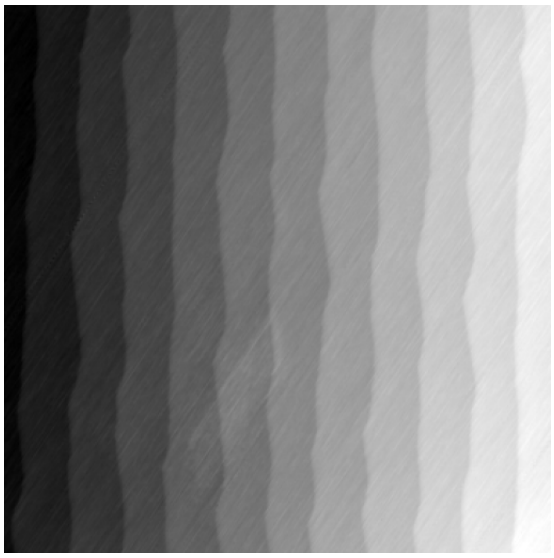

(b) Real

Figure 20: Atomically terraced surfaces. (a) An ideal simulated surface. Each step is assigned a height of 1 Å, and the image width is 1 µm. This corresponds to a simulated wafer miscut of about 0.06°. (b) An AFM image of a real sample surface with atomic steps. The steps are about 3.5 Å tall and the image width is 3.5 µm. The wafer miscut is also 0.06°.

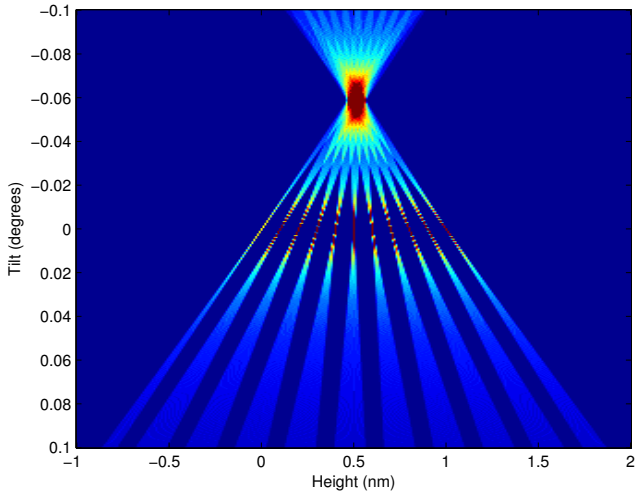

(a)

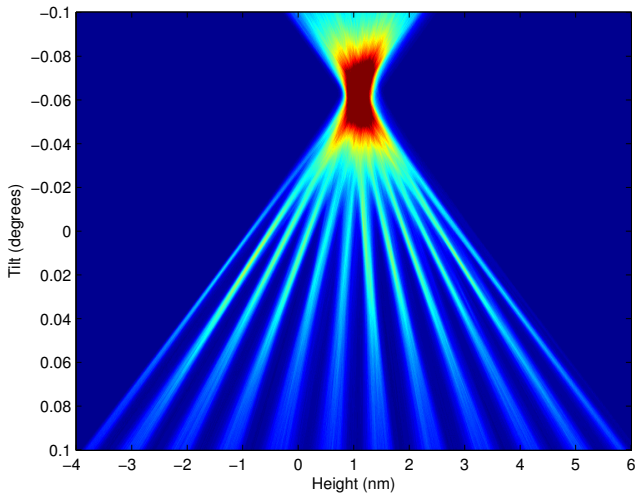

(b)

Figure 21: Tilt-histogram maps generated from the surfaces in figure 20. See the text for a description. (a) The map generated from the simulated surface in figure 20a. The histogram at zero tilt is a series of sharp spikes, as expected. (b) The map generated from the real AFM-measured surface shown in figure 20b. In this case it is difficult to tell where the histogram is maximally sharp, as there is little variation over a relatively wide range of tilts. The colour scales are linear.

be made between plane subtraction and image rotation, but this is unlikely to make much difference in this case. This is an improvement over another technique of fitting a plane to three points, or three small averaged circles, using the three-point tool, because it generally allows averaging over a larger area. The levelling can be checked in two ways: by using the profile extraction tool, taking advantage of the ability to average over a thick line; and by using the "mark grains by threshold" tool. This tool allows you to highlight regions of the image above or below a certain threshold. By changing the height threshold, you can see how the steps "fill" in as you change the level. The entire step should change colour at the same time when adjusting the threshold.

After the image is levelled, the step height can be extracted using the histogram or by using the section tool and averaging the trace over as wide a line thickness as possible. If the steps have been rotated such that the edges lie parallel to the y-axis, then using the "row/column statistics" tool can effectively average over a section line as wide as the entire image. Choosing the median mode, rather than mean, helps eliminate the effect of particles etc. on the surface. Gwyddion also provides a "critical dimension" tool that enables fitting the step heights with a curve-fitting algorithm. The numerous step-height values collected by these methods can then be averaged and the standard deviation can provide an estimate of the statistical error, but it must be kept in mind that the effect of any remaining sample tilt will not be averaged out.

2.3.1.4 *Sapphire step-height results*

AFM images of annealed sapphire surfaces have been analyzed many times. Unfortunately, as mentioned above, the data-processing steps influence the results, making it difficult to be sure of the true step-height values and increasing error estimates. A more thorough study would be possible, but all indications are that the step heights for R- and C-plane sapphire are consistent with the expected values from literature of 3.5 Å for R-plane, the R-plane spacing, and 2.2 Å for C-plane, the c-axis lattice constant divided by six. When reporting step heights from AFM images, an error estimate of at least 0.5 Å is likely warranted.

2.3.2 *X-ray miscut and tilt measurements*

The miscut of a wafer can be measured by AFM, but, as described in section 2.3.1, this procedure can be inexact. Another way to measure the miscut is to use an x-ray diffractometer. This method also allows determination of the tilt of an epitaxial film with respect to the substrate.

The general procedure is to measure the angular position, ω, of a diffraction peak several times, rotating the sample about the surface normal, *i.e.* the ϕ axis, between each measurement. Unfortunately any misalignment in the positioning of the sample in the diffractometer will affect the results. This problem can be overcome by "zeroing" the sample before each measurement by measuring a specular x-ray reflection at a very low incident angle, around about 0.3°, and adjusting the axis zero positions as necessary. Once this is done, the angular position of the diffraction peak from the sample will vary sinusoidally with rotation. The miscut of the wafer is equal to the amplitude of the sinusoid.

By measuring both a substrate and a film diffraction peak at each rotational step, the film tilt can also be measured. Figure 22 shows a schematic diagram of the film and substrate lattices. Figure 23 shows tilt/miscut measurements from a Y_2O_3 film grown on a sapphire substrate. The two curves are in phase, indicating that the film is tilted along the same direction as the substrate miscut. The film tilt is simply the difference between the sine wave amplitudes. Since the film curve has less amplitude, the tilt is towards the surface normal. This direction is expected from a simple stress minimization argument: the film tilts towards the "empty space" at each step edge. More rigorous analysis of shear stress and resulting dislocations is possible but somewhat complicated.[82]

The miscut determined from the fit to the substrate data in figure 23 was $(0.0580 \pm 0.0007)°$. For comparison, consider an AFM image with a step height of (3.5 ± 0.5) Å and 346 nm wide steps. This would lead to a miscut of $(0.058 \pm 0.008)°$, with more than 10 times the uncertainty of the x-ray measurement. The film tilt determined from the x-ray data is $(0.005 \pm 0.004)°$. The error is large because of the wide film x-ray peaks.

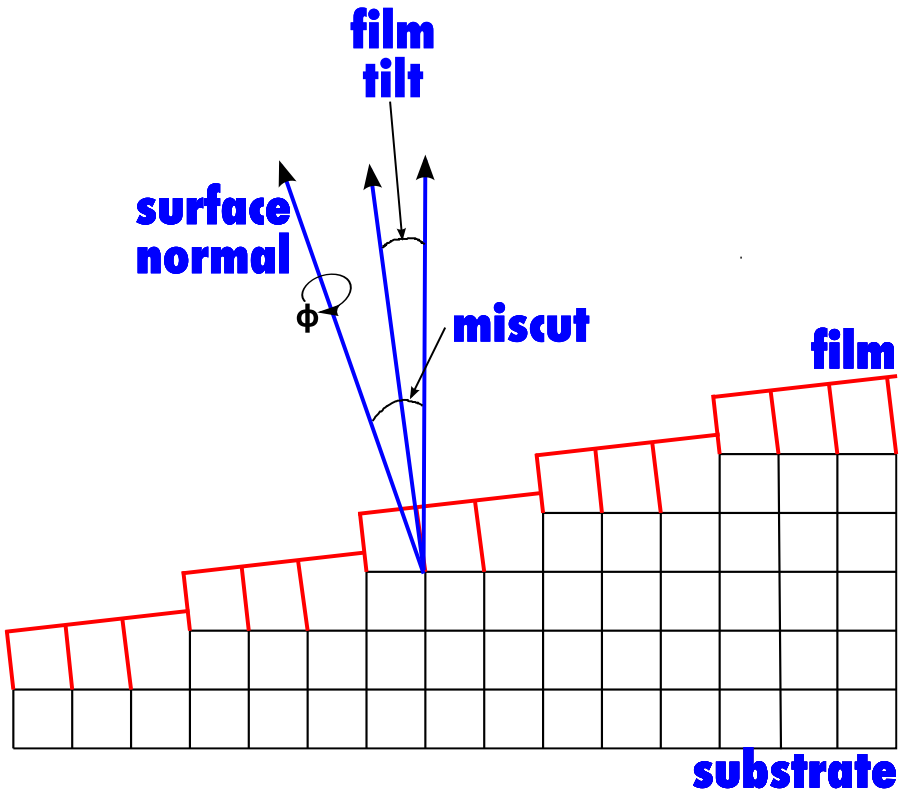

Figure 22: Schematic diagram of a film crystal lattice on a substrate. The substrate shows atomic steps due to miscut, and the film is tilted towards the surface normal.

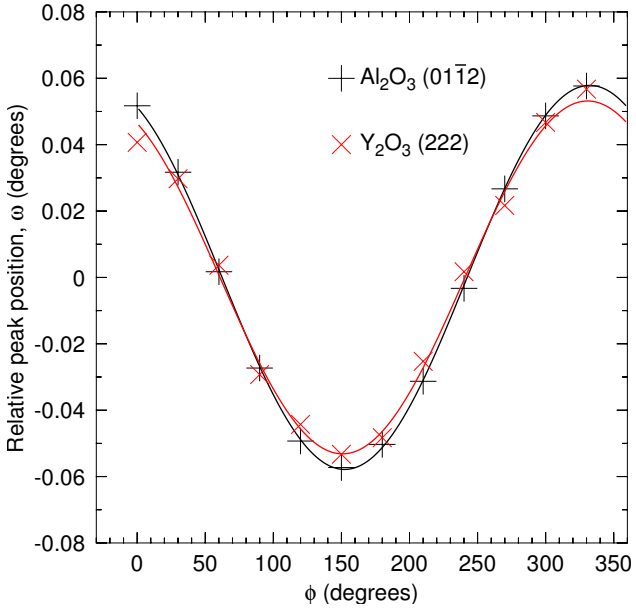

Figure 23: X-ray diffraction measurement of substrate miscut and film tilt for a Y_2O_3 film grown on an R-plane sapphire substrate. The miscut is the amplitude of the substrate sine wave, and the film tilt is the difference between the two amplitudes. The solid lines are fits to the data points.

2.4 GROWTH TECHNIQUES

Samples were grown in a VG V80H MBE system designed for semiconductor growth but modified for oxide growth with the addition of a high-throughput turbomolecular pump with a pumping speed of 2300 L/s, although this was diminished somewhat by tubulation. The turbopump was used to augment the stock cryopump. A serpentine SiC substrate heater purchased from Morgan Advanced Ceramics was also installed. Effusion cells loaded with elemental charges were used, including a high-temperature cell capable of operation at 2000 °C for yttrium. An in-house-designed 200 W variable-frequency plasma source was used for oxygen and hydrogen, but it was not usually energized.[83] Sample growth was performed with liquid nitrogen in the growth chamber shroud, but subsequent experiments have shown this to be unnecessary, as switching the coolant to water caused no noticeable change in sample characteristics.

2.4.1 *Light scattering*

The system was equipped with a Staib RHEED system as well as a light-scattering sample-monitoring system. The 457.9 nm line of an argon-ion laser was used in the light-scattering apparatus. Thin-film interference oscillations in the specular reflection signal provide a convenient measure of the film thickness, while the diffuse signal can be used to glean information about surface roughness. The specular signal will oscillate with a period, Λ, given by

$$\Lambda = \frac{\lambda}{2n\cos\alpha}, \tag{2.2}$$

where α is the angle with respect to the normal of the beam inside the film, n is the film index, and λ is the free-space laser wavelength. Substituting with Snell's law, we find

$$\Lambda = \frac{\lambda}{2n\cos(\arcsin(\frac{\sin\theta}{n}))}, \tag{2.3}$$

where θ is the angle of incidence of the laser beam on the film (with respect to the normal). For our system, with λ =457.9 nm, θ =36.5°, and $n = 1.9$ we find Λ =127 nm. Figure 24 shows example specular reflectivity data from a Y_2O_3 film showing thickness oscillations.

2.4.2 *Substrate temperature measurement*

As the growth of refractory materials such as Y_2O_3 requires high temperatures, some extra attention to the issue of substrate heating is warranted. Figure 25 shows a schematic of the heating system used in the sample growths. The substrates are held onto a molybdenum holder by tantalum wires; a schematic of the holder is shown in appendix D. The substrate is positioned above a square hole in the holder, allowing direct exposure of the back to radiation from the heater. Outside the substrate location, the 90 mm diameter holder is covered by a spot-welded tantalum heat shield to reduce power consumption and chamber heating. A thermocouple mounted between the heater filament and substrate holder allows temperature feedback control. The thermocouple reading is not an accurate indicator of the substrate temperature, as it measures a higher temperature intermediate between that of the heater and that of the sample.

The substrate temperature was calibrated by measuring the spectrum of the thermal radiation emitted out the front of the substrate.

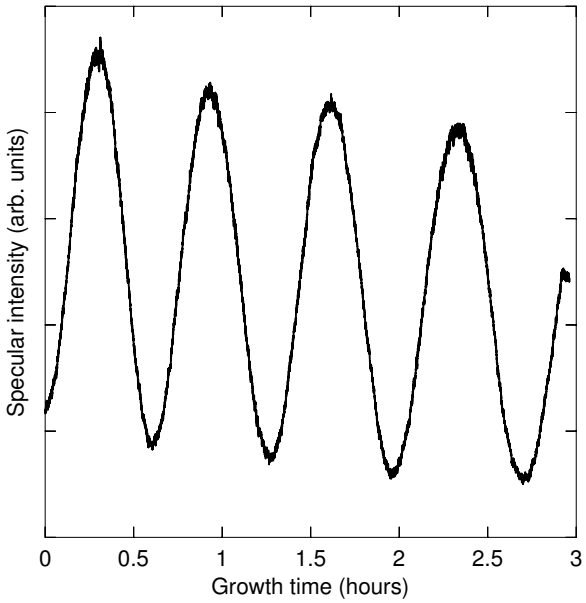

Figure 24: Specular reflectivity at 457.9 nm of a Y_2O_3 sample grown on sapphire. Each oscillation corresponds to 127 nm of film growth. In this case the approximately 4.25 oscillations give a film thickness of about 540 nm, grown at a rate of around 180 nm/hr.

Since sapphire has low absorption in the wavelength range of interest, it transmits the heater radiation. Metallizing the substrate prevents the heater radiation from being transmitted through the substrate and interfering with the substrate temperature measurement. Therefore, the back surface of the sapphire substrate was coated with 200 nm of chromium for adhesion followed by 200 nm of molybdenum. The coatings were deposited in an electron beam evaporator system from elemental sources, at rates around 1 Å/s.

Figure 26 shows radiation data collected from a substrate at three different temperatures. A double-side polished substrate was used for this work to simplify the modelling. The temperature was determined by fitting the data to a graybody expression given by

$$I(\lambda, T) = \frac{A\varepsilon(\lambda)}{\lambda^4(e^{\frac{hc}{\lambda k_b T}} - 1)}, \tag{2.4}$$

where I is the thermal radiation intensity, λ is the wavelength, T is the temperature, A is a fitting parameter, ε is the wavelength dependent spectral emissivity, h is Planck's constant, c is the speed of light, and k_b is the Boltzmann constant. The spectral emissivity values were

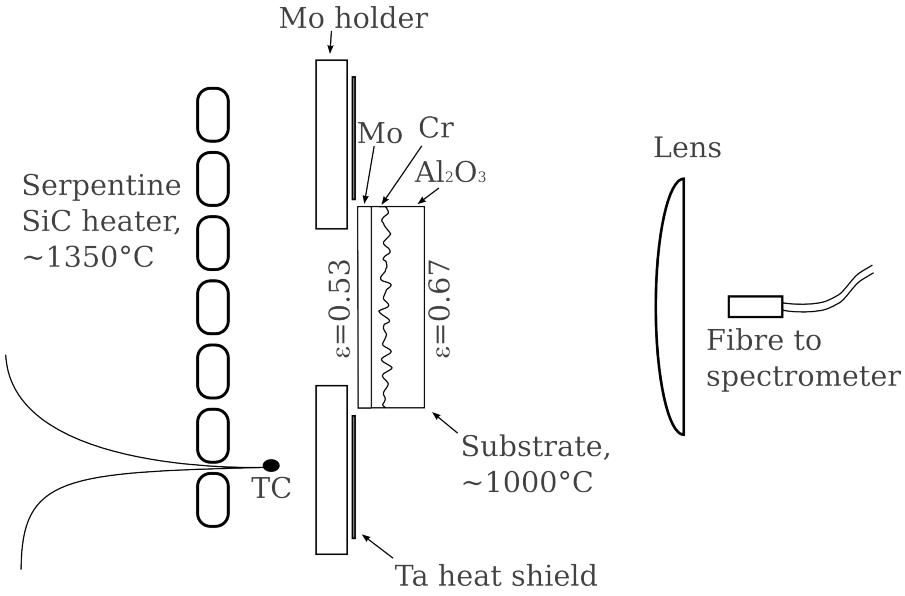

Figure 25: A schematic of the system used to heat substrates in the MBE. The estimated emissivities, ε, of the front and back surfaces of the metallized sapphire substrate are indicated. The rough rear surface of a single-side polished substrate is depicted here. TC stands for thermocouple. The lens and fibre were placed outside the MBE and used to capture data for pyrometry (see text).

calculated for a chromium-coated sapphire multilayer using data from Weaver *et al.*[84] Using Fresnel's equations, the emissivity of the front of the substrate, ε_f, was found to be

$$\varepsilon_f = 1 - R_f \quad \text{with} \tag{2.5}$$

$$R_f = |r_f|^2, \tag{2.6}$$

$$r_f = \frac{r_{01} + r_{12}}{1 + r_{01} r_{12}}, \tag{2.7}$$

$$r_{01} = \frac{1 - n_{Al_2O_3}}{1 + n_{Al_2O_3}}, \quad \text{and} \tag{2.8}$$

$$r_{12} = \frac{n_{Al_2O_3} - n_{Cr}}{n_{Al_2O_3} + n_{Cr}}. \tag{2.9}$$

$$\tag{2.10}$$

$n_{Al_2O_3}$ and n_{Cr} are the indices of refraction for sapphire and chromium. The actual temperatures of the substrate for thermocouple readings of 1200, 1120, and 1080 °C were determined to be 985, 905, and 850 °C, respectively. The heater temperature was determined by measuring the spectrum of the radiation transmitted through an unmetallized substrate. With a thermocouple reading of 1200 °C the heater temperature was found to be 1350 °C.

To better understand the factors that control the substrate temperature, we derived a relationship between the substrate and heater temperatures using Stefan's law for the emitted and absorbed radiation. We assume that the heater and substrate are parallel plates, that the system is in thermal equilibrium, that there are infinitely many bounces of radiation between the heater and substrate, and that there is no conductive or convective heat transfer. We find that

$$T_{substrate} = T_{heater} \sqrt[4]{\frac{\varepsilon_b \varepsilon_h}{(\varepsilon_b + \varepsilon_f)\varepsilon_h + (1 - \varepsilon_h)\varepsilon_f \varepsilon_b}}, \tag{2.11}$$

where ε_h, ε_f and ε_b are the emissivities of the heater, front, and back of the substrate, respectively. Using emissivity values at 2 µm (close to the radiation peak) of ε_f=0.36 and ε_h=0.8 [84, 86] as well as the measured substrate and heater temperatures of 985 and 1350 °C, we can estimate the back surface emissivity to be 0.20, which is larger than the theoretical value of 0.04 for molybdenum. This is consistent with our observation that the back surface becomes less reflective after heat treatment, owing to high-temperature oxidation, surface roughening, or evaporation of SiC heater material onto the substrate.

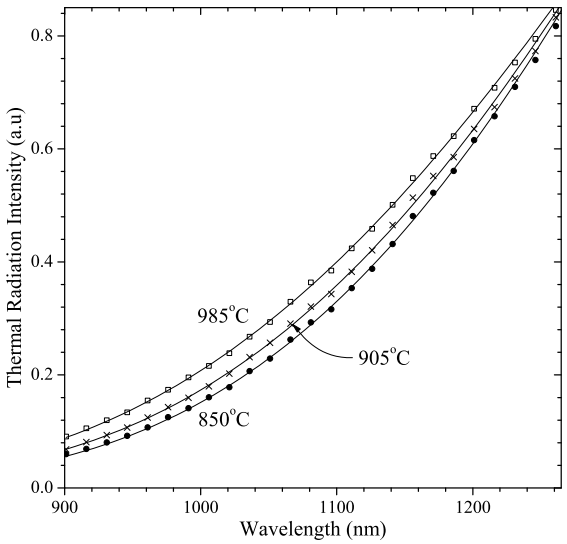

Figure 26: Wavelength dependence of the thermal radiation from a metallized, double-side polished, sapphire substrate. Points indicate measured data while lines correspond to fits of equation 2.4. For the spectra with temperature fits yielding 985, 905, and 850 °C the thermocouple temperature sensor reading was 1200, 1120, and 1080 °C, respectively. Figure courtesy Raveen Kumaran.[85]

The assumption of infinite bounces of radiation between the heater and the back of the substrate is not strictly correct. Some of the radiation will be absorbed by the substrate holder or lost to the chamber. Additionally, the substrate holder itself will be radiating. A proper treatment of these effects is much more complicated and not considered here. We believe that our assumption is reasonable because the substrate and heater are in close proximity. An alternative simple assumption to make would be to assume that all reflected radiation is lost. In that case the terms in the heat balance are simply the radiation absorbed by the substrate from the heater directly, the radiation out the back of the substrate, and the radiation out the front of the substrate. Using the same values as above, this method leads to a calculated back surface emissivity of 0.30. However, this alternative method is not a good candidate for the "opposite extreme" assumption. The subtleties present in the interaction between the heater, substrate, and substrate holder are difficult to predict.

An integrating sphere was also used to measure the emissivity of various materials for consideration in our heating scheme. The sample to be measured was inserted into one port of the sphere and a silicon photodiode was inserted into another. 1047 nm light from a Nd:$LiYF_4$

laser was introduced through a third port and bounced off the sample, with any specular reflection subsequently hitting the sphere material. By varying the laser power and monitoring the photodiode response we can measure a reflectivity curve. Comparison with an aluminum mirror as a known standard allowed the elimination of experimental errors arising from the sphere. The emissivity was taken to be one minus reflectivity, and the measured values are shown in figure 27. Unfortunately the wavelength of the laser was not the same as the desired wavelength of around 2 µm for use in the heater setup, and very slight variations in surface properties, including those that occur during heating, can cause large changes in emissivity. The substrate measured in the integrating sphere was single-side polished and therefore can not be directly compared to the double-side polished sample used in the analysis above. As shown in figure 27, the measured values for the front and back surface emissivities of the metal-coated, single-side-polished substrate were 0.67 and 0.53, compared with the values of 0.36 and 0.20 discussed above. These discrepancies are large, but could be accounted for given the differences between the two situations. In particular we would expect the fact that the substrate in the integrating sphere had a rough back surface to increase the emissivity, as measured, but that the non-heat-treated metal would result in a lower emissivity. It is difficult to predict the net result without further experimentation. Despite some of these practical considerations, the integrating sphere method can allow for good comparisons between different material options.

2.5 SUMMARY

In this chapter we have reviewed a number of techniques that are important for our crystal growth experiments. Producing atomic steps on sapphire substrates by annealing provides an extremely uniform surface for epitaxial growth. Substrate cleaning procedures then ensure that this surface is not contaminated. Sapphire is an important substrate material for oxides as well as other materials such as GaN, so these techniques are widely applicable. Our structural characterization methods allow us to quantify properties such as atomic step width and height that may be important to the growth process, and are useful for a wide variety of materials. Finally, the use of light scattering and optical temperature monitoring during growth allow us to properly control the process in a repeatable manner. Absolute temperature measurement is a challenge associated with wide-bandgap substrates

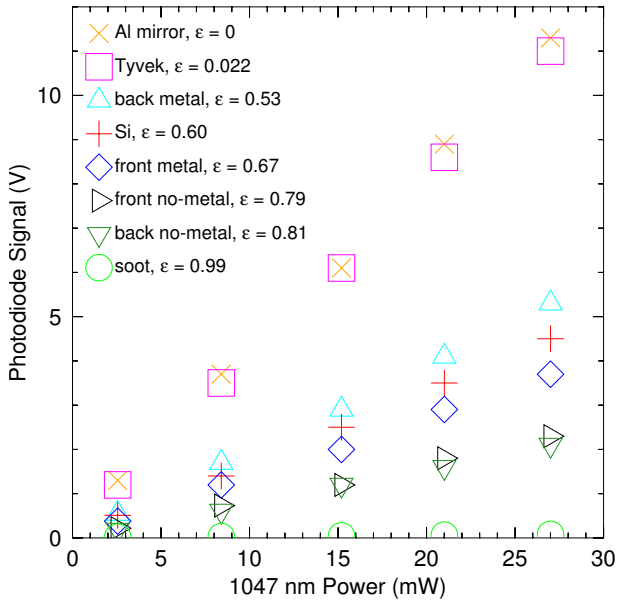

Figure 27: Reflectivity (and therefore emissivity) measurements for a variety of substances. The vertical axis is the signal proportional to reflectivity. The emissivity values are shown in the legend. "Front" and "back" refer to sides of a single-side polished sapphire substrate and "metal" and "no-metal" refer to whether the back side of that substrate was coated in the standard 200 nm Cr and 200 nm Mo. In all cases the relationships are linear, as expected.

for which bandgap thermometry is not possible. Our analysis of this problem should prove helpful to others using these materials.

3 Annealing of Y_2O_3 films on sapphire

In the previous chapter we described the annealing of sapphire substrates before the growth process. Here we investigate the annealing of the grown films to see if we can improve them and to determine how we can influence their properties in general. We may be able to improve the film surface morphology as in the case of the substrates, for instance. Additional possible changes include increasing film density to bulk levels and removing oxygen vacancies by further oxidizing the film in air. We may also be able to learn about interdiffusion between the film and substrate, and the stability of rare-earth dopant distributions at high temperature.

Most of the yttrium oxide films were grown on annealed sapphire substrates, for reasons discussed in section 2.1, but some early films were grown on (100) oriented silicon and unannealed sapphire. The growths on silicon are not reported on here, but we will review the results of growths on unannealed and annealed sapphire before discussing the film annealing experiments.

3.1 Unannealed sapphire substrates

A series of 12 growths were performed on unannealed sapphire of all four standard orientations shown in figure 8, with three thicknesses per orientation of around 80, 500, and 1000 nm. The substrate temperatures were 1000 °C with yttrium fluxes of 2.6×10^{-7} torr and oxygen fluxes of 2.6×10^{-6} torr. The growth rates were around 350 nm/hr. Further details on growth conditions can be found in chapter 4. Samples grown on R-plane $(01\bar{1}2)$ substrates showed the lowest surface roughness overall as measured by AFM, as well as the smallest peak widths measured by x-ray diffraction. Table 2 shows the roughness and x-ray results. On A-, C-, and M-plane substrates the thin films showed unusual linear features of unknown origin on the film surface, as seen in figure 28a. Films on all substrate orientations eventually developed characteristic pyramidal structures with sufficient film thickness. Figure 28b shows a 1000 nm thick Y_2O_3 sample grown on M-plane sapphire. X-ray ω–2θ scans from films grown on A-, C-, and M-sapphire showed primarily {111}-oriented Y_2O_3 but also some peaks from other Y_2O_3 orientations. These subsidiary peaks were not seen in growths

	A	C	M	R
AFM RMS roughness (nm)	22	19	28	17
X-ray ω–2θ FWHM (°)	0.133	0.137	0.138	0.129
X-ray ω FWHM (°)	1.27	1.66	5.97	1.26

Table 2: Data from unannealed 1 µm thick Y_2O_3 films on varying orientations of unannealed sapphire. The x-ray widths are from the Y_2O_3 (222) peaks.

on annealed R-plane sapphire substrates, further increasing R-plane's status as the "best" orientation for sapphire.

3.1.1 *Refractive index*

Several Y_2O_3 films were analyzed with an ellipsometer from J.A. Woollam Co. generously provided by A. Macfarlane. This spectroscopic ellipsometer measures how the polarization of light is changed on reflection from the sample at a variety of wavelengths. Data analysis allows determination of the wavelength-dependent index of refraction of the film, film thickness, and surface roughness.

The ellipsometry was performed near the Brewster angle for Y_2O_3 because this maximizes sensitivity. Near the Brewster angle the difference between reflection of s- and p-polarized light is maximized, and the phase shift is rapidly varying.[87] A Cauchy material model was found to provide the best results for modelling the Y_2O_3 layer. The model used for the wavelength-dependent index of refraction was

$$n(\lambda) = A + \frac{B}{\lambda^2} + \frac{C}{\lambda^4}, \tag{3.1}$$

where A, B, and C are fitting parameters. A surface roughness layer consisting of a mix of 50% Y_2O_3 and 50% air was used along with index of refraction data for sapphire from the literature.

As shown in figure 29 our Y_2O_3 had an index of refraction of 1.85 at the most common Nd:YAG wavelength of 1064 nm, similar to literature values that are around 1.90 for bulk yttria and lower for thin films.[42] The index was nearly constant for greater wavelengths. The fact that the real index was lower than the bulk value likely indicates that our film was not 100% dense. The measured imaginary, absorptive, part of the index was low, less than 10^{-5} above 900 nm. The thickness of this film was found to be 1073 nm with a 16 nm interfacial roughness layer. This thickness value is consistent with data from specular light

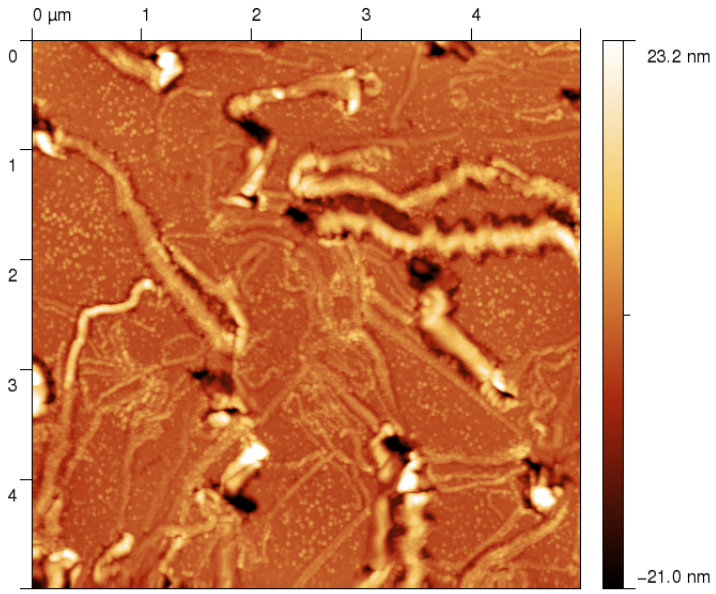

(a) 80 nm on A-Al_2O_3

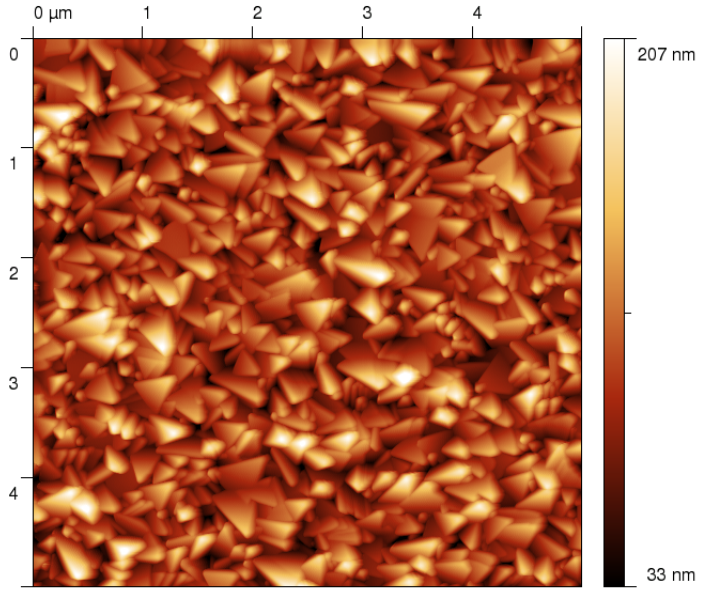

(b) 1000 nm on M-Al_2O_3

Figure 28: AFM images of unannealed Y_2O_3 films grown on unannealed sapphire substrates. (a) An 80 nm thick film on A-plane sapphire with linear features seen in yttria films grown on A-, C-, and M-plane sapphire substrates. (b) A 1000 nm film on M-plane sapphire with pyramidal structures that were very common for thick yttria films.

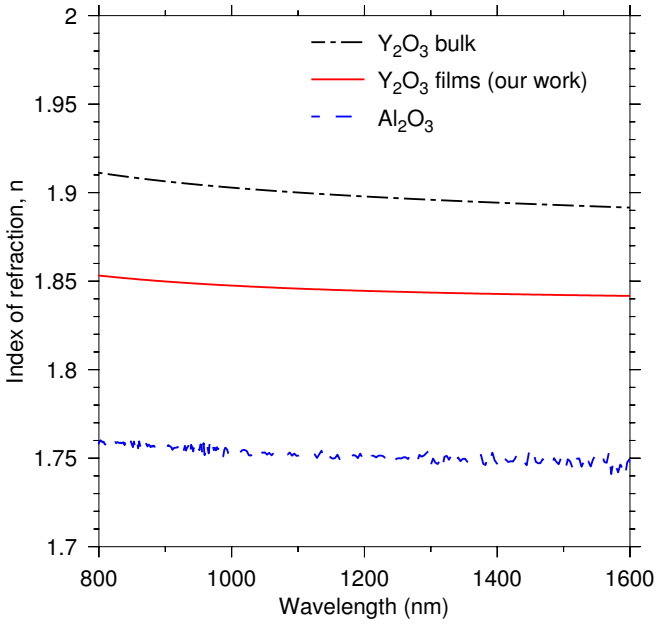

Figure 29: Real index of refraction, n, for an approximately 1 µm thick Y_2O_3 film (solid, red), bulk Y_2O_3 (dash-dot, black) and a sapphire substrate (dashed, blue). Our thin film yttria results are shown as a fit to equation 3.1 and the bulk data is from a Sellmeier fit.[42] The substrate data has increased noise due to imperfect modelling of reflections from the rear substrate surface, but matches literature data well.[88]

scattering collected during growth, as described in section 2.4.1, which predicted 1080 nm. The roughness layer thickness was the same as the RMS roughness value measured with AFM.

3.2 ANNEALED SAPPHIRE SUBSTRATES

Because a motivating factor for this research was the growth of laser materials that need to be suitably thick for waveguiding purposes, numerous "thick" samples were grown on annealed R-plane sapphire after the study on unannealed substrates was concluded. The thickness needs to be on the order of the lasing wavelength, so a thickness of approximately 1 µm was chosen. R-plane was selected, as it showed the most promise in the unannealed trials. Growths on annealed C-plane sapphire did not show the same improvements noted when moving to annealed R-plane substrates.

Figure 30 shows an AFM image of an unannealed ~1 µm Y_2O_3 film on annealed R-plane sapphire. In contrast to figure 28b the surface is mostly very smooth with some larger pyramidal structures. Figure 31

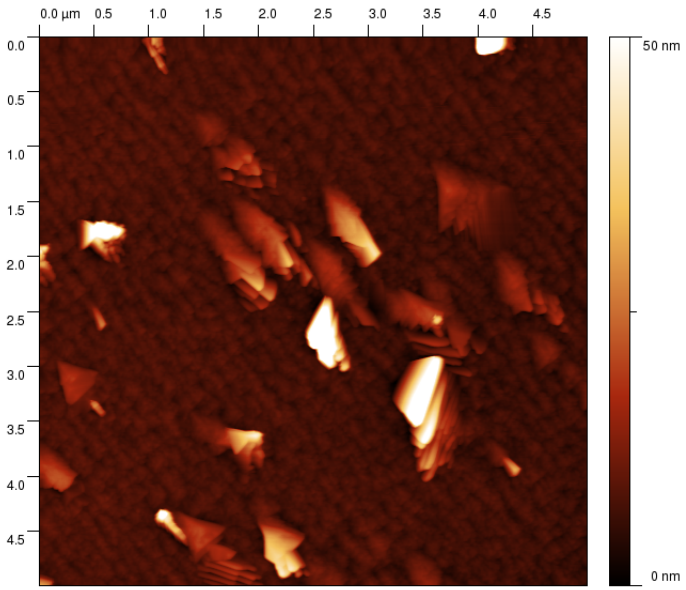

Figure 30: AFM image of an unannealed 1 µm thick Y_2O_3 film grown on annealed R-plane sapphire. Some of the characteristic pyramids seen in figure 28b are visible on a much smoother background.

shows an x-ray reciprocal space map of the Y_2O_3 (222) peak from the same film pictured in figure 30. The peak is narrow in the out-of-plane ω–2θ direction, indicating very homogeneous plane spacings, but wide in the in-plane ω direction, indicating that a variety of "tilts" are present in different regions of the film. This film had Y_2O_3 (222) peak widths in the ω–2θ and ω directions of 0.0144° and 0.751° respectively, compared with the values in table 2 of 0.129° and 1.26° for a film grown on an unannealed R-plane substrate.

3.3 POST-GROWTH FILM ANNEALING

Annealing is a common process for both metallurgy and thin-film studies where heat is used to alter material properties. For thin-film semiconductors a brief period at high temperature seems to allow atoms to move to optimal positions, eliminating some defects created during growth.[89] An example treatment for III-V semiconductors would be 1 minute at 800 °C. We annealed our films in air to study how they changed and to see if certain properties could be improved. Higher temperatures and longer annealing times than for semiconductors were used, as described below, which was reasonable, given the

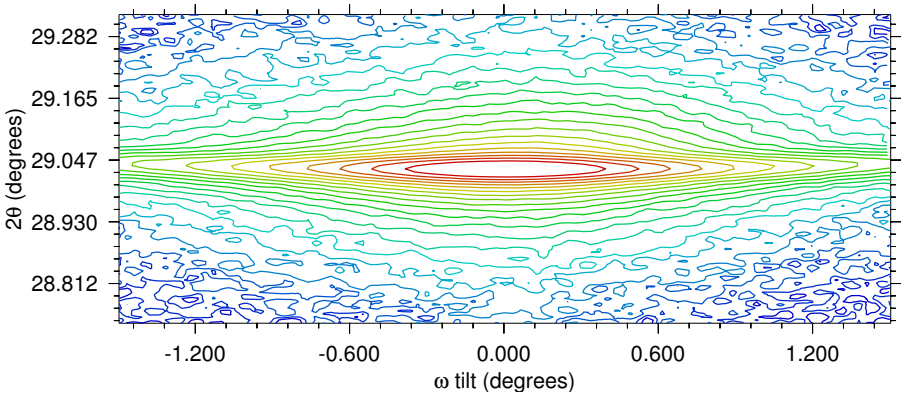

Figure 31: Reciprocal space map of an unannealed 1 µm thick Y_2O_3 film grown on annealed R-plane sapphire. This map is plotted with axes in degrees rather than reciprocal lattice units. The vertical direction is the out-of-plane direction, perpendicular to the sample surface, and the axis shows the 2θ position during the ω–2θ scan. The horizontal direction is in-plane, with the axis showing the ω tilt used during the ω–2θ scan. See section 1.5.3.1 for a more detailed description. Logarithmic contours are used.

much higher bond energies present in Y_2O_3 compared with typical semiconductors. ΔH is around 1900 kJ/mol for Y_2O_3 but only about 70 kJ/mol for GaAs.[90, 91]

Three "thin" films, 20, 66, and 69 nm, and one "thick" 600 nm film, of Y_2O_3 grown on annealed R-plane sapphire were annealed under various conditions. X-ray diffraction results as well as AFM measurements of surface features were compared from before annealing to after each annealing step. The thick film was doped with around 1% Nd, and for this film photoluminescence measurements were also tracked.

3.3.1 *Initial annealing trial*

The first experiments involved annealing two films at 1150 °C for nine hours in air. This regimen was selected, somewhat arbitrarily, as it was the same as that used for the pre-growth anneal of the substrates. A long duration was desired to ensure changes in the films were likely to be noticed. Before annealing, the metal coatings on the back of the substrate were removed to eliminate contamination of the oven and film. The film was attached to a glass slide with Crystalbond version 509 from SPI Supplies and the metal coating removed with wet sandpaper. The Crystalbond was then removed by heating in acetone. Figure 32a shows the surface of a 69 nm thick film before

annealing. Any organic remnants from the Crystalbond process would be removed during the annealing process by the high temperatures.

After the long anneal the surface was re-imaged with AFM, as shown in figure 32b. The difference is striking. The atomic steps have changed into "blobs" with much higher amplitude. Material has diffused around on the surface and it appears that this new structure is energetically preferred. Figure 33 shows a before and after comparison of ω–2θ x-ray diffraction scans from the 69 nm thick Y_2O_3 sample. The primary changes are the apparent shift of the Y_2O_3 (222) peak to higher angle, indicating a smaller lattice spacing, and the appearance of a subsidiary peak at slightly higher angle still, which may correspond to the yttrium aluminum monoclinic (YAM) phase, $Y_4Al_2O_9$, (023) peak. Another small peak that may correspond to the yttrium aluminum perovskite (YAP), $YAlO_3$, (004) peak is also present.

A second Y_2O_3 film was annealed under the same conditions as above. This film was 20 nm thick. Before annealing the surface looked very similar to that of the 69 nm sample depicted in figure 32a; figure 34 shows AFM images from this sample taken after annealing. Figure 35 shows x-ray diffraction results. The AFM results are similar to the 69 nm sample, with what appear to be atomic steps visible on the "blobs." The x-ray results are somewhat different, though the main Y_2O_3 (222) peak shift appears to be similar.

Perhaps unfortunately, the changes seen here from annealing do not appear to be beneficial. The surface is rougher, and pendellösung finite thickness fringes visible on the initial Y_2O_3 (222) peak in figure 35 are absent in the annealed spectrum. The single-phase Y_2O_3 film has become a mixture of different Y-Al oxide phases and orientations. Nevertheless, the desired outcome of witnessing film changes after annealing was achieved, and understanding the evolution of film properties under annealing could prove interesting in its own right.

3.3.2 *Detailed step-wise annealing experiments*

3.3.2.1 *66 nm thick Y_2O_3 film*

After determining that annealing can certainly affect the nature of the Y_2O_3 film, further experiments were performed to gain more insight into the process. Another thin film, 66 nm thick, was annealed, but this time in a series of smaller steps. The sample was first annealed at 800 °C for four hours, then at 900 °C for another four hours, and so on, increasing 100 °C in each step. The final anneal temperature

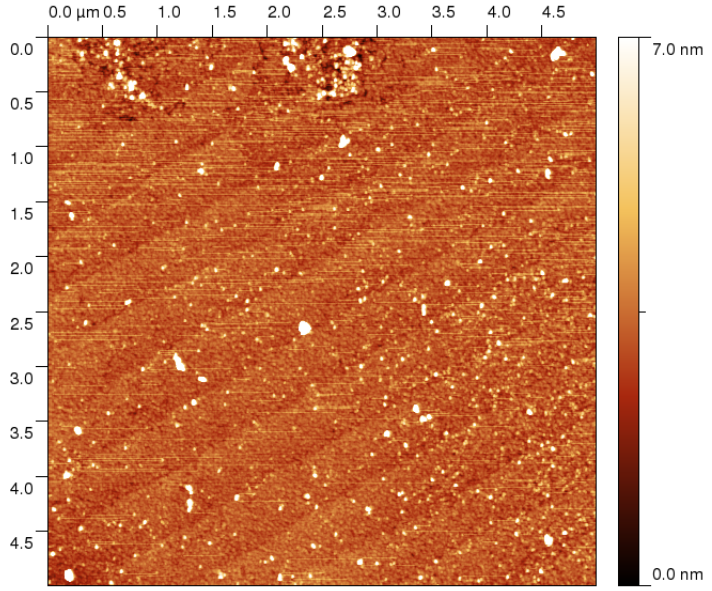

(a) Before

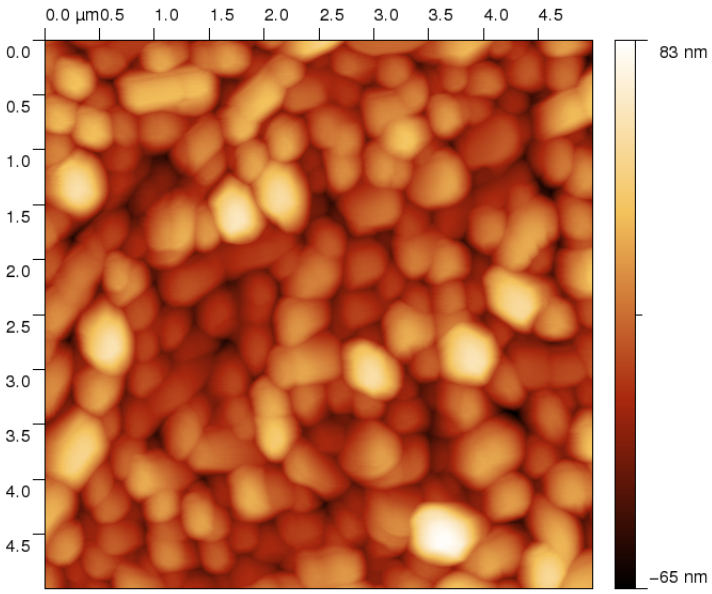

(b) After

Figure 32: AFM images of a 69 nm thick Y_2O_3 film grown on annealed R-plane sapphire. (a) Before annealing. The steps are more difficult to see than usual and the surface is more contaminated because of Crystalbond on the surface (see text). (b) After annealing at 1150 °C for nine hours.

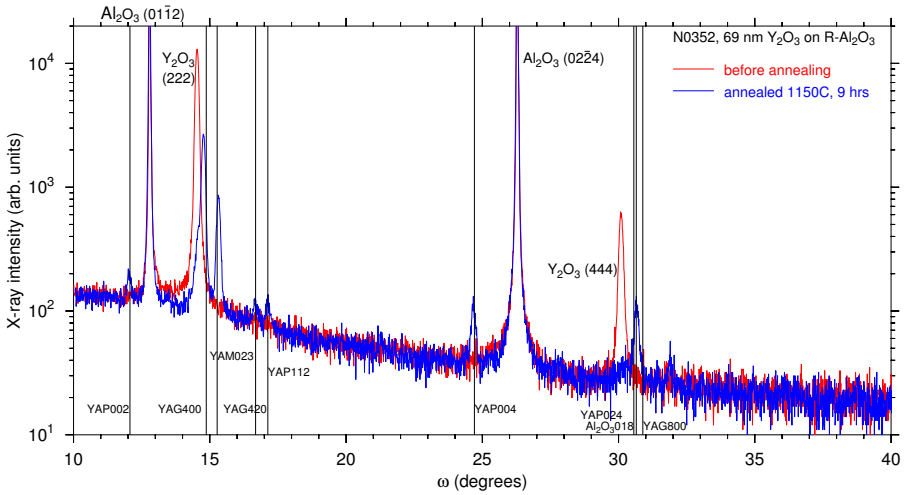

Figure 33: ω–2θ x-ray diffraction scans from a 69 nm thick Y_2O_3 film grown on annealed R-plane sapphire, before and after annealing at 1150 °C for nine hours. Vertical black lines indicate expected positions of x-ray peaks from the literature. The tall clipped peaks are from the substrate, and the other prominent peaks in the "before" spectrum are Y_2O_3 {111}.

was 1400 °C. Figures 36–39 show the sequence of AFM images from this annealing experiment. The surface morphology changes seen here are not overtly similar to the results from the previous annealing experiments. After the first anneal the stepped appearance is gone, replaced with small "blobs" that are much smaller than with the previous anneals. After the 1000 °C anneal the blobs appear to be coalescing, but the image from the 1100 °C stage is quite similar to the 900 °C image. It is possible that some inhomogeneity across the sample is present here, with different areas being accidentally imaged in the different steps. The 1200 °C image shows clear coalescence, followed again by smaller features at 1300 °C. The 1400 °C image shows interesting rectangular features with atomic steps, in clear contrast with previous images in this series, though perhaps similar to those seen in figure 34b.

Figure 40 shows x-ray diffraction scans from each stage of the annealing process for the 66 nm thick film. At 1000 °C new peaks appear at 14.8 and 15.3°, to the right of the Y_2O_3 (222) peak position. In this scan a shoulder is visible on the low-angle side of the 14.8° peak. It is possible that the shoulder is all that remains of the (222) peak. At 1100 °C the shoulder is gone. As the annealing temperature is further increased, the two new peaks disappear and are replaced with others at higher angle. These subsequently also start to fade away.

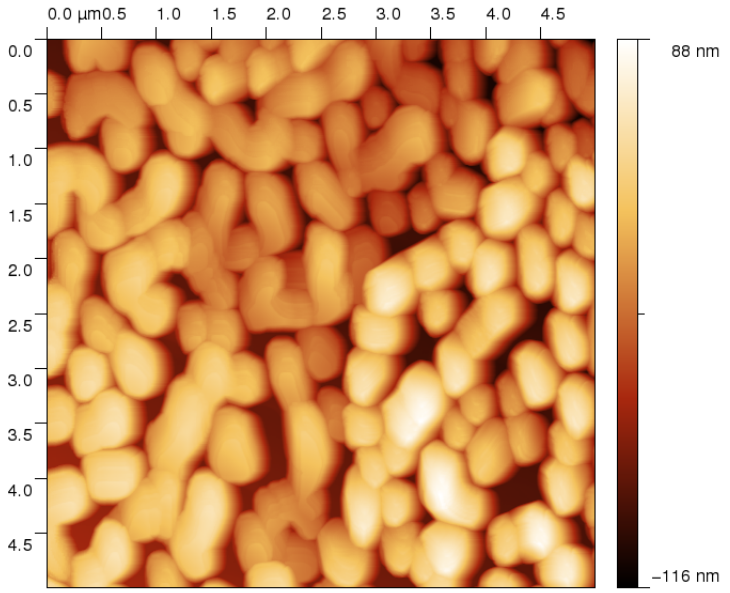

(a) 5 µm×5 µm scan

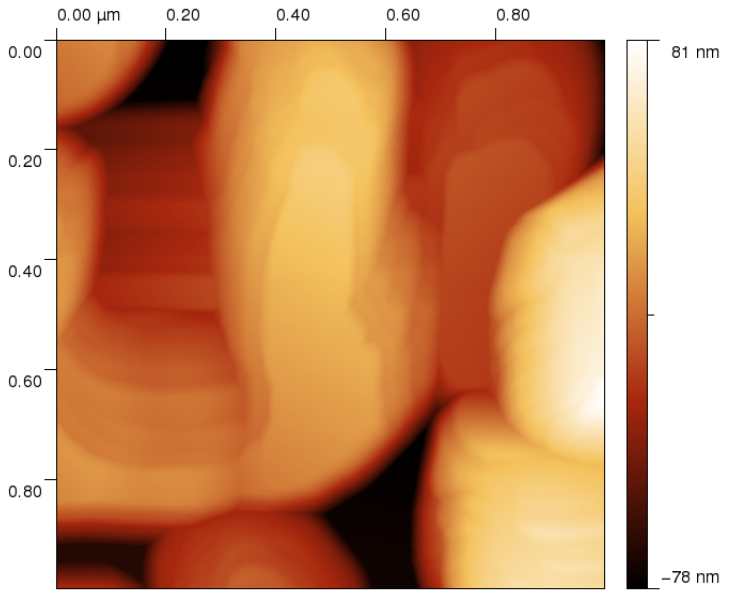

(b) Close-up 1 µm×1 µm scan

Figure 34: AFM scans of a 20 nm thick Y_2O_3 film after annealing at 1150 °C for nine hours. Atomic steps are visible in the close-up scan (b).

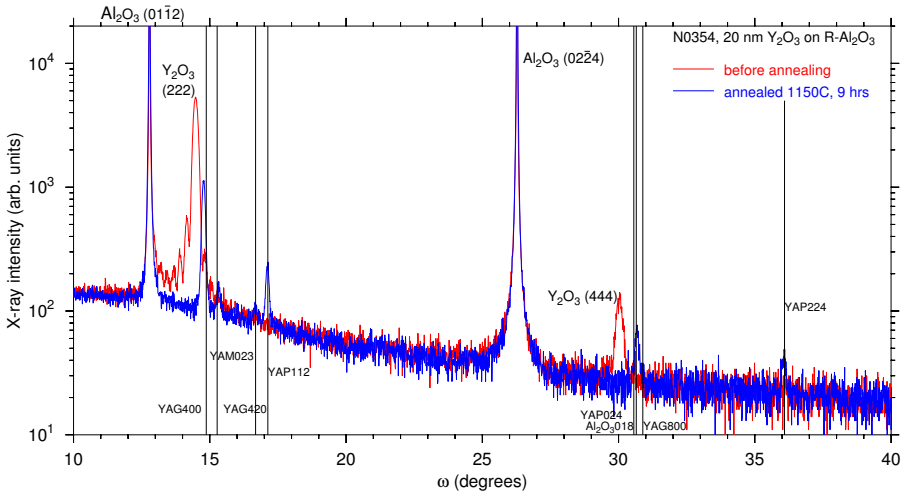

Figure 35: ω–2θ x-ray diffraction scans from a 20 nm thick Y_2O_3 film grown on annealed R-plane sapphire, before and after annealing at 1150 °C for nine hours. Vertical black lines indicate expected positions of x-ray peaks from the literature. The tall clipped peaks are from the substrate, and the other prominent peaks in the "before" spectrum are Y_2O_3 {111}.

There was no difference between the 1300 °C scan and the 1400 °C scan (not shown), but there was a problem with the oven during this final stage, and the temperature setpoint may not have been reached. A difference was present in AFM measurements, as seen in figure 39b, so there is ambiguity regarding this final anneal step.

Since the x-ray diffraction peaks from the film are mostly gone after the final anneal, it is logical to ask whether or not the film still remains on the sample in any form or whether it has evaporated entirely. By visually inspecting the sample, we can see that "shadows" left by the substrate hold-down wires during the deposition process are still present. The complicated structure in the AFM image in figure 39b is also not very suggestive of only the substrate's being left behind. It is possible that the crystal structure of the film has changed such that it has become polycrystalline with random alignment of the individual crystal grains. If this has occurred, one would still expect to see x-ray diffraction peaks as in a powder x-ray scan, but the intensities could be diminished to such a degree that they are not discernible in the measurements we performed.

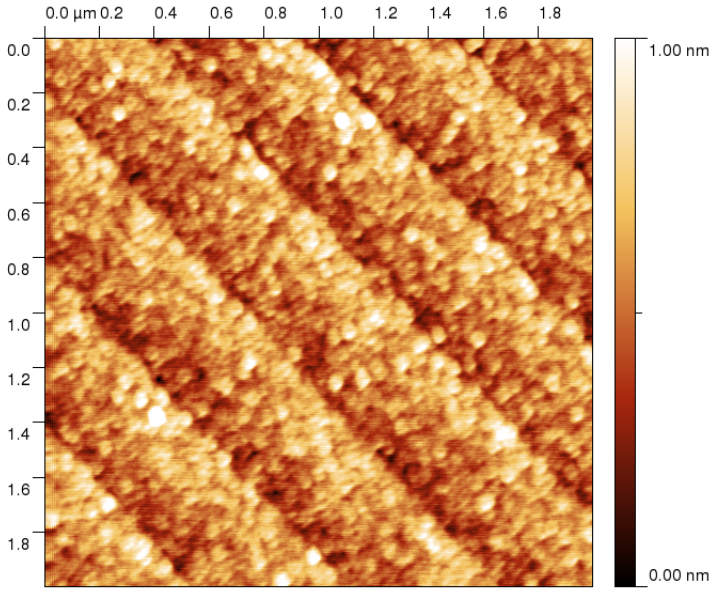

(a) Before

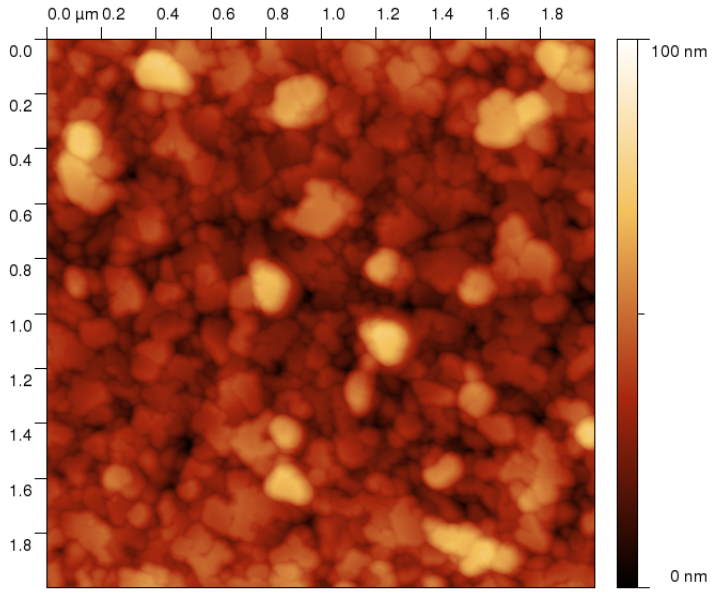

(b) 800 °C

Figure 36: AFM scans of a 66 nm thick Y_2O_3 film (a) before annealing and (b) after annealing for four hours at 800 °C. The atomic steps are replaced by a more granular surface structure after annealing.

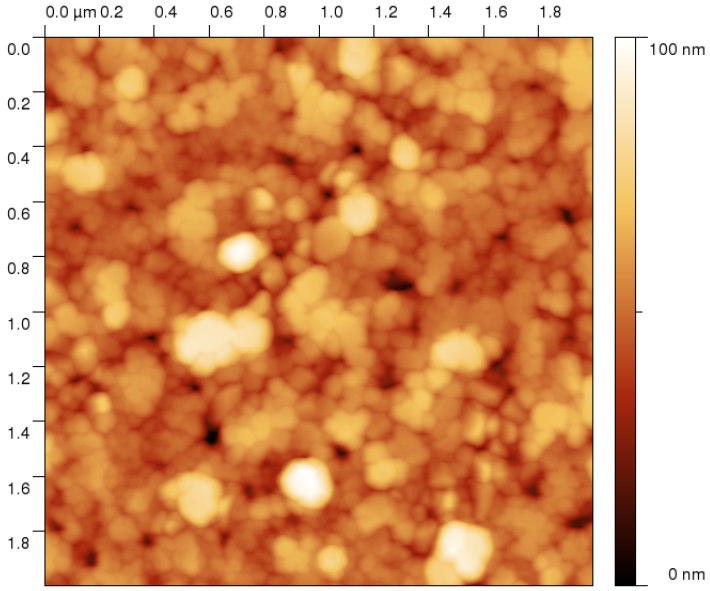

(a) 900 °C

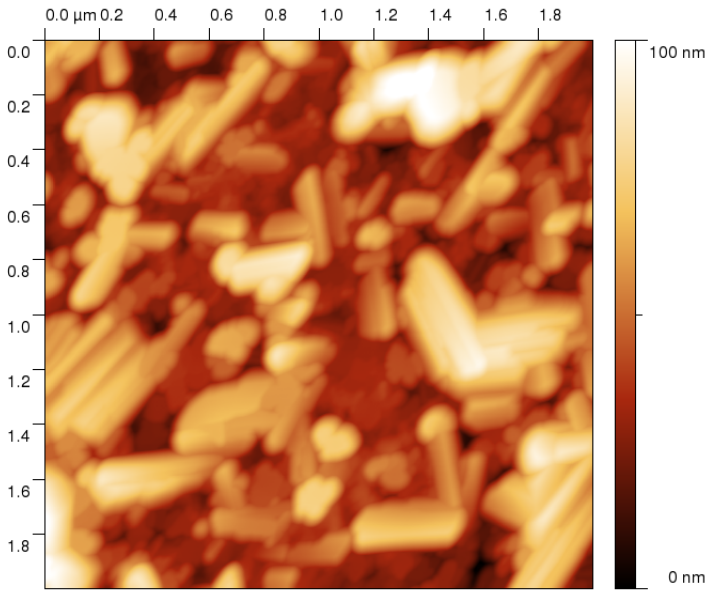

(b) 1000 °C

Figure 37: AFM scans of a 66 nm thick Y_2O_3 film after annealing for an additional four hours at (a) 900 °C and (b) 1000 °C. The surface features have become larger and have more distinct angular structures after the 1000 °C anneal.

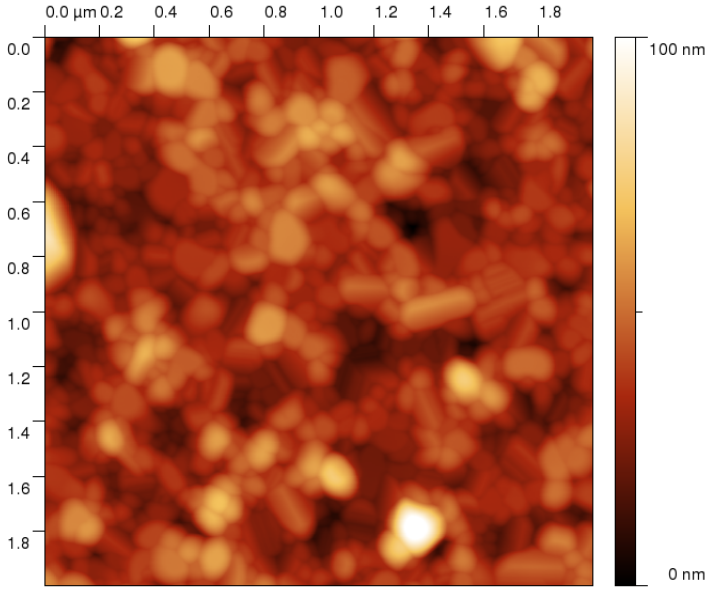

(a) 1100 °C

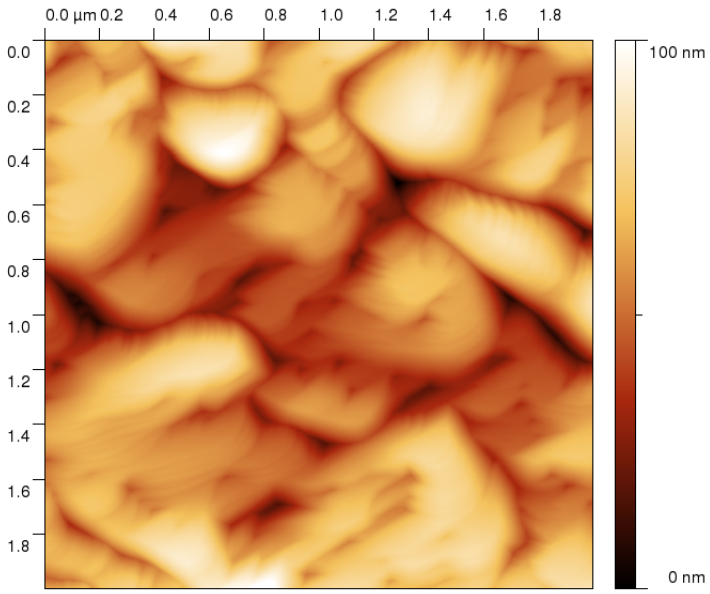

(b) 1200 °C

Figure 38: AFM scans of a 66 nm thick Y_2O_3 film after annealing for an additional four hours at (a) 1100 °C and (b) 1200 °C. The angular structures in figure 37b disappeared after the 1100 °C anneal, but have been replaced with even larger features subsequent to the 1200 °C step.

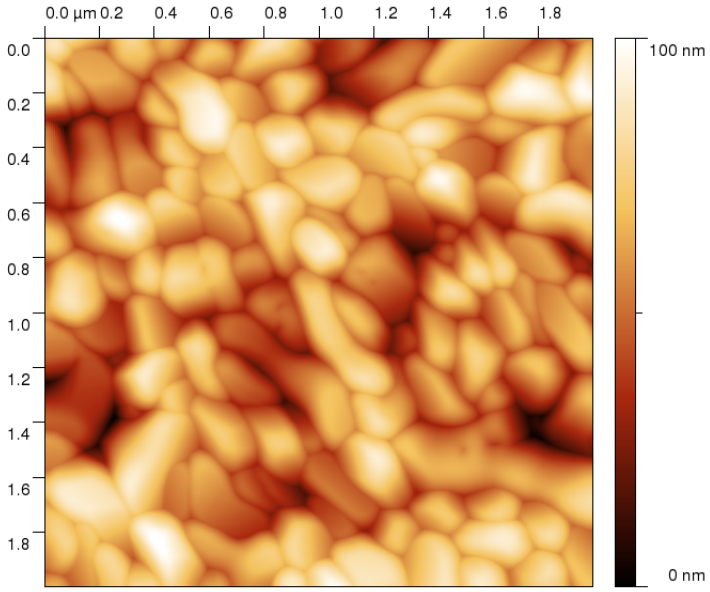

(a) 1300 °C

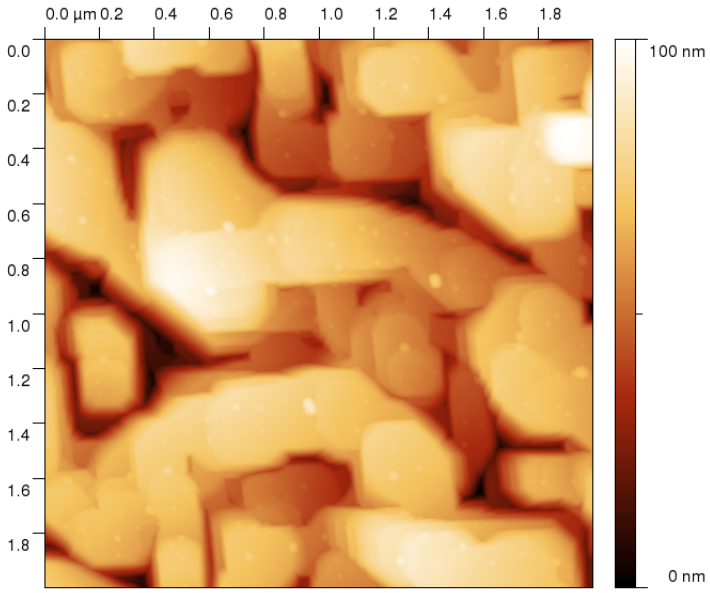

(b) 1400 °C

Figure 39: AFM scans of a 66 nm thick Y_2O_3 film after annealing for an additional four hours at (a) 1300 °C and (b) 1400 °C. After the final 1400 °C anneal the surface is covered with stepped rectangular features.

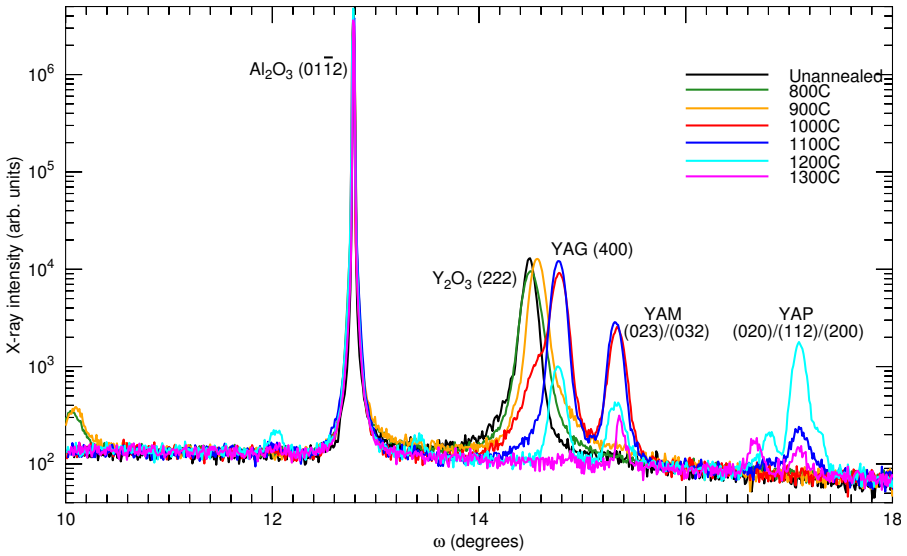

Figure 40: ω–2θ x-ray diffraction scans from a 66 nm thick Y_2O_3 film grown on annealed R-plane sapphire. The same film was annealed several times for four hours at each of the indicated temperatures. The tallest peak is from the substrate. In the unannealed scan only the substrate and Y_2O_3 peak are present. After annealing additional peaks appear, indicating the presence of new crystal phases.

3.3.2.2 *600 nm thick Y_2O_3 film*

A thicker 600 nm Y_2O_3 film doped with around 1% Nd was annealed in a similar fashion to the 66 nm film, except this time the four hour anneals in 100 °C steps started at 600 °C. Figures 41–44 show AFM image results for each step starting at 800 °C, where changes were first noticeable. No noticeable change was seen in the 1400 °C step (not shown) unlike in the thinner film, though, as mentioned above, there was a technical problem with the furnace during this final step. Initial triangular mounds likely related to the triangular {111} symmetry coalesce and form higher-amplitude blobs with some voids visible in the final image. RMS surface roughness wanders about through the series but seems to finally trend upwards, reaching 20 nm after the final anneal.

Figure 45 shows the x-ray diffraction spectra from this thicker 600 nm film. Changes were first detected after the 1000 °C anneal step. The Y_2O_3 (222) peak at 14.5° is joined by another peak around 14.8°. An additional new peak appears at around 15.3°. Looking again at the data in figure 40 it seems likely that the "shoulder" discussed above in the 66 nm thick film scans is in fact the Y_2O_3 (222) peak fading away

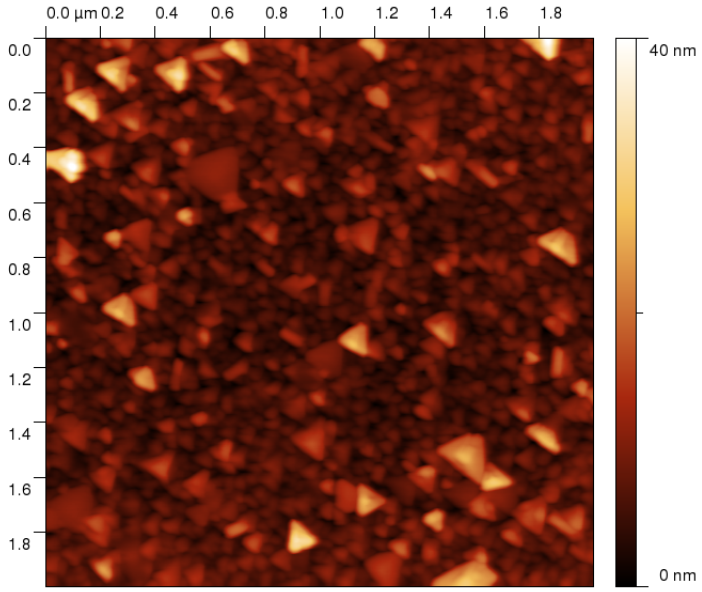

(a) Before

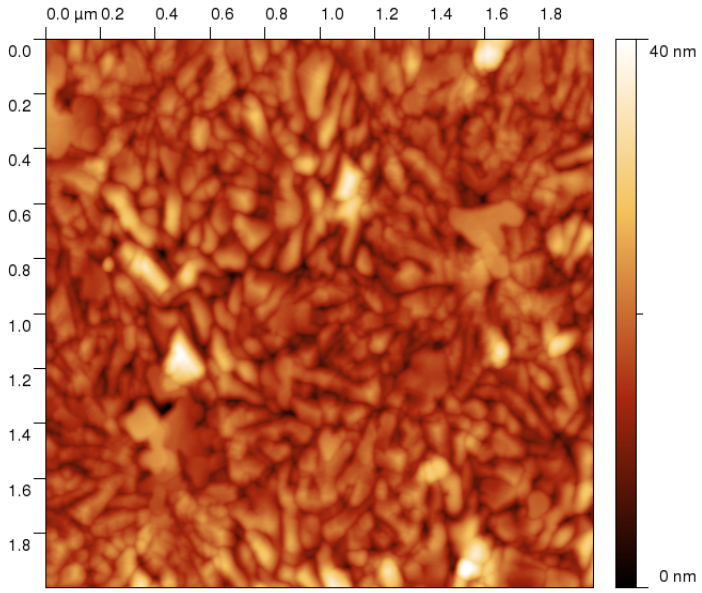

(b) 800 °C

Figure 41: AFM scans of a 600 nm thick Nd:Y_2O_3 film (a) before annealing and (b) after annealing for four hours at 800 °C. The RMS roughness in both cases was 4 nm. Surface features appear to have coalesced after the anneal.

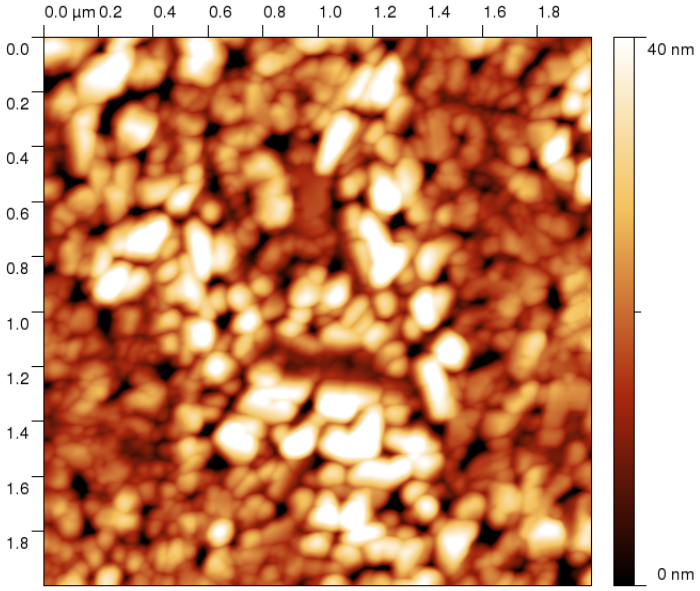

(a) 900 °C

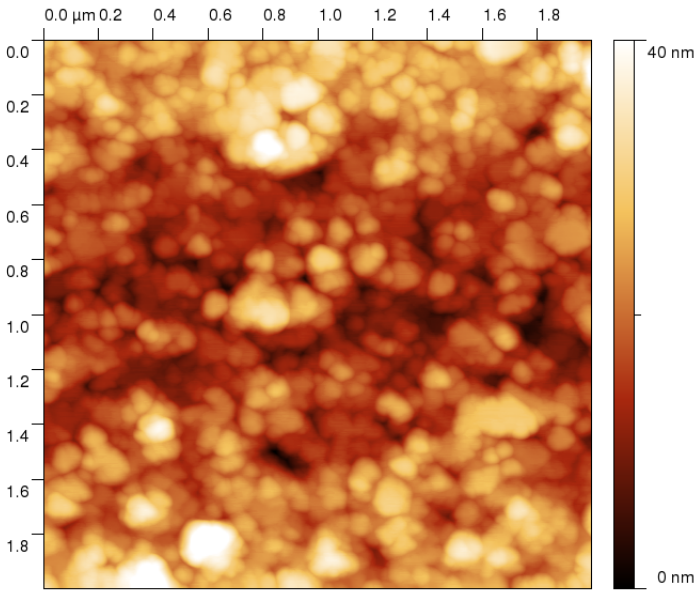

(b) 1000 °C

Figure 42: AFM scans of a 600 nm thick Nd:Y_2O_3 film after annealing for an additional four hours at (a) 900 °C (RMS roughness 10 nm) and (b) 1000 °C (RMS roughness 7 nm). The surfaces appear to be less interconnected than in figure 41b.

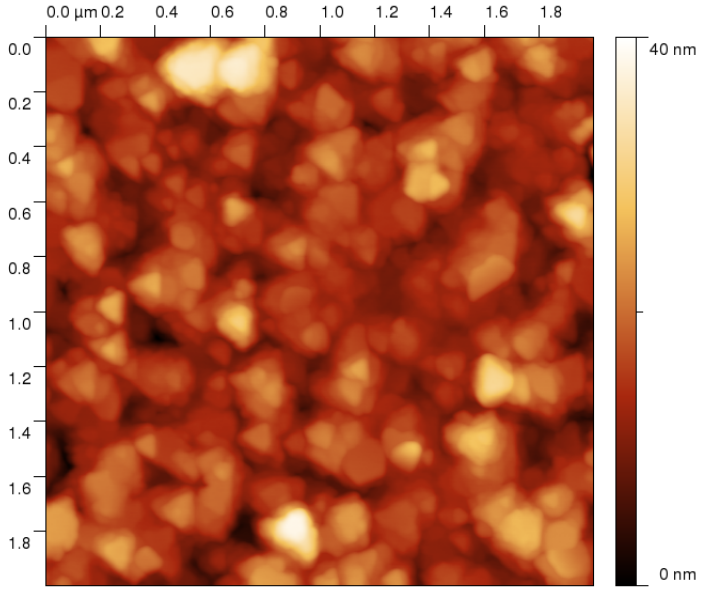

(a) 1100 °C

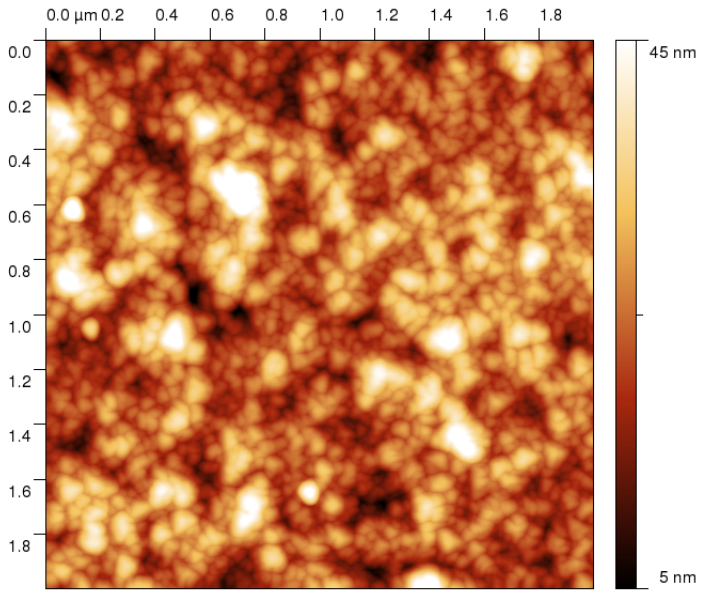

(b) 1200 °C

Figure 43: AFM scans of a 600 nm thick Nd:Y_2O_3 film after annealing for an additional four hours at (a) 1100 °C (RMS roughness 5 nm) and (b) 1200 °C (RMS roughness 7 nm). A definitive trend in the evolution of the surface morphology with annealing is not clear from these images.

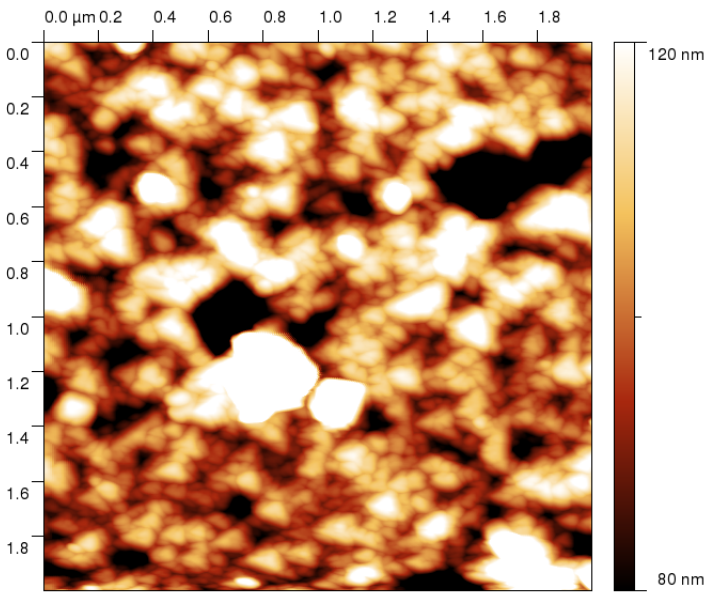

Figure 44: AFM scan of a 600 nm thick Nd:Y_2O_3 film after annealing for an additional four hours at 1300 °C (RMS roughness 20 nm). This image from after the final anneal step shows some larger voids or deep pits on the surface.

and that the peak at 14.8° is new, and not a higher angle version of the Y_2O_3 peak. This would also apply to the results from the initial trial annealing experiment, where it now seems likely that the Y_2O_3 (222) peak was eliminated by the anneal at 1150 °C for nine hours. This thicker sample also shows higher-angle peaks around 17° seen in the previous samples.

It is difficult to positively identify x-ray diffraction peaks like these from data tables because of the many different possibilities, but a cursory inspection of strong peaks from standard powder diffraction data may provide some insight. The Inorganic Crystal Structure Database maintained by the FIZ Karlsruhe Leibniz Institute for Information Infrastructure[92] was consulted, and peaks with strengths $> 20\%$ of the maximum were considered. The YAG, $Y_3Al_5O_{12}$, (400) peak is located at 14.87° and could be the origin of the peak near 14.8°. Another possibility for this peak is the unusual garnet phase of $YAlO_3$, which has a peak at 14.73°.[93] YAM, $Y_4Al_2O_9$, has two peaks near 15.3°: (023) at 15.27° and (032) at 15.28°. The YAM ($22\bar{1}$) peak is at 14.66°, which is very near the Y_2O_3 (222) peak and could be contributing to some confusion. YAP, the more common perovskite phase of $YAlO_3$, has three strong peaks near 17°: (020) at 16.81°, (112) at 17.13°, and (200)

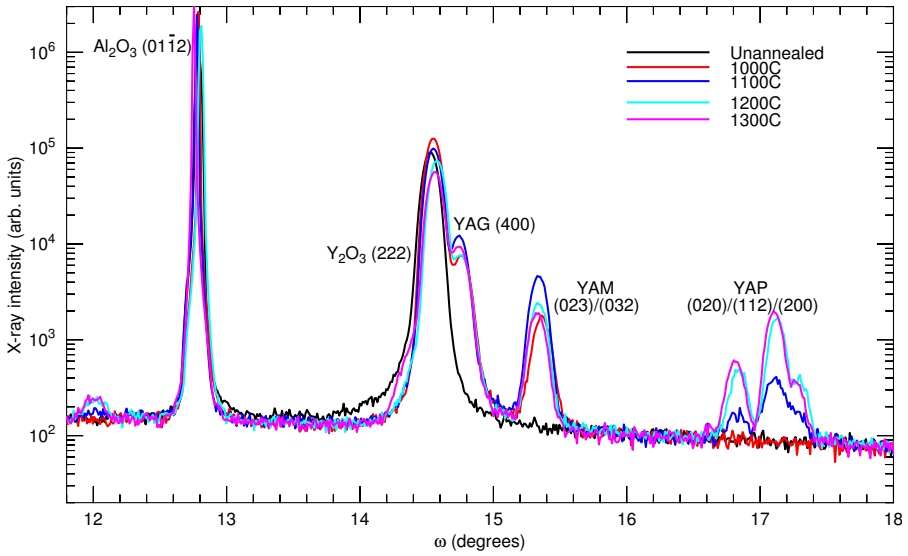

Figure 45: ω–2θ x-ray diffraction scans from a 600 nm thick Nd:Y_2O_3 film grown on annealed R-plane sapphire. The same film was annealed several times for four hours at each of the indicated temperatures. The tallest peak is from the substrate. As in figure 40, the only peaks present before annealing were from the substrate and Y_2O_3 film. New peaks from other crystal phases appear after annealing and persist throughout the process.

at 17.31°. Despite some imperfect position matches, this peak data provides some additional evidence for the yttria film transformations into mixed Y-Al oxide phases.

A prism-coupling laser system was used to investigate waveguiding in the thick sample.[71] Two guided modes were supported for 523 nm light, allowing us to separate the effects of index and thickness changes. We determined that the thickness stayed constant during the anneal and the index dropped from about 1.93 before any annealing to 1.91 after the final annealing step, a significant decrease. The thickness might be expected to increase as Al diffuses into the film from the substrate, but if the initial film was slightly porous, the porosity could be declining during annealing. YAG has a lower index than Y_2O_3, while the index of YAP is higher. There is little data for YAM. This may not lead to an easy conclusion for the expected change of the index, but in general the addition of oxygen could be expected to decrease the index if the film was previously oxygen deficient, by making it less metallic.

Figure 46 shows room-temperature photoluminescence spectra collected from the 600 nm thick Nd:Y_2O_3 sample throughout the anneal-

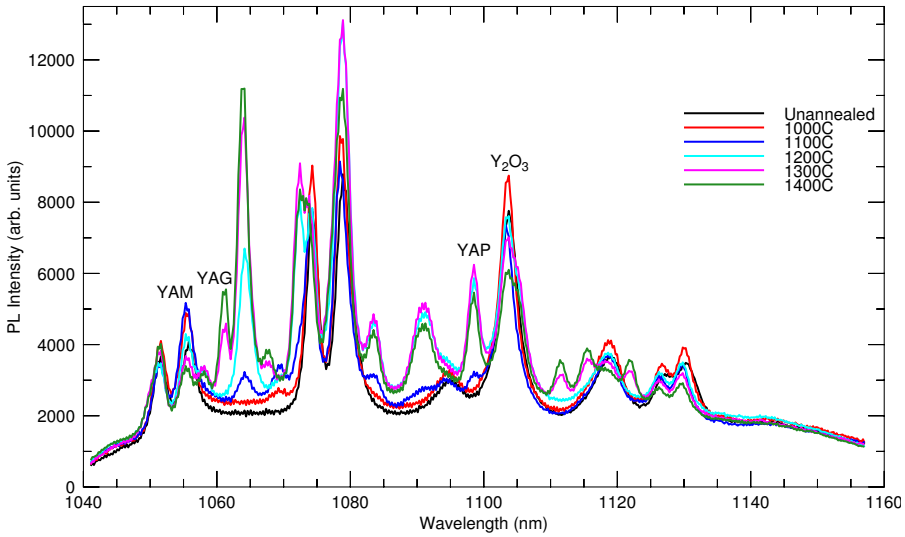

Figure 46: Photoluminescence measurements from a 600 nm thick Nd:Y_2O_3 film grown on annealed R-plane sapphire. The same film was annealed several times for four hours at each of the indicated temperatures. The peaks are due to excited states of the neodymium. The changes in the spectra are due to changes in the crystal host. Sharp spectra indicate crystalline material. The labelled peaks were used to estimate the phase fractions shown in figure 48.

ing process. The pump source was an 800 nm laser diode operated at a power of 500 mW. There was no visible difference until the 1000 °C anneal step, as in the x-ray diffraction measurements. The initial spectra corresponded to typical Nd:Y_2O_3 spectra seen in literature.[94] After the 1000 °C step some small changes are seen in intensity; however, it is difficult to precisely control intensity variation from run to run in the photoluminescence measurement setup, so these changes may not be real. After the 1100 °C step new peaks begin to appear, which become stronger after subsequent annealing steps.

For comparison with figure 46, figure 47 shows photoluminescence spectra from a variety of other Y-Al oxide phases. By noticing the presence of unique peaks from the various phases, we can gain insight into what transformations the Y_2O_3 film may be undergoing during the annealing process. It appears from the lack of peaks at 1096 nm and 1136 nm that no significant amount of Nd:Al_2O_3 is present. There may be a small amount of YAM present due to the increase of peak height at 1055 nm, but this drops down at higher temperatures. YAP peaks, *e.g.* at 1057, 1064, 1072, 1090, and 1098 nm, appear around the 1100 °C anneal step and remain throughout the process. YAG peaks,

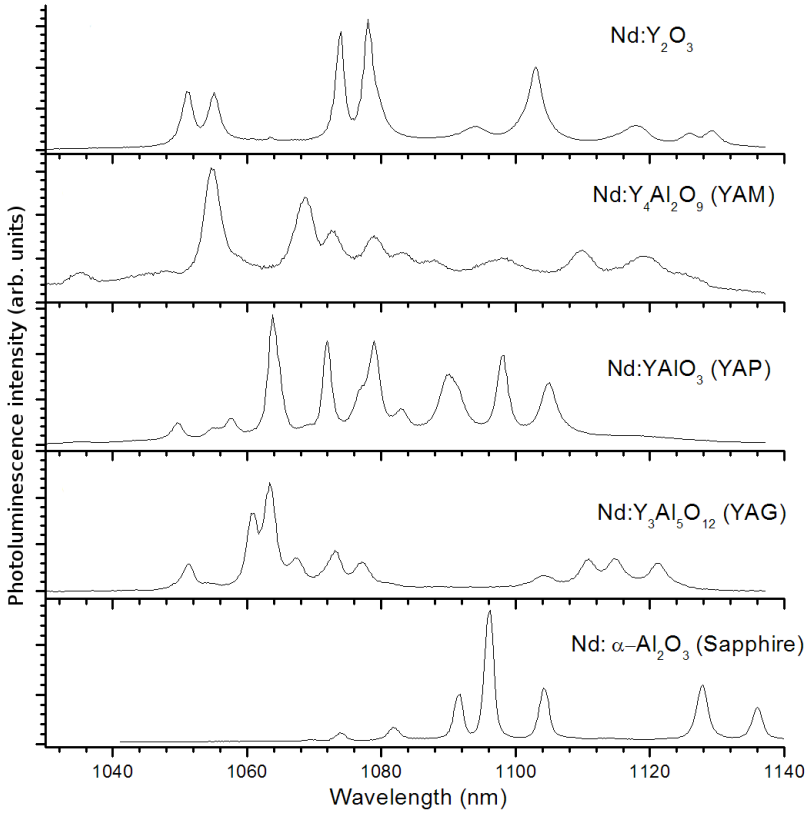

Figure 47: Photoluminescence spectra from Nd:Y_2O_3, Nd:Al_2O_3, and the three Y-Al ternary phases, YAM, YAP, and YAG. The different spectra arise from the different structures of the host crystal lattices surrounding the Nd^{3+} ions. Figure courtesy Raveen Kumaran.

e.g. at 1061 nm, and a group near 1115 nm, appear after the 1300 °C step and remain. The Y_2O_3 peaks appear to be decreasing in intensity after the anneals. This would make sense if the finite amount of Y_2O_3 present is being converted into other phases.

By tracking intensity changes of the Y_2O_3 peak at 1103 nm, the YAM peak at 1055 nm, the YAP peak at 1098 nm, and the YAG peak at 1061 nm, we can make a rough quantitative estimate of the phase fractions of the Y-Al oxides present in the thick film at the various annealing temperatures. The influence of the overlapping yttria peak was subtracted from the YAM peak heights. Figure 48 shows a plot of the results. This figure is intended as only a guideline, as the absolute intensities of these different lines are not expected to be the same. For each temperature the four characteristic peak heights were taken to

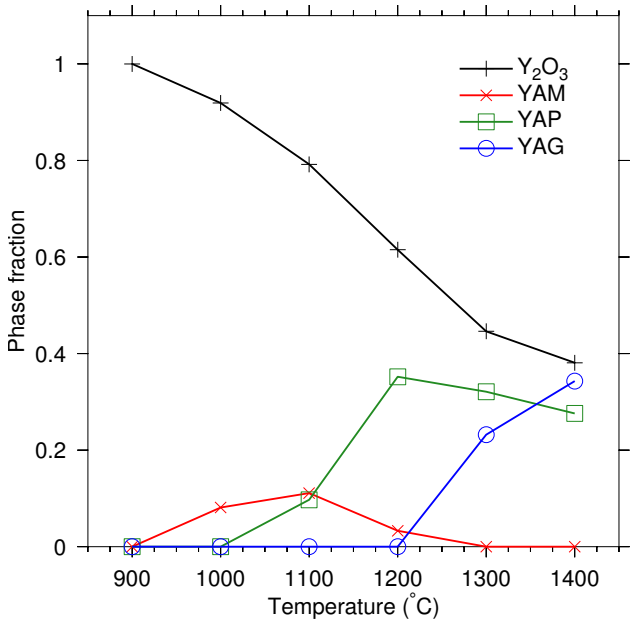

Figure 48: A rough estimate (based on photoluminescence measurements) of the fractions of the various Y-Al phases present in a thick Nd:Y_2O_3 film after annealing at various temperatures.

sum to 100%, and the phase fractions were determined by comparing the height of their unique peak with the 100% sum.

As seen in figure 48, YAM starts to appear after the 1000 °C step, YAP at 1100 °C, and YAG at 1300 °C. However, in the x-ray diffraction data in figure 45, YAG and YAM seemed to form at 1000 °C and YAP at 1100 °C. The inconsistency in the YAG formation temperature may mean that the YAG peak has been misidentified in the x-ray spectrum or that it takes extra time for the Nd atoms to integrate into the YAG structure and start producing photoluminescence.

3.3.3 *Discussion of interdiffusion*

It is logical for YAM and YAP to appear first when annealing Y_2O_3 on Al_2O_3, since they have high yttrium-to-aluminum ratios of 2:1 for YAM and 1:1 for YAP. As aluminum diffuses from the substrate into the Y_2O_3 film, these lower Al fraction compounds would be likely to form first. YAG, with its 3:5 Y:Al ratio forms later, as more Al diffuses into the film. As this occurs, the amount of Y_2O_3 decreases. Figure 49 shows a schematic diagram of how the some of the stages of annealing could progress.

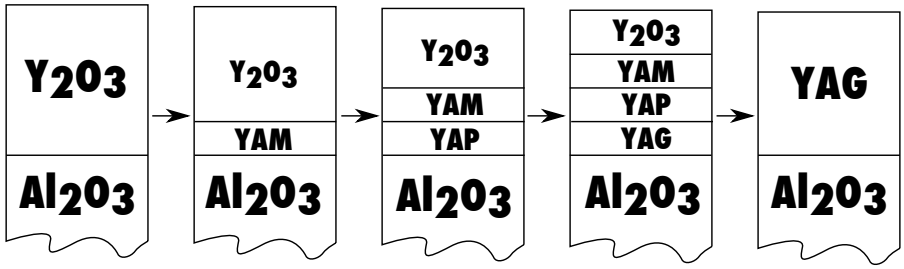

Figure 49: Schematic of some possible steps in the annealing process of Y_2O_3 on Al_2O_3. First, YAM, the mixed Y-Al oxide with the highest Y:Al ratio appears, followed by YAP and YAG. As this happens, the amount of Y_2O_3 decreases. Eventually all that would be left is some amount of YAG, the most stable of these ternary oxides.

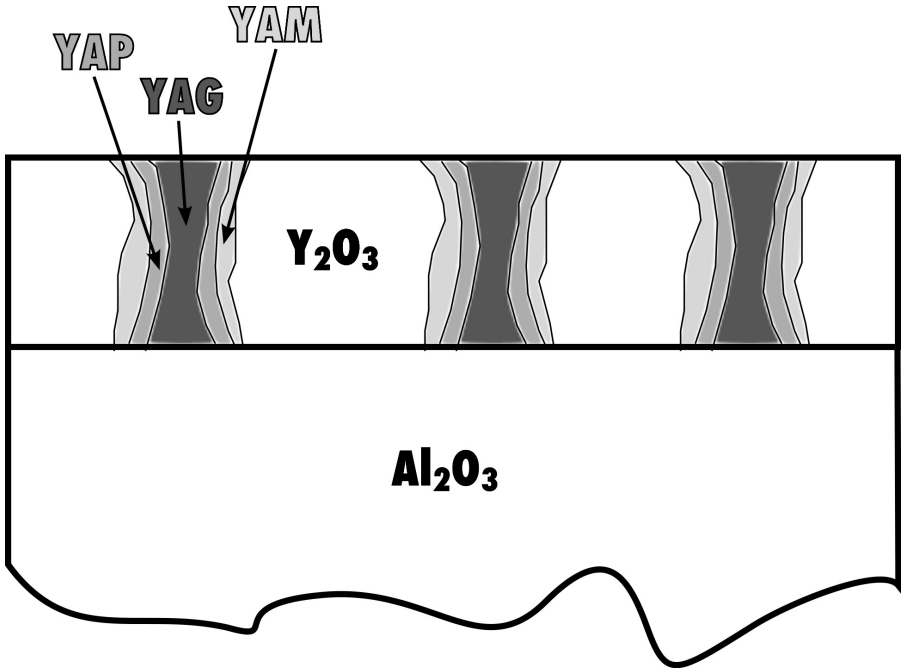

Figure 50: An alternate schematic view of how the annealing process of Y_2O_3 on Al_2O_3 could proceed. Aluminum could propagate up "channels" that surround Y_2O_3 crystallites.

We can attempt to obtain quantitative information about the diffusion that is occurring by analyzing the x-ray and AFM results above. First we assume that only Al diffuses into the Y_2O_3 and not Y into the Al_2O_3 substrate. This could be a reasonable assumption, since Y is a larger atom than Al. Nd is also much larger than Al and was not observed to diffuse into the Al_2O_3 in photoluminescence measurements. Porosity in the films is another potential rationale for increased diffusion compared to the substrate. From Fick's laws of diffusion, after time t, at temperature T, Al will diffuse a distance approximately $\sqrt{Dt}$ into the Y_2O_3 film, where D, the diffusion constant is given by

$$D = D_0 e^{-E_a/k_b T}, \tag{3.2}$$

with D_0 being an infinite-temperature diffusion constant, E_a the activation energy for the diffusion, and k_b the Boltzmann constant.

As diffusion occurs, Y_2O_3 is converted into the Y-Al oxide phases YAM, YAP, and YAG. The x-ray diffraction peaks from these phases increase and decrease in height in proportion to the amount of each phase present. The Y_2O_3 x-ray peak decreases in intensity as material is converted to the other phases. This is most obvious in figure 40. Here we see that the Y_2O_3 (222) peak at approximately 14.5° has diminished to about 15% of its original intensity after the 1000 °C annealing step. We interpret this to mean that Al has diffused through 85% of the film in the four-hour annealing time. This allows us to calculate a diffusion constant by equating 85% of the 66 nm film thickness (*i.e.* 56 nm) to a diffusion length, $\sqrt{Dt}$, and then solving for D. We arrive at a value of $D_{1000\,^\circ C} = 2.2 \times 10^{-15}\,\mathrm{cm}^2/\mathrm{s}$.

We can proceed further and extract an activation energy using equation 3.2 by estimating a value for D_0 as follows. We assume that the infinite-temperature diffusion constant, D_0, is approximately equal to the mean free path of the atoms, l_{MFP}, multiplied by the average velocity of the atoms, $\bar{v}$. We can estimate the average velocity as the product of the mean free path and a thermal attempt frequency, ν_0, similar to the Debye frequency, which we take to be about $10^{12}\,\mathrm{s}^{-1}$.[95] We can further estimate the mean free path to be equal to the ionic diameter of the oxygens ($r_{ion} \approx 0.14$ nm), assuming that they are the primary impediment to diffusion. So we have:

$$D_0 \approx l_{MFP}\bar{v} \approx l_{MFP}^2 \nu_0 \approx 4 r_{ion}^2 \nu_0 = 7.8 \times 10^{-4}\,\mathrm{cm}^2/\mathrm{s}. \tag{3.3}$$

Using the above values for D and D_0 we find an activation energy for Al diffusion in Y_2O_3 of 3.0 eV. We compare our results with litera-

	Al in Y_2O_3 (this work)	Y in Al_2O_3	Y in Y_2O_3	Al in Al_2O_3
$D_{1000\,°C}$ (cm^2/s)	2.2×10^{-15}	9.3×10^{-19}	1.6×10^{-17}	2.3×10^{-22}
$\log_{10} D_{1000\,°C}$ (cm^2/s)	−14.7	−18.0	−16.8	−21.7
$\log_{10} D_{1200\,°C}$ (cm^2/s)	−13.1	−16.4	−15.1	−18.8
$\log_{10} D_0$ (cm^2/s)	−3.1	−5.9	−4.5	−0.66
E_a (eV)	3.0	3.1	3.1	5.3

Table 3: Diffusion constants and activation energies for Al and Y diffusing in Y_2O_3 and Al_2O_3. Y in Al_2O_3 data from E.G. Moya *et al.*,[96] Y in Y_2O_3 data from R.J. Gaboriaud,[97] and Al in Al_2O_3 from M. Legall *et al.*[98]

ture values for Y diffusion in single-crystal sapphire,[96] Y diffusion in single-crystal Y_2O_3,[97] and Al diffusion in single-crystal sapphire[98] in table 3. Our activation energy is very similar to the values for Y diffusion in Al_2O_3 and Y_2O_3. Our calculated diffusion constant for Al is higher than the reported value for Y in Al_2O_3, which is consistent with our assumptions. It is impractical to calculate meaningful error estimates from our limited data.

3.3.4 *Effect of annealing on surface roughness*

We can attempt to learn about surface diffusion, in contrast with bulk diffusion discussed above, by studying the AFM results. Power spectral density (PSD) curves were calculated for each of the AFM images captured from the two films that were annealed in stages (figures 36-39 and 41-44). Figure 51a shows example PSD measurements from the 600 nm thick Nd:Y_2O_3 sample after annealing at 800 and 1300 °C. The PSD gives a measure of which length scales are present on the sample surface and is equal to the Fourier transform of the autocorrelation of the image in one direction, averaged over the other direction. For our samples the typical result was a flat horizontal line at low spatial frequency, which rolled off and dropped linearly on a log-log plot at higher frequency. By fitting straight lines to the low- and high-frequency sections and finding their intersection, we can determine a characteristic spatial frequency and therefore a characteristic length, the inverse, for the surface. This procedure is illustrated in figure 51a. Two PSD data sets are shown, with characteristic spatial frequencies of $3 \times 10^6\,m^{-1}$ and $1 \times 10^7\,m^{-1}$, giving lengths around 300 nm and 100 nm, respectively. While the dynamic range of the presented data somewhat exceeds that of the AFM, owing to the finite size of the

imaged area and pixels, the highest- and lowest-spatial-frequency points can be ignored with minimal impact on the calculation of our characteristic length.

Now, similarly to above, we can assume that this length is proportional to the diffusion length and therefore the square root of the diffusion constant. With data from the anneals at various temperatures in figure 51b we extract an activation energy using equation 3.2. For our Y_2O_3 films we find an activation energy for surface diffusion of (0.5 ± 0.3) eV. This is somewhat less, but not incredibly so, than the value of 1.3 eV reported for surface diffusion of single crystal Al_2O_3[99] and lower than the 3.6 eV reported for surface diffusion in polycrystalline Y_2O_3.[100] Our value of 0.5 eV will be discussed further in section 4.1.

3.4 SUMMARY

Post-growth annealing of Y_2O_3 oxide films grown on sapphire tends to roughen the surface and convert the Y_2O_3 to other mixed Y-Al phases including YAM, YAP and YAG. This is not directly helpful for the creation of waveguide laser devices, but the ability to convert material between these phases could be useful if a single phase end result was possible. The diffusion constants estimated for Al migration in Y_2O_3 and for Y_2O_3 surface diffusion are useful for comparison with other materials systems.

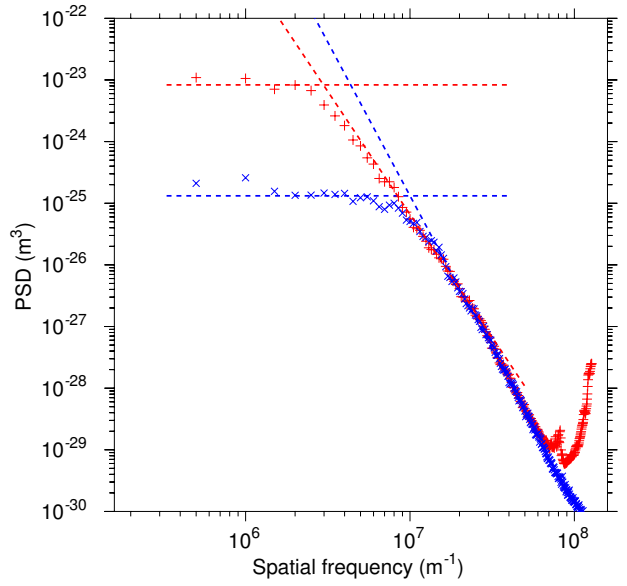

(a)

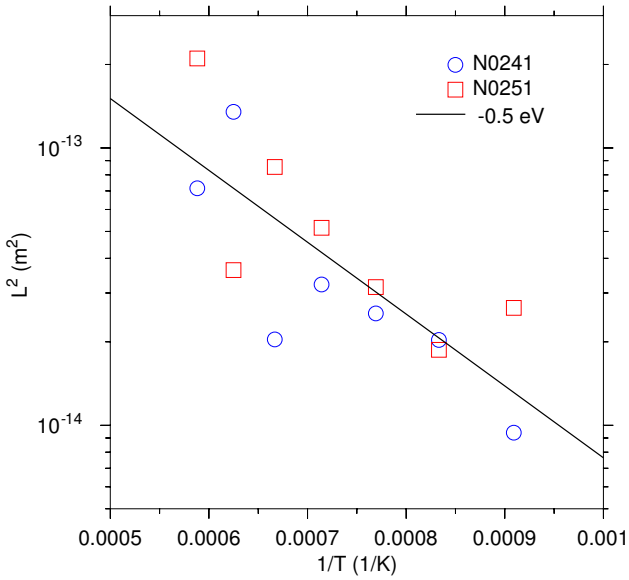

(b)

Figure 51: (a) Power spectral density data from the surface of a thick Nd:Y_2O_3 film after annealing for four hours at 800 °C (blue) and 1300 °C (red). The intersection of the dashed trend lines is taken as an inverse characteristic length of the surface. (b) Characteristic lengths, L, determined from PSD data, were plotted as a function of temperature to determine an activation energy for surface diffusion. The blue circles are from the 600 nm film and the red squares are from the 66 nm film. The black line is a fit to the data representing a 0.5 eV activation energy. The square of the characteristic length is plotted on the vertical axis because the diffusion constant is proportional to the square of the diffusion length. By plotting the data in this fashion the exponential activation energy in equation 3.2 appears as a straight line.

4 X-ray structural analysis

X-ray diffraction is a powerful characterization tool that can be used to provide detailed information about the structural properties of crystalline films. Typically one performs an experimental measurement and then compares with theory to interpret the data. A simple example would be to use the diffraction angle of an x-ray peak with respect to the film surface to calculate the lattice spacing of the crystal. In this chapter we explore the results from x-ray diffraction experiments and calculations as they apply to thin oxide films.

4.1 Critical thickness

A series of relatively thin Y_2O_3 films, 5 to 70 nm thick, were grown to investigate the initial stages of growth. Understanding the beginning of the growth process may allow us to better control the growth of thicker films that are suitable for waveguide structures. Our analysis revealed that the thin films started growing with a very high degree of structural order, but that eventually the growth mode changed such that the film was more disordered. This type of growth suggests a "critical thickness" phenomenon, where the film structure drastically changes at a certain thickness.

R-plane sapphire substrates that had been annealed in air for nine hours at 1150 °C were used as substrates. Annealing the substrates causes distinct atomic steps to form on the surface, leading to improved structural quality and lower surface roughness for the films (see sections 2.1 and 3.2). During film growth the substrates were heated to between 400 and 1000 °C. The yttrium effusion cell was operated between approximately 1400 and 1800 °C, allowing control of the growth rate between 10 and 240 nm/hr. The yttrium beam equivalent pressure was measured with an ion gauge, calibrated for N_2, placed in front of the substrate, and found to be between 1×10^{-8} torr and 3×10^{-7} torr. Oxygen gas was introduced to the growth chamber through the plasma source but the source was not energized. Typical oxygen background pressures were 3×10^{-6} torr, giving an oxygen-to-yttrium flux ratio of between approximately 10:1 and 300:1.

Figure 52 shows a typical streaky RHEED pattern observed during growth, indicating good crystalline quality and a smooth film. These

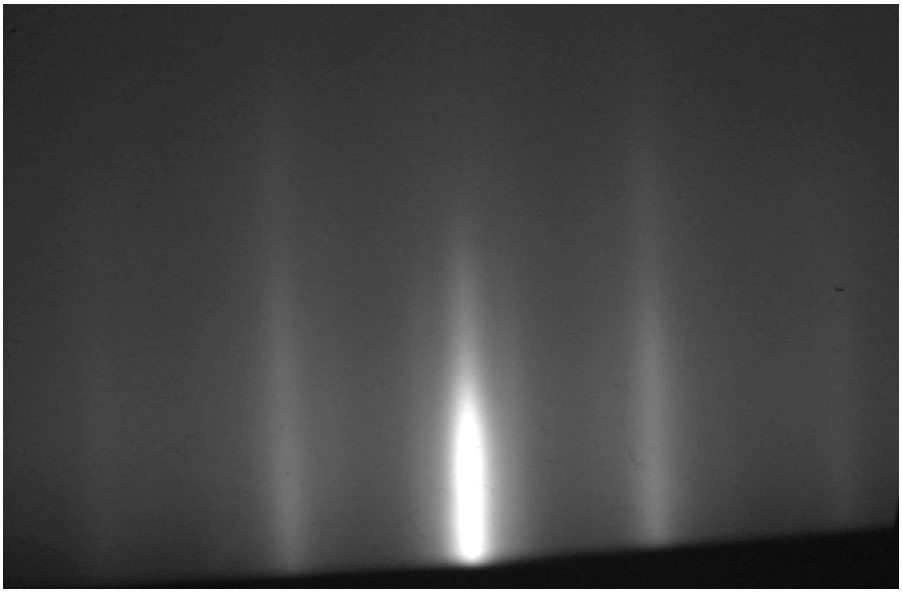

Figure 52: RHEED image from Y_2O_3 growing on R-plane sapphire. The beam is oriented along the Y_2O_3 [$1\bar{1}0$] direction. The streaks indicate a smooth surface. Sharper spots can appear when the electron beam is transmitted through material on rougher films. The horizontal spacing between the streaks corresponds to the inverse of the in-plane lattice spacing of the crystal.

patterns persisted throughout the growth. RHEED provides a measure of the in-plane orientation of the film with respect to the substrate. By loading the substrate in a known orientation and analyzing the streak spacing in the substrate RHEED pattern before growth, we determined that the beam was oriented along the Al_2O_3 [$2\bar{1}\bar{1}0$] direction. Analysis of the film streak spacing after growth, combined with x-ray diffraction data, showed that the corresponding direction in the Y_2O_3 crystal was [$1\bar{1}0$]. Growth oscillations were not observed in the RHEED measurements.

Figure 53 shows x-ray reflectivity from the same sample as in figure 52. By fitting the oscillations in the x-ray reflectivity with a model using the PANalytical X'Pert Reflectivity software,[101, 102] we determined that the film was 21 nm thick. This corresponds to a growth rate of 11 nm/hr. We saw no change in growth rate for varying substrate temperatures. This is an indication that all of the yttrium sticks to the substrate and does not re-evaporate. The critical angle found in the reflectivity fit confirms that the film had the expected density of 5.01 g/cm^3, as for bulk Y_2O_3. X-ray reflectivity also pro-

vides a measure of film and interface roughness. For this sample the substrate/film interface and surface roughness were 0.6 and 0.7 nm, respectively, from reflectivity, and the RMS surface roughness was 0.2 nm from AFM. The reflectivity values are based on a density-change interface width and could reflect deeper structures than the AFM can image.

The right side of figure 54 shows an AFM image of the sample discussed above, with atomic steps clearly visible. The left side of figure 54 shows a typical starting R-Al_2O_3 surface with atomically flat terraces. Since the step edges remained straight during growth, we concluded that the steps were a conformal replication of the steps present on the initial substrate surface and were not an indication of step flow growth. The mottled pattern on the surface with a characteristic feature size of about 20 nm was typical of the Y_2O_3 films. The straight step edges and mottling in excess of the substrate roughness are evidence for low diffusion during growth. Larger adatom diffusion lengths would likely lead to step-edge roughening and increased Y_2O_3 island size.

The inset of figure 53 shows the dependence of the AFM measured roughness on film thickness for a variety of Y_2O_3 samples with thicknesses from 6 to 1200 nm, including films grown in this study and those mentioned in chapter 3. For a random deposition process with no diffusion, the expected relationship is:

$$w \sim t^{0.5}, \tag{4.1}$$

where w is the RMS roughness and t is the film thickness.[103] This relationship is shown on the log-log plot as a straight line with slope 0.5 and is consistent with the AFM data. This type of deposition process is also known as ballistic aggregation. While some diffusion is required for epitaxial growth, this is another indication that only short-range surface diffusion occurs. The films represented by the data points were grown under the range of conditions described above, so some deviations are expected and this plot is intended only to indicate a general trend. Additionally, some large crystallites present on the surface of the thicker films were ignored in the roughness determination in an effort to compare only the small-scale local roughness.

Additional structural characterization was performed by x-ray diffraction. Figure 55a shows a portion of an ω–2θ scan for the same 21 nm thick Y_2O_3 film on R-Al_2O_3 as in figure 54. The substrate peak and film peak are shown with clear pendellösung fringes visible for

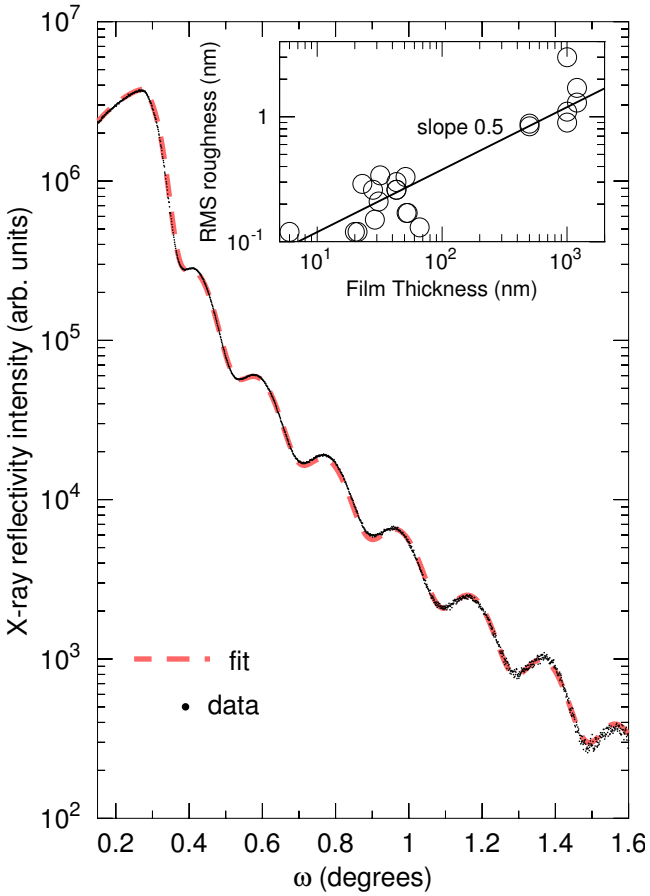

Figure 53: X-ray reflectivity scan from a Y_2O_3 sample. The excellent fit (red dashed line) to the data (black) indicates that the thickness of the film is 21 nm and that it has the bulk Y_2O_3 density of 5.01 g/cm^3. Film and interface layer roughness are also included in the model. Inset: RMS roughness as determined by AFM for Y_2O_3 samples with a variety of thicknesses. The error in the AFM measurements is represented by the data point size.

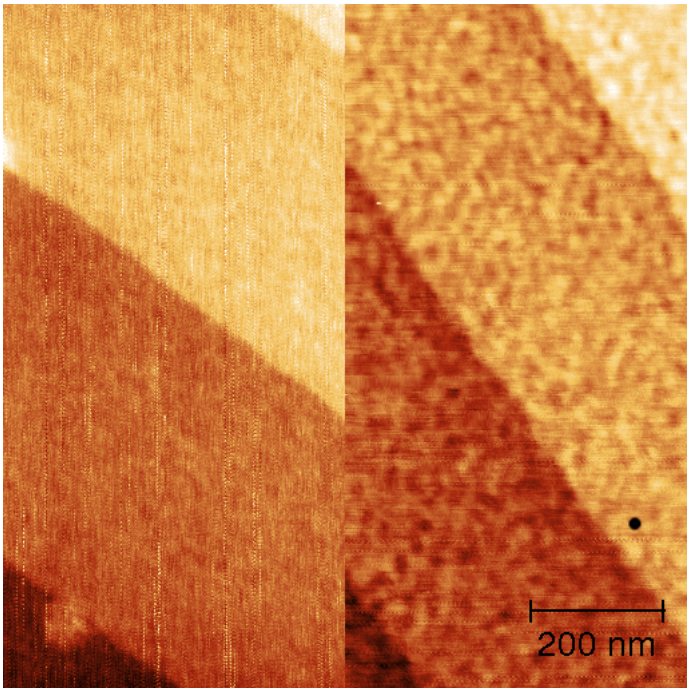

Figure 54: AFM images of a typical annealed R-Al_2O_3 substrate (left) and Y_2O_3 sample (right). Clear atomic steps are visible on the substrate. These steps persist through the growth, with the film developing a clear mottled texture not present on the starting surface. The small black dot in the lower right indicates the average crystallite size of 15 nm determined using equation 4.9, matching the mottled pattern. The step spacing is different in the two images due to varying miscut between wafers. The linear full colour scale is 1.6 nm.

the film, indicating sharp interfaces and a high-quality epitaxial film. The film peak was identified as Y_2O_3 (222), indicating that the film grew with {111} out-of-plane orientation. This was consistent for all growths on sapphire, independent of the substrate orientation. The film peak is relatively broad because the film is quite thin. The peak width matches the minimum width expected for this film thickness estimated using the Scherrer formula:

$$B = \frac{0.9\lambda}{t \cos\theta}, \tag{4.2}$$

where B is the full-width at half-maximum (FWHM) of the x-ray peak, λ is the x-ray wavelength, t is the film thickness or grain size, and θ is the diffraction angle.[73] Only Y_2O_3 {111} and substrate reflections were seen in broader ω–2θ scans.

The region of reciprocal space surrounding the peaks in figure 55a was examined further by collecting an x-ray reciprocal space map with a triple-bounce Ge analyzer crystal. The analyzer crystal is necessary to ensure that only single points in reciprocal space are measured for each data point. The usual slits on the detector actually sample a small arc of reciprocal space, which greatly increases intensity but is inappropriate for creating a space map. The large ω–2θ width of the film peak is visible as the vertical stripe in the map shown in figure 56. Broadening of the film peak in the in-plane direction is visible as a broad horizontal background.

The in-plane film peak broadening was investigated to further quantify the structural quality of the films by recording ω scans for several samples. ω scans consist of rocking the sample while holding the detector fixed. This corresponds to measuring along k_x in reciprocal space. Figure 55b shows results from three films. Two of the films have broad mosaic backgrounds topped by sharp peaks. The thinnest 6 nm film shows only a sharp peak. The sharp peaks are extremely narrow, around 7 arcseconds, when measured with the detector analyzer crystal. This is approximately the resolution of the diffractometer, indicating a high degree of structural order.

The fact that the thinnest film had no broad background suggests that the crystal growth may start out essentially perfectly, with greater disorder occurring with increased thickness. This type of growth often occurs for semiconductors, where the film grows strained to match the lattice constant of the substrate up to a certain point, then relaxes by dislocation nucleation and propagation. The film thickness that can be reached before relaxation is called the critical thickness, and

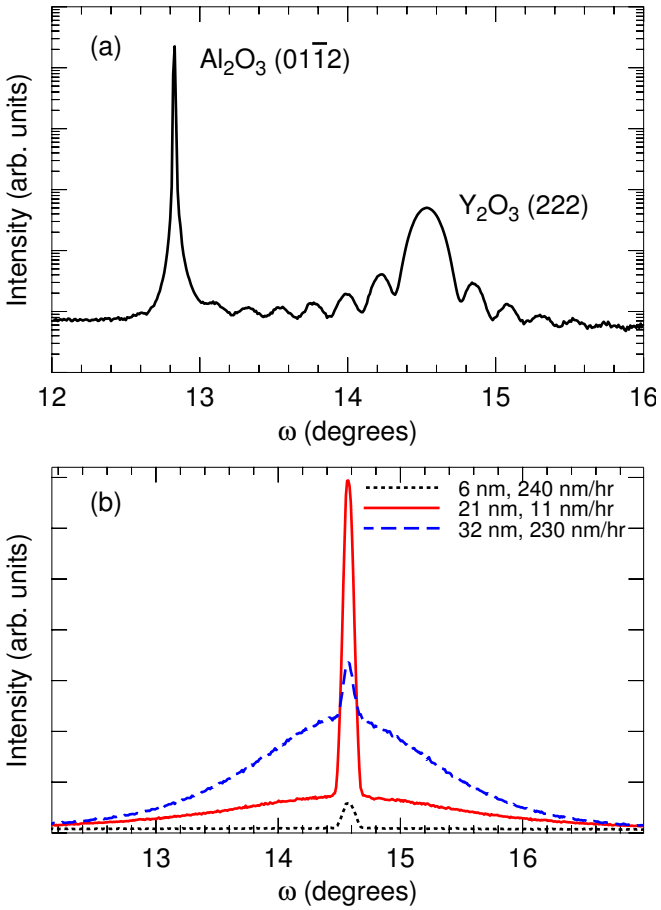

Figure 55: (a) ω–2θ x-ray scan of a 21 nm {111}-oriented Y_2O_3 film on R-Al_2O_3. The fringes indicate sharp interfaces and a high degree of film uniformity. (b) ω x-ray scans of the film peaks from various Y_2O_3 samples (thickness and growth rate are indicated). The sharp central peak is from highly ordered material that grows initially while the broad background is from subsequent lower-structural-order material.

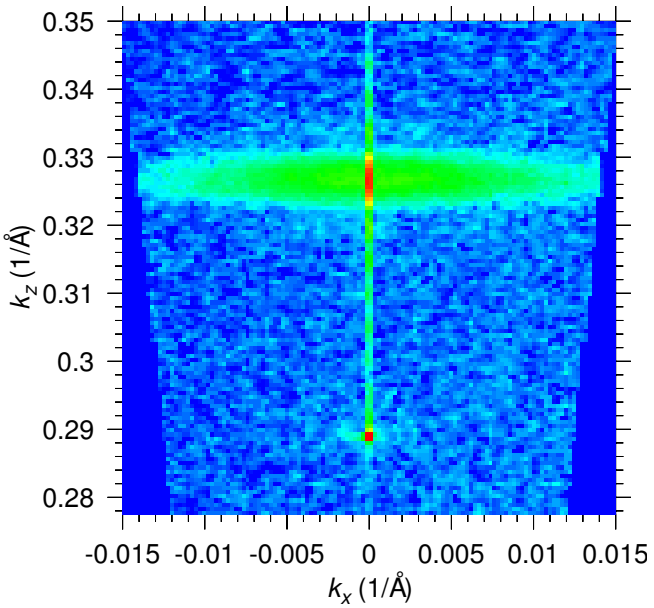

Figure 56: X-ray reciprocal space map from Y_2O_3 on R-Al_2O_3. The peak at the bottom of the image is the substrate peak and the streak in the upper part is the film peak, broadened vertically by its small thickness. The broad horizontal background on the film peak is due to structural imperfections. The abrupt colour changes in the film peak are due to the very sharp features seen in figure 55b. A logarithmic colour scale is used.

is determined by the mismatch between the substrate and film lattice constants. An expression for this critical thickness was derived by Matthews and Blakeslee.[104] Our case of a (111) cubic lattice on the $(01\bar{1}2)$ face of a hexagonal crystal is somewhat complicated, but the mismatch between the best-aligned planes of atoms is approximately 10% along the $[\bar{2}110]Al_2O_3/[1\bar{1}0]Y_2O_3$ direction and about 5% in the perpendicular direction ($[0\bar{1}11]/[11\bar{2}]$). With such a mismatch the expected Matthews-Blakeslee critical thickness would be less than a monolayer. Our measurements, described below, indicate that the volume of highly ordered material in our films is much greater than this minimal amount. Additionally, we do not see a large peak position shift due to strain in our x-ray diffraction results. Therefore we conclude that our layers are not strained to match the substrate, and that a somewhat different process is occurring in our experiments.

To investigate this concept in more depth, we choose to take the ratio of the ω-scan sharp peak area to total ω-scan area as a metric for evaluating film quality. We propose that the sharp peak signal is from highly ordered material while the broad peak signal is due to lower-quality portions of the film. As mentioned above, a simple way to envision the growth is to imagine that the film grows nearly perfectly up to a certain critical thickness, but then the growth changes and lower-quality material is deposited beyond the critical thickness. We can quantify this critical thickness by multiplying the ratio of sharp peak area to total area by the film thickness:

$$t_c = \frac{A_{sharp}}{A_{total}} t, \tag{4.3}$$

where t_c is the critical thickness, A_{sharp} is the area of the sharp peak in the ω scan, A_{total} is the total scan area, and t is the total film thickness. Note that this case would be different from the concept of critical thickness for semiconductors described above. In that case the highly ordered part of the crystal is "destroyed" by dislocations that propagate throughout the full thickness of the film. In our case the "perfect" part of the film appears to remain intact regardless of total film thickness.

Note that equation 4.3 would provide an appropriate quantitative measure of film quality even if all of the highly ordered material was not present in a uniform initial layer. If the high-quality material was distributed throughout the film then we could take the same peak area ratio and multiply it by the film volume to find the fractional volume of ordered material. Since all of our films have the same surface area,

multiplying by the film thickness has the same effect, and equation 4.3 is valid for comparing our samples.

The two-component ω-scan line shape with both sharp and broad components has been seen before by others, though interpretation in the literature varies. Some interpret the lineshape as being due to a traditional critical thickness phenomenon, with initial high quality growth, followed by lower quality relaxed material.[23, 66, 105] One group suggests that the high quality material may be present *on top* of the film, "floating" on a relaxed layer.[106] Zaitsev *et al.* conclude that the highly ordered material is distributed throughout the thickness of the film.[107] They argue that the finite thickness determined from the spacing of pendellösung fringes in ω–2θ scans is the same as the full thickness of the film, and therefore that the ordered material is not restricted to either the top or bottom of the layer. Boulle *et al.* show reciprocal space maps very similar to our figure 56.[108, 109] They state that the sharp feature is due to coherently diffracting crystallites which extend throughout the thickness of the film. The peak can be sharp in the in-plane direction because the lateral extent of the crystallites is greater than the film thickness. They state that while the sharp coherent peak only depends on the size and shape of the crystallites, the broad diffuse peak also depends on disorder and can therefore be wider in the in-plane direction. Boulle also presents simulations that match the experimental data that take into account the shape of the crystallites and the distribution of their sizes in the film.

Several additional groups have attempted to explain these results theoretically. Miceli and Palmstrøm present a scattering model which reproduces the two-component ω-scan lineshape.[110] They attribute the broad peak to rotational displacements within the crystal with short correlation lengths. They state that the sharp peak is due to uncorrelated displacements that are "bounded in magnitude by the substrate." The idea is that the relatively small film thicknesses and the inherent connection with the substrate in epitaxy lead to a limitation on the amount of disorder possible. This allows the sharp peak to persist even when the film is not fully ordered. They note that there is experimental evidence that this phenomenon is linked to the "adhesion" between the film and substrate, explaining the fact that it is only observed in certain materials systems.

Barabash *et al.* provide expressions for the intensity of the broad and sharp components of the ω-scan based on scattering theory for bulk crystals.[111] They include the effects of misfit dislocations. They

find that the presence and strength of the sharp peak is controlled by the magnitude of the Debye-Waller factor (DWF) for the situation in question. The DWF is an exponential term that decreases the intensity of elastic x-ray scattering based on the displacement of atoms from their ideal lattice positions. It can be used to account for thermal vibrations as well as displacements due to disorder. Barabash show that the exponent in the DWF scales with film thickness, *i.e.* $\text{DWF} \propto e^{-t}$, for layers less than 150 nm thick.

Kaganer *et al.* present perhaps the most complete investigation of the dual-lineshape phenomenon.[112, 113] They state that misfit dislocations are responsible for the two-component lineshape and that academic agreement has been reached on this point. They perform Monte Carlo calculations reproducing the lineshape and show that it is far more likely to observe the sharp peak component when the misfit dislocations are correlated in position. Uncorrelated dislocations reduce the strength of the sharp peak by two orders of magnitude. Kaganer additionally argues similarly to Barabash that the DWF for the coherent peak remains finite, *i.e.* non-zero, for epitaxial films. He also shows that the dimensionless parameter ρt controls the type of diffraction from the crystal, where ρ is the linear dislocation density and t is the film thickness. Low values of ρt lead to stronger coherent peaks. This result is again similar to that of Barabash in that it makes a connection between the strength of the sharp peak and film thickness.

Figure 57 shows the dependence of the sharp peak signal in our ω x-ray scans on film thickness. As with the authors mentioned above, we see a clear trend towards smaller coherent peaks as the films get thicker. We would not expect to see a perfectly linear relationship in the plot because the films in our experiments were not grown under identical conditions. The decreased intensity of the sharp peak signal with film thickness fits with the traditional critical thickness picture, but also seems to be consistent with the other interpretations discussed above. Similarly to Zaitsev *et al.*[107] the spacing of pendellösung fringes in our ω–2θ scans matches what is expected from the full thickness of our films, implying that the highly ordered material is present throughout.

Our films may be growing in a columnar fashion, with many vertically oriented columns originating at the substrate interface. There would be disorder at the boundaries between columns, and as the film grew thicker, the connection with the substrate would be lessened. Eventually there could start to be "interference" between columns and the "perfect" vertical orientation could be lost. This columnar interpretation would fit with the mottled surfaces seen in our AFM

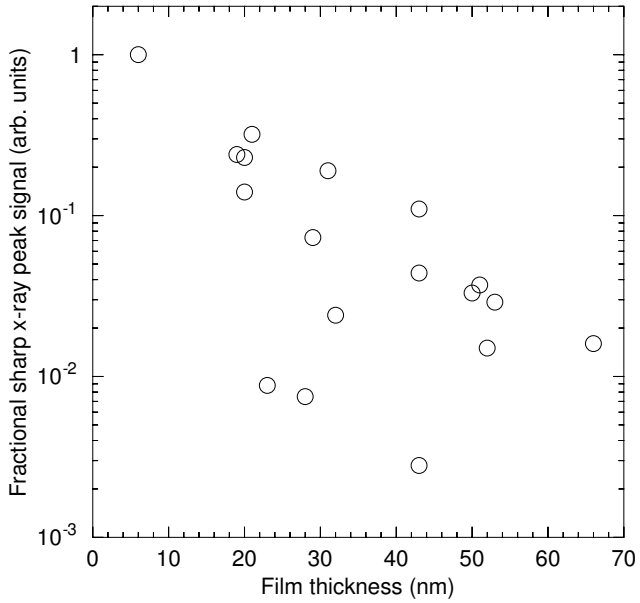

Figure 57: Variation of the sharp peak signal in ω x-ray scans with film thickness. The peak signal generally decreases with increasing film thickness. The vertical axis is plotted logarithmically for comparison with Barabash *et al.*'s result that the exponential DWF scales with film thickness.[111]

images, such as in figure 54. The spots on the surface could be the tops of columns of Y_2O_3.

Turning to the concept of misfit dislocations originating at the substrate film interface, the fact we see evidence of very low diffusion during growth may argue against the idea of dislocations propagating through previously deposited material. It could take too much energy to rearrange all of the atoms in the necessary fashion. Additionally, preliminary plan-view and cross-sectional transmission electron microscope images taken by our collaborator Shawn Penson lack the characteristic straight lines usually seen from misfit dislocations.

It is interesting that despite the variety of materials systems and conditions under which this sharp and broad scattering pattern can be observed, and with the range of possible interpretations, that the experimental results are very similar. The phenomenon appears to be "universal" and even with possibly different specific details of the defects present in the materials, the underlying physics appears to be the same. With this in mind, we will proceed with our analysis based on equation 4.3. Regardless of the distribution of the highly ordered material in the film, the "critical thickness" value is useful for comparison of the relative quality of our samples.

Figure 58a shows a plot of our "critical thickness" as a function of growth rate for nine samples deposited at 800 °C. Films grown at a lower rate had less broad peak signal, signifying a higher quality and larger critical thickness. The relationship was determined to be

$$t_c \sim F^{-0.6} \tag{4.4}$$

where F is the flux of material landing on the substrate, which is proportional to the growth rate. Figure 58b shows the effect of temperature on critical thickness for six samples grown at similar rates, between 11 and 15 nm/hr. Growing at a higher temperature increased quality up to 800 °C, beyond which crystallinity decreased. The extremely low critical thicknesses for the films grown at the very low and high temperatures of 400 and 1000 °C likely indicate the presence of only small areas in the crystal with structural perfection. An activation energy of 0.3 eV was determined from an Arrhenius fit to the data up to the optimal temperature. This value is much lower than the bond energy but could indicate that a lower-energy structural relaxation is involved in the film growth.

It is not surprising that a low growth rate can improve film quality, as the incoming atoms will have more time to arrange themselves correctly, but the growth rates with the best results here of around 10 nm/hr are two orders of magnitude lower than typical values for semiconductor growth. Unfortunately, for solid state laser applications relatively thick films are desired, up to many microns. If extreme crystalline quality is desired, a new method may need to be devised to increase the growth rate. The relatively low optimal growth temperature of 800 °C is consistent with the usual rule of thumb for MBE that the growth temperature be half the bulk melting temperature, which in this case is 2430 °C. Nieh *et al.* reported a similar growth temperature of 780 °C.[66]

We can use the data in figure 58 to estimate an activation energy for the surface diffusion that occurs during growth. We expect growth phenomena including the critical thickness to vary with $\left(\frac{F}{D}\right)^{\gamma}$ where F is the incident atomic flux, D is the diffusion constant, and γ is a variable parameter depending on the size of atomic clusters taking part in the diffusion.[15] From figure 58a we can equate the growth rate with the flux, F, and determine that γ is about -0.6. Now, the

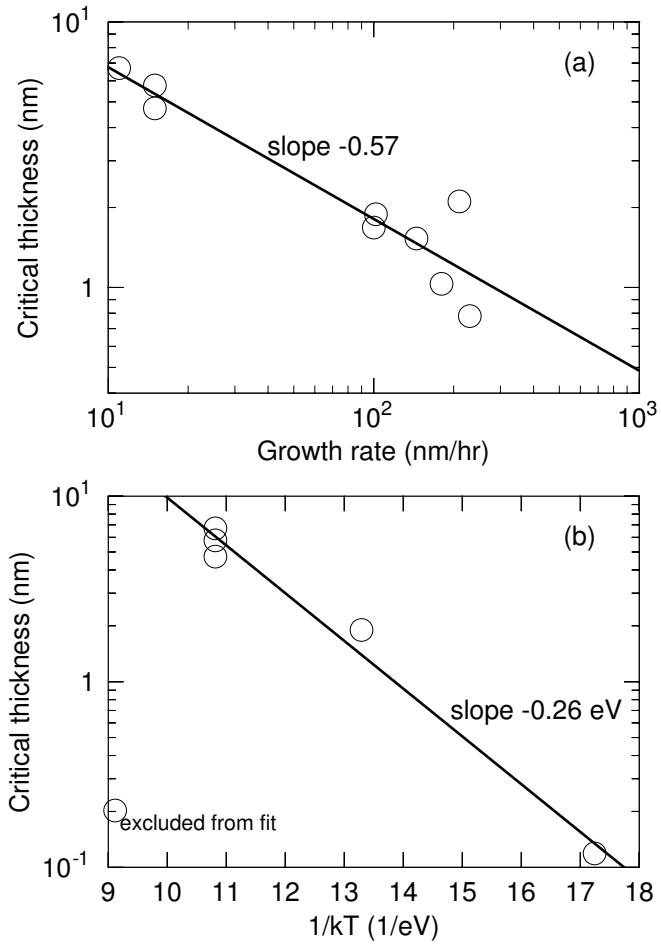

Figure 58: (a) Variation of Y_2O_3 critical thickness with growth rate, as determined from an analysis of ω x-ray scans such as those in figure 55b (see text). (b) Variation of Y_2O_3 critical thickness with growth temperature. Only values from samples grown with similar growth rates (around 15 nm/hr) are shown in this plot, limiting the number of data points. Results from samples grown at higher rates are consistent with this trend.

temperature dependent process we examined in figure 58b, with activation energy 0.3 eV, can be analyzed as follows:

$$t_c \propto e^{-\frac{0.3}{k_b T}} \propto (\frac{1}{D})^{\gamma} \propto \left(\frac{1}{e^{-\frac{E_a}{k_b T}}}\right)^{\gamma} \propto (e^{\frac{E_a}{k_b T}})^{\gamma}, \tag{4.5}$$

where t_c is the critical thickness, as before. With $\gamma = -0.6$, the activation energy, E_a, in equation 4.5 for the surface diffusion during growth is 0.5 eV. This agrees with the value we determined during the annealing experiments in section 3.3.4. This activation energy is very small, but the amount of diffusion could also be small, as indicated above, if the D_0 prefactor for the diffusion constant (see equation 3.2) was small as well. This could result from a complex reorganization of Y_2O_3 molecules being required for diffusion. The value for γ of -0.6 could also indicate that several Y_2O_3 clusters take part in the diffusion process, because for some physical regimes the magnitude of γ scales with the number of participating atomic clusters.[15]

Following the method of Herres *et al.*,[114] ω scans of the Y_2O_3 (222), (444), and (666) peaks were measured in order to determine the origin of the broad background. Broadening due to mosaicity, *i.e.* crystallite tilt, will not vary with the Bragg angle (and therefore peak order), but broadening due to a finite-size effect from small in-plane crystallites will decrease for higher-order peaks. This allows the two effects to be separated. The two broadening terms are given by

$$\Delta k_{mosaic} = \Delta_{mosaic} k_{\perp} \tag{4.6}$$

$$\Delta k_{size} = \frac{1}{< t_{\parallel} >}, \tag{4.7}$$

where the Δk terms are the in-plane reciprocal peak broadenings, Δ_{mosaic} is the average crystallite tilt, $k_{\perp}$ is the out-of-plane reciprocal coordinate of the peak, and $< t_{\parallel} >$ is the average crystallite size in the in-plane direction. Assuming the broadenings are normally distributed and uncorrelated, they will sum in quadrature, and we can write

$$\Delta k_{\parallel}^2 = \Delta k_{mosaic}^2 + \Delta k_{size}^2 \tag{4.8}$$

$$= (\Delta_{mosaic} k_{\perp})^2 + \frac{1}{< t_{\parallel} >^2}. \tag{4.9}$$

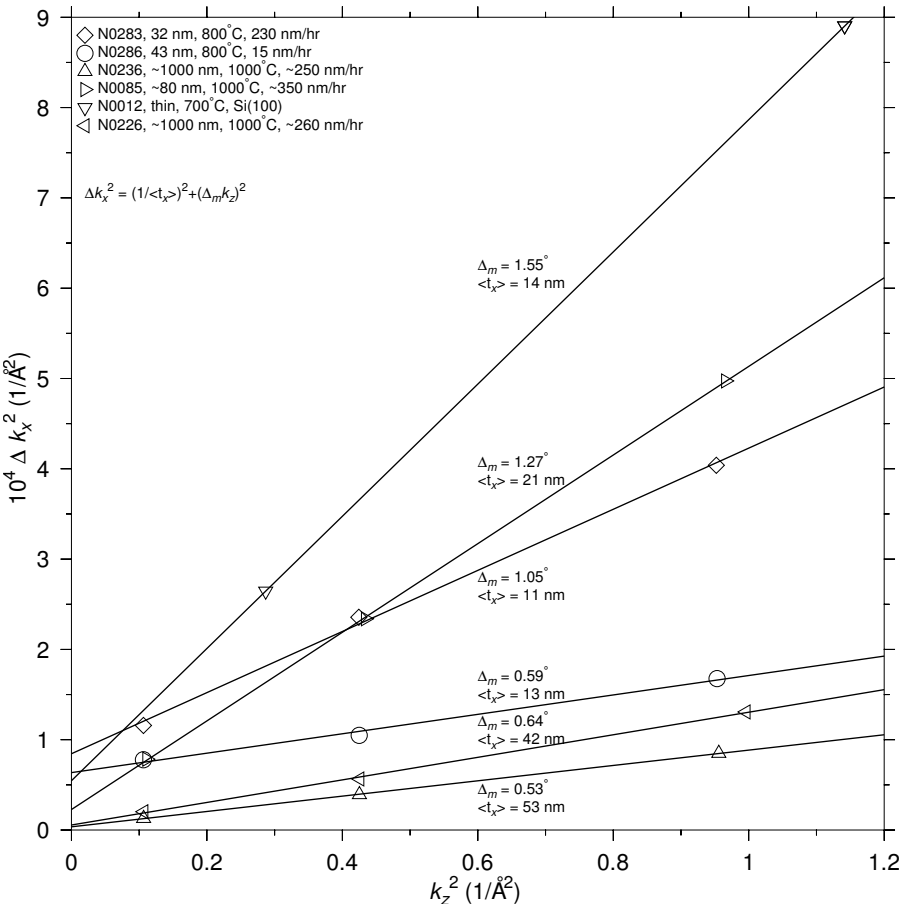

Figure 59: Reciprocal space broadening analysis for a selection of Y_2O_3 films. The slope and intercept from each linear fit gives the indicated mosaic tilt and mean crystallite size (see text).

Now we can plot $\Delta k_{\parallel}^2$ against $k_{\perp}^2$ and extract the broadenings from the slope and intercept of a linear fit. Figure 59 shows some examples of this type of analysis.

For our samples the mosaicity and crystallite size did not vary significantly with growth rate or temperature. The mosaic tilt was between 0.6° and 1.9° and crystallite size was between 8 and 24 nm, as determined from equation 4.9. At these levels both effects make a significant contribution to the background in the ω scans. The crystallite size matches the length scale of the small bumps that make up the mottled pattern visible in AFM images; see, for example, figure 54, where the average crystallite size is indicated with a black circle. The crystallite size determined here could be a measure of the diameter of columns of material as discussed above. It is not entirely clear how

this size would affect the in-plane width of the sharp vertical streak in the reciprocal space maps, *e.g.* figure 56. Boulle *et al.*[109] state that the thin streak is possible because their "columns" are much wider than the film thickness (127 nm wide and 17 nm thick in their simulations), but our in-plane sizes are much closer to the film thicknesses. Our much simpler analysis of only the diffuse peak signal may be less appropriate for interpreting the two-component peak shapes.

4.2 HIGH-RESOLUTION X-RAY RECIPROCAL SPACE MAPS

Many x-ray reciprocal space maps recorded from thin Y_2O_3 films showed very sharp features in the in-plane k_x direction, as discussed above. Figure 56 shows this thin vertical streak, which is indicative of the near-perfect crystal layer discussed in section 4.1. To investigate this further, we collected even higher-x-axis-resolution, space maps and discovered a number of related phenomena of interest.

Figure 60 shows a space map from a 20 nm thick Y_2O_3 film on R-Al_2O_3, which has approximately 10 times the x-axis resolution as figure 56. We see subpeaks in the vertical stripe, which can also be seen in ω–2θ scans as pendellösung finite-thickness fringes. We notice two satellite peaks in the horizontal stripe of the film peak. These peaks were also visible in space maps from other samples. To investigate the origin of these peaks, we changed the alignment of the x-ray beam with respect to that of the atomic step edges on the sample surface by rotating the sample in the diffractometer. The satellite peak spacing varied predictably with the projection of the atomic step spacing and we were therefore able to determine that the satellite peaks are caused by the atomic steps and have a spacing given by the miscut of the wafer. In this case, for instance, the peak spacing of 0.1° matches the miscut of the substrate. Since the Y_2O_3 film is conformal, the atomic step spacing is the same as before growth. Higher order side peaks were also visible in some ω scans.

We expect from the convolution theorem that the reciprocal/Fourier space representation of the multiplication of two real-space patterns will be equal to the convolution of the Fourier transforms of the individual patterns. Here the patterns are the periodic crystal, with a characteristic spatial frequency of $\frac{2\pi}{a}$, where a is the plane spacing, and the atomic steps, with a spatial frequency of $\frac{2\pi}{L}$, where L is the step width. With the step edges running perpendicular to the scattering plane, the result, in our two-dimensional reciprocal space representation, will be a series of subpeaks in the horizontal direction on each

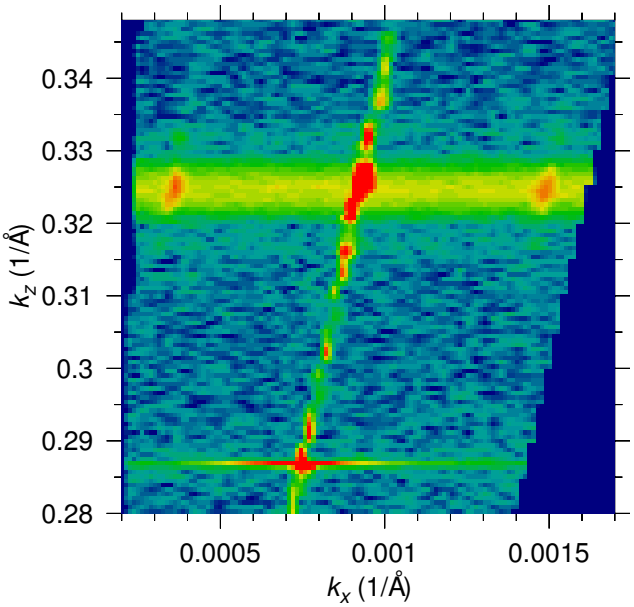

Figure 60: X-ray reciprocal space map from Y_2O_3 on R-Al_2O_3. Finite-thickness satellite peaks are visible on the film peak in the vertical stripe. The satellite peaks in the horizontal film peak stripe are due to the atomic steps on the sample surface and have an angular spacing equal to the wafer miscut. The horizontal offset between the film and substrate peaks is caused by a combination of film tilt and sample misalignment in the diffractometer. A logarithmic colour scale is used.

reciprocal lattice point. A change in scattering amplitude is required to generate this pattern. The difference in phase between scattered waves from different crystal planes is 2π and gives constructive interference, the origin of Bragg diffraction. In our case of a 20 nm thick film, variations in film thickness at step edges on the order of a unit-cell dimension of around 1 nm would lead to an amplitude modulation of about 5%. Similarly, the unit-cell sized disruption at a step edge would be about 1% of the step width of around 150 nm. It is reasonable to believe that phenomena of these scales could be observable by x-ray diffraction, which has many orders of magnitude of dynamic range. In figure 60 the subpeaks have intensities approximately 1% of the main film diffraction spot, the same as the 1% disruption mentioned above. Geometrically, the angular separation of the subpeak will be given by

$$\Delta\omega = \tan^{-1}\left(\frac{2\pi}{L}\frac{a}{2\pi}\right) = \tan^{-1}\frac{a}{L}, \tag{4.10}$$

which is simply the miscut of the wafer, in agreement with our measurements.

An alternate explanation for the satellite peaks is given by Kaganer *et al.* in one of their papers about correlated misfit dislocations discussed above.[113] They generate satellite peaks in their Monte Carlo simulations with spacings equal to the inverse dislocation density. The satellite peaks are only visible in situations where the correlation is strong, meaning that the dislocation spacing is very uniform. This is very similar to our case of atomic steps. We presented some arguments against propagating misfit dislocations in section 4.1. Nevertheless, it could be that we have misfit dislocations originating from the step edges at our substrate-film interface. This would be a logical place for dislocations to form because the crystal is disrupted by the step edge. However, these satellite peaks could be an example of another universal type of phenomenon with similar experimental manifestations resulting from different physical origins.

The thin vertical stripe in figure 60 still does not appear to be fully resolved, so space maps were recorded with a further factor of 10 refinement in the x-axis. Figure 61 shows an example map, this time on the same 21 nm thick Y_2O_3 sample used in figure 56. The finite-thickness fringes are now resolved as round peaks. Interestingly, these peaks are not arranged in a perfectly straight line, but instead they weave back and forth in a "zig-zag" pattern. The angle from vertical of the overall line between the substrate and film peaks is exaggerated by the very fine horizontal scale and is due to a slight misorientation,

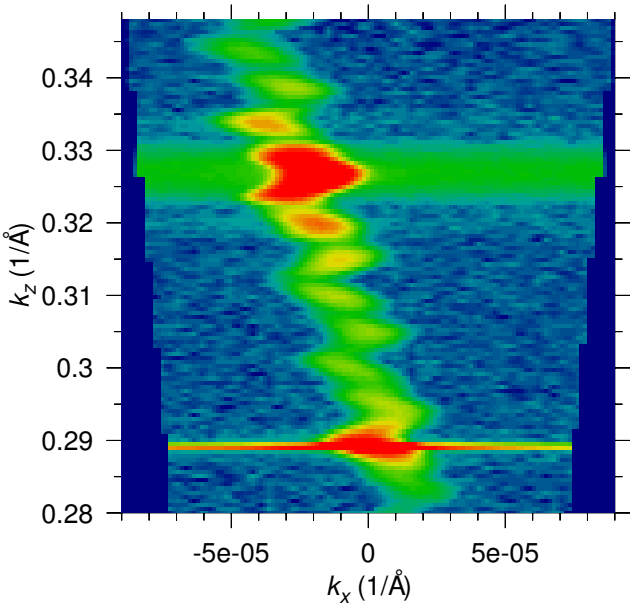

Figure 61: X-ray reciprocal space map from Y_2O_3 on R-Al_2O_3. This is a much closer look, with a finer x-scale, at the vertical stripe from figure 56. As before, the peak at the bottom of the image is the substrate peak, and the streak in the upper part is the film peak. The "zig-zag" pattern was commonly seen from high-quality thin Y_2O_3 films. A logarithmic colour scale is used.

or tilt, of the sample with respect to the x-ray stage. While it may be logical to associate the zig-zag with the stepped surface of the film, analysis of the length scales and angles involved were inconclusive, and we did not determine the origin of this phenomenon.

4.3 DYNAMICAL DIFFRACTION

Often epitaxial growth can provide very-high-quality crystal layers, and the flexibility of this technique allows the production of complicated multilayer structures. These types of samples can produce quite complicated x-ray diffraction patterns, including some effects that are not predicted by traditional kinematic theory. In these cases it is desirable to use so-called dynamical diffraction theory, which takes into account the wave nature of the x-rays and provides a proper model for even the most problematic systems.

Dynamical diffraction theory was developed before the rise of modern epitaxial techniques as a way of modelling curved crystals by considering them to be a series of separate layers. Takagi[115] and

Taupin[116] developed similar theories independently in the 1960s. Interest in the theory surged after the advent of multilayer epitaxial growth. Dynamical diffraction theory correctly predicts such effects as pendellösung finite-thickness fringes and small-film-thickness Bragg peak shifts.

Implementing a custom software simulation package allows us to model a variety of crystal structures that are not present in commercial software, such as yttrium oxide, all orientations of sapphire, and various mixed oxide layers. Our implementation follows the method of Bartels *et al.*[117] A recursive method is used to solve the Taupin differential equation for the amplitude ratio of the incoming, D_0, and outgoing, D_H, x-ray beams, where D is the electric displacement. Assuming the x-ray source is of constant intensity, the ratio $|D_H/D_0|^2$ is the simulated x-ray signal. The recursion is over the layers of the sample. We start at the top of the substrate, which is assumed to be infinitely thick, and then calculate the new intensity at the top of every successive layer.

The derivation of the Taupin equation is complicated, but it begins with Maxwell's equations:

$$\vec{D} = \varepsilon_0(1+\chi)\vec{E}, \tag{4.11}$$

$$\vec{B} = \mu_0\vec{H}, \tag{4.12}$$

$$\nabla \cdot \vec{D} = 0, \tag{4.13}$$

$$\nabla \cdot \vec{B} = 0, \tag{4.14}$$

$$\nabla \times \vec{E} = -\frac{\partial \vec{B}}{\partial t}, \tag{4.15}$$

$$\nabla \times \vec{H} = \frac{\partial \vec{D}}{\partial t}, \tag{4.16}$$

which are then arranged, assuming the periodic susceptibility of the crystal χ is small, to yield:

$$\nabla \times \nabla \times (1-\chi)\vec{D} = \frac{4\pi^2}{\lambda^2}\vec{D}. \tag{4.17}$$

Now, using a periodic Bloch form for D and with much manipulation and approximation, the differential equation of a slightly modified x-ray amplitude ratio called X can be written as[116, 117]

$$-i\frac{dX}{dT} = X^2 - 2\eta X + 1, \tag{4.18}$$

where X, η and T are complex quantities given by

$$X = (\frac{F_{\bar{H}}}{F_H})^{\frac{1}{2}} |\frac{\gamma_H}{\gamma_0}|^{\frac{1}{2}} \frac{D_H}{D_0}, \tag{4.19}$$

$$\eta = \frac{-b(\theta - \theta_B)\sin 2\theta_B - \frac{1}{2}\Gamma F_0(1-b)}{|b|^{\frac{1}{2}} C\Gamma(F_H F_{\bar{H}})^{\frac{1}{2}}}, \tag{4.20}$$

$$T = \frac{\pi C\Gamma(F_H F_{\bar{H}})^{\frac{1}{2}} t}{\lambda|\gamma_0\gamma_H|^{\frac{1}{2}}}, \tag{4.21}$$

with

$$\Gamma = \frac{r_e\lambda^2}{\pi V}, \tag{4.22}$$

$$r_e = \frac{e^2}{4\pi\varepsilon_0 mc^2}, \tag{4.23}$$

$$b = \frac{\gamma_0}{\gamma_H}. \tag{4.24}$$

We quote from Bartels for explanations of the terms:[117]

> T is determined by the crystal thickness t and the structure factor F_H of the reflection. The departure from the Bragg angle θ_B determines the deviation parameter η. The second part of the numerator of η corresponds to the refraction and absorption of the X-rays. In the Bragg case the direction cosines γ_0 and γ_H of the incident and the diffracted beam with respect to the surface normal are opposite in sign so that the asymmetry factor b is negative. The classical electron radius r_e is equal to 2.818×10^{-5} Å, λ is the X-ray wavelength and V is the volume of the unit cell. $C = 1$ for perpendicular (σ) polarization and $C = |\cos 2\theta_B|$ for parallel (π) polarization of the incident beam.

The structure factor F_H is a complex-valued unitless measure of the strength of scattering from the material, incorporating both the scattering factors for the atoms as well as the geometry of the crystal. It is given by:

$$F_H = \sum_j f_j e^{2\pi\Delta\vec{k}\cdot\vec{r}_j}. \tag{4.25}$$

where the sum runs over all the atoms in the unit cell, f_j is the scattering factor of the atom, $\Delta\vec{k}$ is the scattering vector, and $\vec{r}_j$ is the fractional position vector of the atom in the unit cell.[73] As an example, consider the term in the sum for the arsenic atom at the

X-ray peak	Structure factor
Y_2O_3 (222)	$-963 - 58.7i$
Al_2O_3 (006)	$-11.2 + 1.66i$
Al_2O_3 (102)	$-47.9 - 0.893i$
Al_2O_3 (110)	$62.7 + 2.65i$
GaAs (004)	$153 + 6.75i$

Table 4: Example structure factors calculated with the dynamical diffraction software.

$(\frac{1}{4}, \frac{1}{4}, \frac{1}{4})$ position in the zincblende GaAs structure. For the (004) diffraction peak we simply have $\Delta\vec{k} = (0, 0, 4)$ and $\vec{r} = (\frac{1}{4}, \frac{1}{4}, \frac{1}{4})$ so in this case $e^{2\pi\Delta\vec{k}\cdot\vec{r}} = 1$. Note that the structure factor is complex both because the atomic scattering factors are complex and because the spatial part can itself be complex. Some further discussion can be found in appendix C and in the work of Cole and Stemple.[118] They also describe a related method for computing the quantities $(F_H F_{\bar{H}})^{\frac{1}{2}}$ and $|F_H/F_{\bar{H}}|$. The latter ratio is unity in our usual simple case, as described below. Note that with $F_H = F_{\Delta\vec{k}} = F_{(h,k,l)}$, $F_{\bar{H}} = F_{-\Delta\vec{k}} = F_{(-h,-k,-l)}$. Table 4 shows some structure factors calculated with our software.

The recursive solution to equation 4.18 found by Bartels for multi-layered structures is as follows. For a given x-ray amplitude ratio at the bottom of a layer, X_0, the amplitude ratio at the top of that layer is

$$X_t = \eta + (\eta^2 - 1)^{\frac{1}{2}} \left[\frac{S_1 + S_2}{S_1 - S_2} \right], \tag{4.26}$$

where

$$S_1 = [X_0 - \eta + (\eta^2 - 1)^{\frac{1}{2}}] e^{-iT(\eta^2-1)^{\frac{1}{2}}}, \tag{4.27}$$

$$S_2 = [X_0 - \eta - (\eta^2 - 1)^{\frac{1}{2}}] e^{iT(\eta^2-1)^{\frac{1}{2}}}. \tag{4.28}$$

For the initial starting value at the top of the infinitely thick substrate we can use the Darwin formula, modified by Prins for absorption, for the rocking curve of a perfect crystal:[119]

$$X_\infty = \eta \pm (\eta^2 - 1)^{\frac{1}{2}}, \tag{4.29}$$

where the sign is chosen to be the opposite of Re(η). Each individual calculation gives the x-ray intensity for a single diffraction angle, $\theta - \theta_B$.

Thankfully the computer can easily compute values for any angular range and resolution.

For symmetric reflections, such as our usual case of Bragg peaks for crystal planes parallel to the film surface, γ_0 and γ_H are equal in magnitude and opposite in sign, making $b = -1$. F_H and $F_{\bar{H}}$ are also equal in magnitude, and equations 4.19 and 4.20 simplify to:

$$X = \frac{D_H}{D_0}, \tag{4.30}$$

$$\eta = \frac{(\theta - \theta_B)\sin 2\theta_B - \Gamma F_0}{C\Gamma(F_H F_{\bar{H}})^{\frac{1}{2}}}, \tag{4.31}$$

with the diffracted x-ray intensity just given by $|X|^2$.

The software package takes information about the substrate and epilayer as inputs, including the crystal structures and film thickness. In particular, the lattice constants of the layers are used directly. This means that if stress and strain are to be taken into account, then those calculations will have to be done in advance and the resulting lattice constants used. See section 4.4 below for a discussion of stress and strain calculations. Appendix C contains an example input file.

Figure 62 shows a comparison of the measured x-ray $(11\bar{2}0)$ ω–2θ Bragg reflection from an A-plane sapphire substrate with a simulation from our software. Once the simulation is convolved with a 14″ FWHM gaussian, the approximate resolution of the diffractometer, the agreement is excellent. A more useful simulation is the case of Y_2O_3 on R-Al_2O_3. Figure 63a shows a simulation of the x-ray data from figure 55a, showing that finite-thickness fringes are properly reproduced. The simulated thickness used is 21 nm, the same as that measured by x-ray reflectivity.

As described above, part of the calculation required to simulate diffraction spectra is the determination of the structure factor, which requires knowledge of the atomic scattering factors for the atoms in the crystal, along with their positions in the unit cell. Figure 63b shows how the choice of atoms and therefore scattering factors influences the simulation results. A 20 nm thick Ga_2O_3 film on A-plane sapphire is simulated in three ways: using the correct atomic composition, by replacing all Ga atoms with Al, and by replacing all Ga atoms with Nd. Regardless of the data scaling used, the simulation using the Ga atoms provides the best fit to the data.

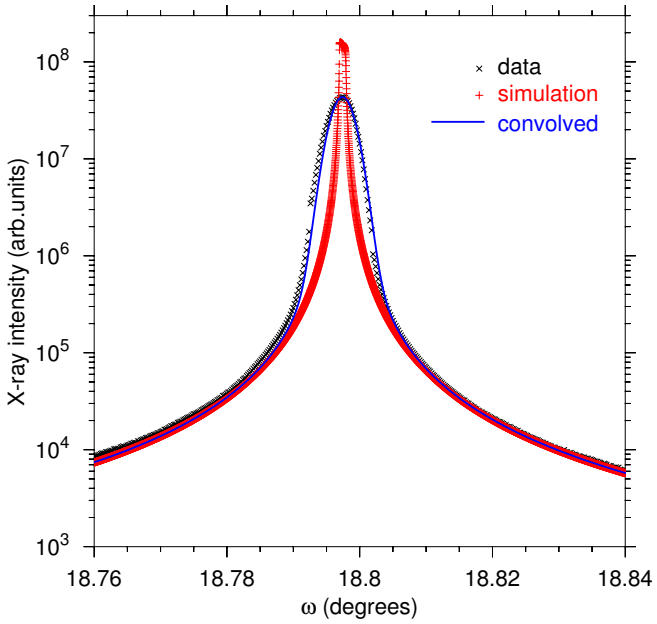

Figure 62: Comparison of a simulated sapphire $(11\bar{2}0)$ ω–2θ Bragg reflection with experimental data. The blue line is the simulation result after convolution with a 14″ FWHM gaussian, which is approximately the diffractometer resolution.

4.4 STRESS AND STRAIN

An important refinement to x-ray diffraction simulations of epitaxial systems is the incorporation of stress and strain effects. In epitaxial growth the deposited layer is influenced by the underlying substrate lattice. The ideal situation is for the in-plane lattice constants of the epilayer to expand or contract to perfectly match the substrate. When this happens the lattice in the out-of-plane direction also changes in a way predicted by elasticity theory.

Stress, σ, and strain, ϵ, are related by a fourth-rank tensor, either the stiffness c_{ijkl} or compliance s_{ijkl}, with $[c] = [s]^{-1}$:

$$\sigma_{ij} = c_{ijkl}\epsilon_{kl}, \tag{4.32}$$

$$\epsilon_{ij} = s_{ijkl}\sigma_{kl}, \tag{4.33}$$

where the Einstein summation convention over repeated indices is implied.[1] Many of the terms in the stiffness/compliance tensors are indistinguishable—c_{1112} and c_{1121}, for instance. For convenience, it is

1 For example, $\sigma_{24} = \sum_{k=1}^{3}\sum_{l=1}^{3} c_{24kl}\epsilon_{kl}$.

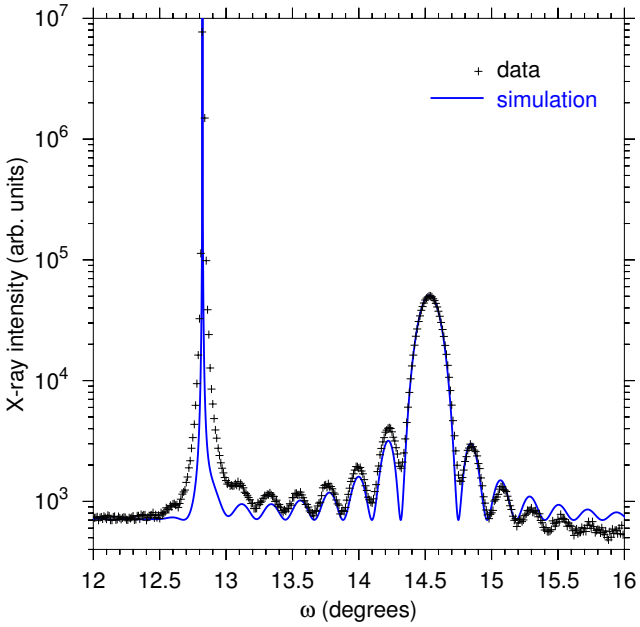

(a)

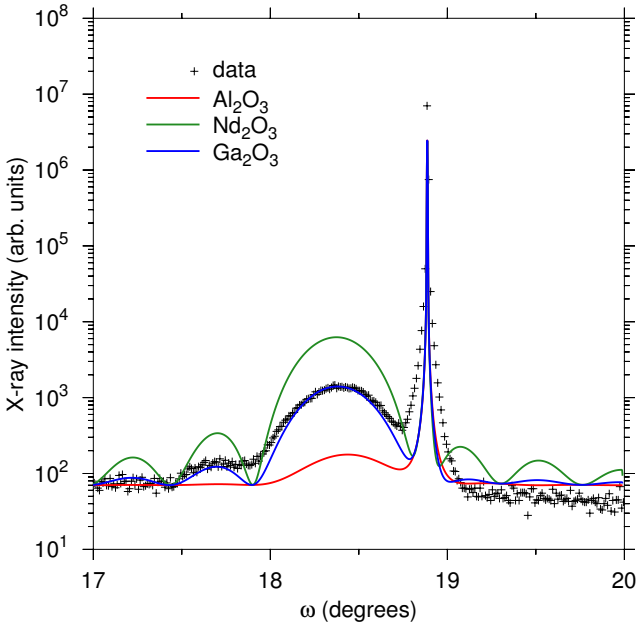

(b)

Figure 63: (a) Simulation of ω–2θ finite-thickness fringes from a 21 nm thick Y_2O_3 film on R-Al_2O_3. The film thickness determined from the dynamical x-ray simulation is the same 21 nm determined from x-ray reflectivity measurements. (b) ω–2θ simulation for a 20 nm thick Ga_2O_3 film on A-plane sapphire. The three simulated curves are assuming the film has the indicated composition. While the curves could be rescaled, the "correct" Ga_2O_3 composition gives the best fit to the data. Experimental data courtesy Raveen Kumaran.

standard to adopt a two-suffix notation, with the following transformations:

$$11 \to 1, \quad 22 \to 2, \quad 33 \to 3, \quad 23 \to 4, \quad 13 \to 5, \quad 12 \to 6.$$

With the equivalence of 23=32, 13=31, and 12=21, equations 4.32 and 4.33 now become:

$$\sigma_i = c_{ij}\epsilon_j \tag{4.34}$$

$$\epsilon_i = s_{ij}\sigma_j. \tag{4.35}$$

The stiffness, and less frequently compliance, values using this convention can be found in the literature for various materials. Now, given a set of conditions, we can determine how materials deform.

One of the most obvious starting points would be to apply a set of known stresses to an object and then use equation 4.35 and the compliance values to calculate all of the strains. A slightly more complicated case occurs for typical epitaxial growth. Here we generally assume that the grown material is pseudomorphic, *i.e.* it matches the lattice constant of the substrate, in the in-plane directions, but is free to expand or contract in the out-of-plane direction. The latter condition is equivalent to having zero stress in the out-of-plane direction. If the in-plane directions are x and y (1 and 2) and the out-of-plane direction is z (3), then we can calculate ϵ_1 and ϵ_2 from the lattice mismatch, and we know that $\sigma_3 = \sigma_4 = \sigma_5 = \sigma_6 = 0$. This results in a set of six equations with six unknowns, so we can now solve for the out-of-plane strain or the other quantities. For a non-triclinic crystal many of the stiffness elements will be zero, which often greatly simplifies the form of the equations. Symmetry considerations also reduce the number of independent coefficients.

For an isotropic material in our epitaxial example above, we find that

$$\epsilon_3 = -\frac{2c_{12}\epsilon_1}{c_{11}}. \tag{4.36}$$

For another more specific example, consider the case of growing on an A-plane $(11\bar{2}0)$ sapphire substrate. Assuming hexagonal symmetry and designating the out-of-plane direction with the 2 subscript, we find that

$$\epsilon_2 = -\frac{c_{12}\epsilon_1 + c_{13}\epsilon_3}{c_{11}}. \tag{4.37}$$

However, the symmetry of sapphire is actually trigonal, and there is a non-zero c_{14} term. With this term included the out-of-plane strain is given by the slightly more complicated

$$\epsilon_2 = \frac{(c_{12} + \frac{c_{14}^2}{c_{44}})\epsilon_1 + c_{13}\epsilon_3}{\frac{c_{14}^2}{c_{44}} - c_{11}}. \tag{4.38}$$

In the case of sapphire the difference between equations 4.37 and 4.38 turns out to be small, around 2%.

Figure 64a shows a comparison of our simulation software with the commercial X'Pert Epitaxy package from PANalytical and the GID_sl software from the Argonne National Laboratory. The simulated system is a 20 nm thick pseudomorphic AlAs film on (001) GaAs. The AlAs lattice is distorted into a tetragonal geometry by the approximately 0.5% lattice mismatch with GaAs. All three results are very similar, validating the performance of our code. The reasons for non-perfect agreement are some small assumptions and the choice of materials constants used, such as the atomic scattering factors and lattice constants. Assumptions are discussed in the comments accompanying the code in appendix C.

Figure 64b shows a simulated ω–2θ spectrum for a 110 nm thick mixed Al-Ga oxide film compared with experimental data. In this case the position of the diffraction peak can be used to determine the out-of-plane lattice constant. Assuming pseudomorphic growth, and using elastic constants for sapphire, we can calculate the composition of the film. Here we found a composition of $Al_{1.38}Ga_{0.62}O_3$, which was somewhat different than the x-ray photoelectron spectroscopy (XPS) result of $Al_{1.22}Ga_{0.78}O_3$. The lack of agreement could be explained by non-pseudomorphic growth or significant variation of the elastic constants from the assumed values. The experimental film peak does not exhibit finite-thickness fringes, likely indicating imperfections in the crystal, such as non-uniformities in thickness or composition.

4.5 SUMMARY

We have shown that we can grow thin Y_2O_3 films of very high structural quality on annealed R-Al_2O_3. The determination of an optimal growth temperature of 800 °C should be useful for growing thicker Y_2O_3 layers. Similarly, our observation that high growth rates diminish crystal quality is relevant to the production of thick waveguides, where growth time becomes a limiting factor at low rates. Our dynam-

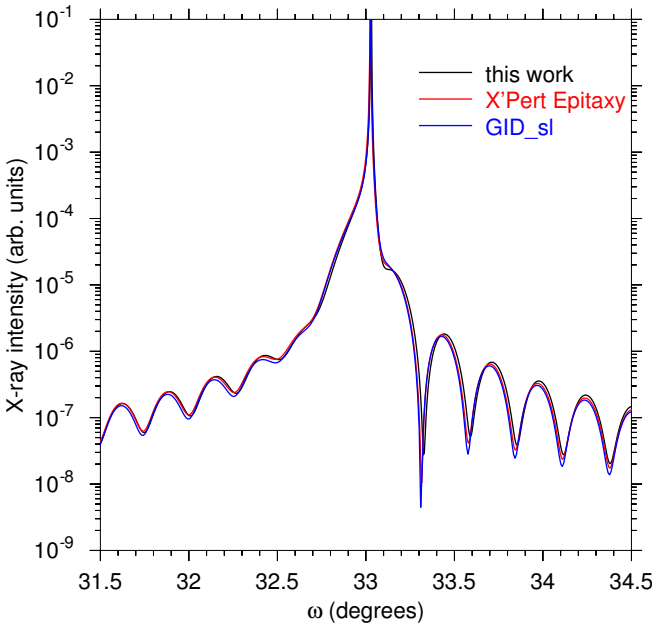

(a)

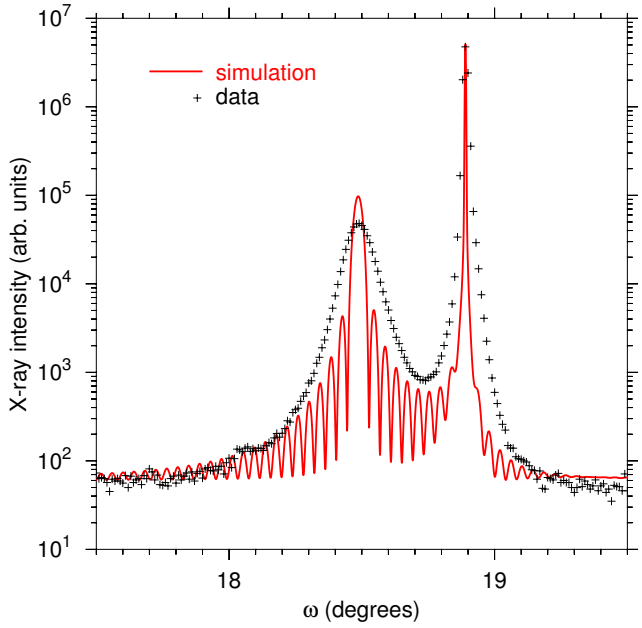

(b)

Figure 64: (a) ω–2θ x-ray simulation comparison using the model system of 20 nm AlAs on (001) GaAs. The results from our software are extremely similar to other offerings from PANalytical and the Argonne National Laboratory. (b) ω–2θ experimental data and dynamical diffraction simulation from a 110 nm thick mixed Al-Ga oxide on A-plane sapphire. The composition used in the simulation, assuming pseudomorphic growth, was $Al_{1.38}Ga_{0.62}O_3$, somewhat lower than the XPS-measured result of $Al_{1.22}Ga_{0.78}O_3$. Experimental data courtesy Raveen Kumaran.

ical diffraction package is applicable to a wide variety of materials, unlike most commercial offerings.

5 The search for a surfactant

In the context of molecular beam epitaxy, a surfactant is a substance that is deposited on the substrate during growth along with the desired crystal components. Ideally the surfactant "floats" on the surface of the growing epilayer and does not incorporate; its presence should positively impact one or more properties of the grown crystal film.

Surfactants can be an effective way to improve the quality of group IV[120] and III-V[121] semiconductor materials grown by MBE. Surfactants stay on the substrate, lowering surface energy and encouraging surface adatom diffusion.[122] Often large atoms are used, as their size prevents them from easily incorporating. Recently Suzuki *et al.*[20] published a paper on the use of atomic hydrogen as a surfactant during MBE ZnO growth. In similar fashion to the semiconductor studies, they were able to reduce surface roughness and improve crystal quality and photoluminescence. They also found that they could grow high-quality material at lower temperatures with a surfactant than without. This could have advantages such as aiding incorporation of a dopant. Suzuki's work suggests that surfactants may be able to make a large contribution to epitaxial oxide growth. Reducing surface roughness is particularly attractive for the waveguide applications because rough interfaces will cause light scattering.

5.1 Hydrogen

Our MBE system was able to introduce molecular hydrogen gas through the same source port as the oxygen: through the plasma source, which was usually not energized. We attempted to use a hydrogen flux during the growth of Y_2O_3 to influence film properties. Hydrogen should act as a bond terminator and could replace bridging oxygen atoms with OH groups. Changing the reactivity of the surface in this manner could lead to surfactant effects.

Four pairs of samples were grown on R-plane sapphire with a substrate temperature of 800 °C. At this temperature some hydrogen dissociation on the substrate surface may be possible. One sample from each pair was grown with H_2 and the other without. The pairs of films were 25, 30, 50, and 60 nm thick. The growth rates for these pairs were 15, 220, 100, and 160 nm/hr, respectively. In all cases, the

hydrogen pressure in the chamber was measured with an ion gauge before the oxygen was introduced and found to be about 3×10^{-6} torr. There was minimal difference between the pressure measured with the flux gauge in front of the substrate and the background pressure elsewhere in the chamber.

Using our critical thickness analysis described in section 4.1, we determined that the samples grown with hydrogen were superior for the 50 nm and 30 nm pairs but not for the others. The critical thicknesses increased from 1.7 to 1.9 nm and from 0.78 to 2.1 nm, respectively. For the 25 nm thick pair the critical thickness decreased from 6.7 to 5.8 nm and for the 60 nm thick pair the decrease was from 1.5 to 1.0 nm. The AFM measurements were similar in all cases and showed no conclusive change in overall roughness or surface morphology.

Two ways that the hydrogen flux could be modified in an attempt to cause more noticeable film changes would be to energize the plasma source or to increase the flow rate. However, a trial run with the plasma source turned on did not show any obvious differences, and the chamber pressure was already reaching the upper limit for our equipment during these growths.

5.2 GALLIUM

A conventional effusion cell loaded with Ga metal was added to the MBE growth chamber to allow the attempted use of gallium as a surfactant for Y_2O_3 growth. Ga deposition and subsequent re-evaporation after the cell shutter was closed was observed in tests on sapphire substrates. This lack of reactivity suggests the possibility of success as a surfactant. Additionally, the Ga_2O suboxide is volatile and can act as an etchant. This could increase oxygen mobility, and the interplay between deposition and etching could lead to improved crystallinity if ordered areas are preferentially retained.

Two sets of Y_2O_3 comparison samples with and without gallium flux were grown to evaluate any surfactant effect. One set consisted of approximately 70 nm thick films and the other consisted of 20 nm samples. All samples in this experiment were grown at a substrate temperature of 800 °C on R-plane sapphire. The yttrium flux was approximately 5×10^{-8} torr and the gallium flux was approximately 1×10^{-7} torr.

The films grown with and without Ga in the 70 nm thick set were practically indistinguishable in AFM and x-ray measurements, indicat-

ing that the Ga flux had little or no effect. The 20 nm thick films had very similar AFM results, with the sample grown without Ga having a 0.16 nm RMS roughness compared with 0.18 nm for the film grown with surfactant. The difference in x-ray results was more dramatic, with the no-gallium sample having a higher critical thickness based on our analysis discussed in section 4.1. The critical thickness was 4.6 nm for the sample grown without Ga and 2.8 nm for the film grown with a Ga flux.

It is possible that a much higher Ga flux would have a greater effect, since at a substrate temperature of 800 °C, all the gallium will evaporate quickly with little to no buildup on the surface. However, the effects that were seen in the thinnest test films seemed to be undesirable, as usually smoother films and sharper x-ray peaks are preferable.

5.3 CESIUM

Cesium is a large atom and would not be expected to easily incorporate in our films. Similarly to hydrogen, it could act as a bond terminator, creating non-directional ionic bonds that could favour surface mobility and therefore influence the growth process.

Since cesium has such a low melting point of 29 °C and a high vapour pressure of over 1×10^{-4} torr at the melting point, a simple in-house thermal source was constructed to introduce Cs to the growth chamber. The design was based on similar sources depicted in the literature.[123, 124] Figure 65 shows a schematic of the Cs source. A sealed glass ampoule containing 1 g of Cs under argon was loaded into a small Conflat nipple with a blank flange on one end and a Swagelok valve on the other. The valve was connected to a standard 4.5″ source port on the MBE growth chamber with several adapters. The ampoule was shaped like a test tube, with the lower end sealed and separated from the upper end by a thin glass membrane. The upper end contained a steel slug, allowing the use of a magnet outside the source to crack the membrane and release the cesium. The entire source was wrapped with a Watlow rod heater bent into a generally helical shape to conform to the source. The heater power was modulated by a temperature controller using feedback from an internal thermocouple in the heater. The source was wrapped in an insulating blanket, and an auxiliary thermocouple was attached to the valve body with a screw. While there was no line of sight through the valve when open, the high Cs vapour pressure and literature examples gave confidence that

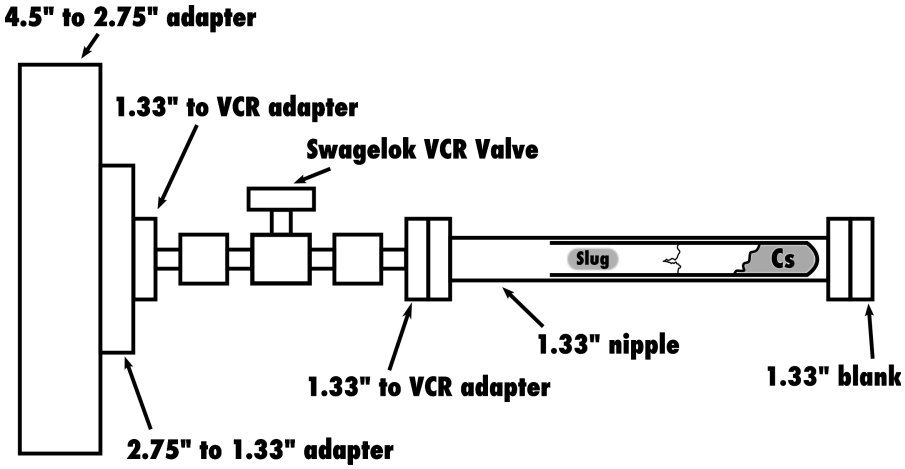

Figure 65: Schematic of the Cs surfactant source. A sealed glass ampoule containing cesium under argon gas was loaded into a Conflat nipple and attached to the MBE chamber via a Swagelok valve and several adapters. The ampoule was broken open by using a magnet to manipulate an iron slug inside the source. The entire source was wrapped in a heating element and insulation.

with sufficient temperature the Cs would evaporate out of the source and onto the substrate.

The source was attached to the MBE with the valve open so that it would be evacuated when the system was pumped down. Later the valve was closed and the steel slug manipulated with a magnet to crack open the ampoule. The valve was then very carefully opened to prevent any pressure burst from the small amount of Ar that had been released. There were no noticeable problems in terms of vacuum integrity. Unfortunately, when the source was heated to several hundred degrees Celsius, no flux could be measured with the flux gauge and no Cs or Cs compounds were found in the residual gas analyzer (RGA) spectrum. After the system was vented, the source was disassembled in an N_2 purged glovebag, and we found that the orifice in the ampoule membrane was exceedingly small and clogged. The hole was enlarged to 3 mm in diameter and the ampoule and source were reattached to the MBE.

In an effort to maximize the temperature of the valve and surrounding fittings with small orifices, additional heating tape and insulation was added to this section of the source. This enabled heating the valve up to 310 °C, just below the rated service limit of 315 °C, with the heater internal temperature reading 465 °C. Despite this high temperature relative to the Cs melting point and expected vapour pressure,

no flux was measured with the flux gauge. The RGA did show a very small peak just above the noise floor at the expected cesium mass of 133 amu. This peak disappeared when the source was cooled, so it does appear that some cesium exited the source, but not nearly enough to have any surfactant effect.

When the source was later disassembled it was quite clean and not filled with debris or any apparently cesium residue inside. It appeared that almost all of the Cs charge had stayed within the ampoule. It seems that the ampoule opening was easily clogged, likely with a more stable cesium oxide, preventing cesium escape. The main pool of cesium metal was likely also covered in a thin oxide layer, similarly inhibiting evaporation. It seems that using a standard effusion cell for cesium may be possible, though there are material handling concerns due to the extreme reactivity and possibility for spontaneous combustion.

6 Conclusion

Yttrium sesquioxide is a material of technological interest, both as a potential high-κ dielectric for semiconductor devices and as a solid state laser host material. The latter topic has been examined in this thesis. Y_2O_3 and related Y-Al oxides are suitable core layers in planar waveguide lasers when doped with rare-earth ions. Their high index of refraction and thermal properties are attractive for this application.

Molecular beam epitaxy is ideally suited to growing layered structures due to its fine control over growth rates and ability to form sharp interfaces. We have demonstrated that MBE is a feasible technique for deposition of Y_2O_3 on Al_2O_3, which is a satisfactory cladding layer for planar waveguides. The preparation of the Al_2O_3 substrates was shown to be important for controlling the structural properties of the Y_2O_3 epilayers. Annealing the substrates at 1150 °C for nine hours in air has proved a reliable method of generating atomically smooth surfaces, with parallel atomic steps easily visible in AFM measurements. Keeping the Al_2O_3 surface free of particles and contamination during post-annealing processing was somewhat difficult, though impact on the grown films appears to have been minimal. Ozone cleaning shows promise for the removal of residue generated in the wafer dicing process. X-ray diffraction and AFM characterization allow the condition of the substrate to be properly evaluated before growth.

Traditional MBE techniques, including the use of solid source effusion cells, RHEED, and light scattering, are practical and effective for the growth of oxides such as Y_2O_3. The optical properties of Al_2O_3 and Y_2O_3 make accurate growth-temperature measurement challenging, but stable conditions can be maintained with thermocouple feedback control and an SiC heater. No special oxygen source was required for Y_2O_3 growth, with molecular O_2 gas being sufficient to achieve full yttrium oxidation.

We have shown that using annealed R-plane Al_2O_3 substrates, moderate growth temperatures around 800 °C, and slow deposition rates under 100 nm/hr, allows the growth of thin {111}-oriented Y_2O_3 crystals with a very high degree of structural order. X-ray diffraction measurements including detailed reciprocal space maps show very sharp features in the in-plane direction and clear finite-thickness fringes in the out-of-plane direction. An activation energy for surface diffusion

of 0.5 eV was estimated. A critical-thickness-like phenomenon was observed, and the maximum "perfect" layer thickness achieved was 7 nm. Our analysis does not conclusively show that the very highly ordered material is present in a uniform layer at the bottom of the film, but the methods are applicable even if the ordered regions are distributed throughout the layer. In this case the 7 nm value would be an equivalent thickness of the distributed material.

The motivation for the thin-film experiments described above was to gain understanding of the growth process such that optimal thick films could be grown. A film thickness of at least 1 µm is required for a technologically feasible waveguide. A 0.6 µm thick Nd-doped Y_2O_3 film grown at the optimal temperature of 800 °C had a surface roughness of 5.8 nm RMS. Even at this insufficient thickness, the roughness had grown to a level that leads to an unacceptable level of scattering loss, exceeding 1 dB/cm.[71] The surface roughness needs to be below 4 nm and preferably significantly less than that. Surface roughness was shown to increase roughly proportionally with the square root of thickness.

The annealing of a Y_2O_3 film on a Al_2O_3 substrate presents an opportunity to study the interdiffusion of Al and Y in these crystals. We observed significant diffusion after annealing in air at temperatures above 800 °C and conclude that Al diffusion into the Y_2O_3 film is occurring without Y diffusion into the substrate. This means that post-growth annealing is not suitable for improving the properties of the Y_2O_3 films because new phases appear, consisting of other compounds in the Y-Al-O ternary system. We find an approximate activation energy for bulk diffusion of Al in Y_2O_3 of 3.0 eV. The surface of annealed Y_2O_3 films is observed to undergo drastic changes, generally becoming more rough. We estimate from AFM data that the activation energy for surface diffusion is (0.5 ± 0.3) eV, in agreement with the value found in our thin-film structural experiments mentioned above.

Our efforts to find an effective surfactant for Y_2O_3 growth were unsuccessful. Neither hydrogen nor gallium provided a consistent benefit to either structural quality or surface morphology. It is possible that the strong reactivity of yttrium and oxygen limited the influence of surfactant atoms on the crystal surface. Technical difficulties prevented the evaluation of cesium as another surfactant option. There is much room for further work in this area in particular, as is discussed in section 6.1.

MBE has proven to be capable of growing high-structural-quality Nd-doped Y_2O_3 films with strong luminescence on R-Al_2O_3. The optimal growth temperature was found to be approximately 800 °C. Lower growth rates were found to improve structural quality down to as low as 10 nm/hr. Surface roughness remains an issue to be addressed in terms of film suitability for planar waveguide laser devices.

6.1 FUTURE WORK

There are many possibilities for continuing this work, both from a basic research point of view and for technological applications. Creating a laser device is an obvious goal and requires the application of an upper cladding layer, the polishing of end facets, and the creation of a pumping system. An epitaxial cladding layer would seem ideal and could feasibly be deposited by MBE. We note that our collaborator Wei Li has deposited polymethyl methacrylate cladding layers *ex situ* for testing purposes.[71] Because the sapphire substrates are physically very hard, polishing the facets requires the use of diamond and can be difficult to accomplish without damaging the film-substrate interface. Once the raw waveguides are fabricated, a variety of pumping schemes should be possible, including simple edge butt-coupling of a laser diode bar.

The use of surfactants in oxide epitaxy is a research area deserving of more attention. Our experiments with gallium could be continued with a higher gallium flux and lower growth temperatures. A standard or low-temperature effusion cell could be suitable for cesium deposition. Bismuth has been used successfully as a surfactant in III-V semiconductor growth and could be appropriate for oxides as well.

Finally, there are a variety of other related materials systems beyond Y_2O_3 that can be investigated. In our own research group, Raveen Kumaran has worked on Al_2O_3 homoepitaxy[125] as well as YAG, YAP,[85] YAM, and Ga_2O_3[126] growth on Al_2O_3. YVO_4, $GdVO_4$, and $LuVO_4$ are other solid state laser hosts that could be explored using our techniques.

Bibliography

[1] D Look. *Materials Science and Engineering B*, **80**:383, 2001.

[2] Ü Özgür, Ya. I Alivov, C Liu, A Teke, MA Reshchikov, S Doğan, V Avrutin, S-J Cho, and H Morkoç. *Journal of Applied Physics*, **98**: 041301, 2005.

[3] T Fukumura, H Toyosaki, and Y Yamada. *Semiconductor Science and Technology*, **20**:S103, 2005.

[4] NJC Ingle, RH Hammond, and MR Beasley. *Journal of Applied Physics*, **91**:6371, 2002.

[5] GD Wilk, RM Wallace, and JM Anthony. *Journal of Applied Physics*, **89**:5243, 2001.

[6] AA Kaminskii. *physica status solidi (a)*, **200**:215, 2003.

[7] JI Mackenzie. *IEEE Journal of Selected Topics in Quantum Electronics*, **13**:626, 2007.

[8] GC Brown and AE Mussett. *The Inaccessible Earth*. Chapman and Hall, 2nd edition, 1993.

[9] VE Henrich and PA Cox. *The Surface Science of Metal Oxides*. Cambridge University Press, 1994.

[10] J Mannhart and DG Schlom. *Science*, **327**:1607, 2010.

[11] L Leung, D Davison, A Cornfeld, F Towner, and D Hartzell. *Journal of Crystal Growth*, **227**:143, 2001.

[12] B Joyce. *Reports on Progress in Physics*, **48**:1637, 1985.

[13] J Arthur. *Surface Science*, **500**:189, 2002.

[14] N Kaiser. *Applied Optics*, **41**:3053, 2002.

[15] A Pimpinelli and J Villain. *Physics of Crystal Growth*. Cambridge University Press, 1998.

[16] J Reiner, F Walker, and CH Ahn. *Science*, **323**:1018, 2009.

[17] DG Schlom, JH Haeni, J Lettieri, CD Theis, W Tian, JC Jiang, and XQ Pan. *Materials Science and Engineering B*, **87**:282, 2001.

[18] SA Chambers. *Journal of Physics: Condensed Matter*, **20**:264004, 2008.

[19] YF Chen, H-J Ko, S-K Hong, and T Yao. *Applied Physics Letters*, **76**:559, 2000.

[20] H Suzuki, T Minegishi, G Fujimoto, MW Cho, and T Yao. *Journal of the Korean Physical Society*, **49**:1266, 2006.

[21] SH Park, T Hanada, DC Oh, T Minegishi, H Goto, G Fujimoto, JS Park, IH Im, JH Chang, MW Cho, T Yao, and K Inaba. *Applied Physics Letters*, **91**:231904, 2007.

[22] E Cagin, J Yang, W Wang, JD Phillips, SK Hong, JW Lee, and JY Lee. *Applied Physics Letters*, **92**:233505, 2008.

[23] RW Ulbricht, A Schmehl, T Heeg, J Schubert, and DG Schlom. *Applied Physics Letters*, **93**:102105, 2008.

[24] NJC Ingle and IS Elfimov. *Physical Review B*, **77**:121202, 2008.

[25] C Webb, S-L Weng, JN Eckstein, N Missert, K Char, DG Schlom, ES Hellman, MR Beasley, A Kapitulnik, and JS Harris Jr. *Applied Physics Letters*, **51**:1191, 1987.

[26] ES Hellman, DG Schlom, N Missert, K Char, JS Harris Jr, MR Beasley, A Kapitulnik, TH Gebalie, JN Eckstein, S-L Weng, and C Webb. *Journal of Vacuum Science and Technology B*, **6**:799, 1988.

[27] JN Eckstein, DG Schlom, ES Hellman, KE von Dessonneck, ZJ Chen, C Webb, F Turner, JS Harris Jr, MR Beasley, and TH Gebalie. *Journal of Vacuum Science and Technology B*, **7**:319, 1989.

[28] Y Tokura and N Nagaosa. *Science*, **288**:462, 2000.

[29] G Rispens and B Noheda. *Integrated Ferroelectrics*, **92**:30, 2007.

[30] R Ramesh and NA Spaldin. *Nature Materials*, **6**: 21, 2007.

[31] ME White, MY Tsai, F Wu, and JS Speck. *Journal of Vacuum Science and Technology A*, **26**:1300, 2008.

[32] O Bierwagen, ME White, M-Y Tsai, and JS Speck. *Applied Physics Letters*, **95**:262105, 2009.

[33] M-Y Tsai, O Bierwagen, ME White, and JS Speck. *Journal of Vacuum Science and Technology A*, **28**:354, 2010.

[34] EG Víllora, K Shimamura, K Kitamura, and K Aoki. *Applied Physics Letters*, **88**:031105, 2006.

[35] C Grivas and RW Eason. *Journal of Physics: Condensed Matter*, **20**: 264011, 2008.

[36] YN Xu, ZQ Gu, and WY Ching. *Physical Review B*, **56**:14, 1997.

[37] RWG Wyckoff. *Crystal Structures*. Interscience, 1964.

[38] LJ Sham and M Schlüter. *Physical Review B*, **32**:3883, 1985.

[39] OM Bordun. *Journal of Applied Spectroscopy*, **68**:304, 2001.

[40] PH Klein and WJ Croft. *Journal of Applied Physics*, **38**:1603, 1967.

[41] IC Robin, R Kumaran, S Penson, SE Webster, T Tiedje, and A Oleinik. *Optical Materials*, **30**:835, 2008.

[42] ED Palik. *Handbook of optical constants of solids II*. Academic Press, 1991.

[43] G Teowee, KC McCarthy, FS McCarthy, TJ Bukowski, DG Davis Jr, and DR Uhlmann. *Journal of Sol-Gel Science and Technology*, **13**:895, 1998.

[44] L Lou, W Zhang, A Brioude, C Le Luyer, and J Mugnier. *Optical Materials*, **18**:331, 2001.

[45] T Kim Anh, L Quoc Minh, N Vu, T Thu Huong, N Thanh Huong, C Barthou, and W Strek. *Journal of Luminescence*, **102**:391, 2003.

[46] Y-C Wu, S Parola, O Marty, and J Mugnier. *Optical Materials*, **27**: 21, 2004.

[47] Jun Yeol Cho, Ki-Young Ko, and Young Rag Do. *Thin Solid Films*, **515**:3373, 2007.

[48] Shaoqiang Zhang and Rongfu Xiao. *Journal of Applied Physics*, **83**:3842, 1998.

[49] D Kumar, KG Cho, Zhan Chen, V Craciun, PH Holloway, and Rajiv K Singh. *Physical Review B*, 60:13331, 1999.

[50] RJ Gaboriaud, F Pailloux, and J Perriere. *Applied Surface Science*, 186:477, 2002.

[51] S Bär, G Huber, J Gonzalo, A Perea, A Climent, and F Paszti. *Materials Science and Engineering B*, 105:30, 2003.

[52] S Bär, G Huber, J Gonzalo, A Perea, and M Munz. *Applied Physics A Materials Science & Processing*, 80:209, 2005.

[53] AOG Dikovska, PA Atanasov, M Jiménez de Castro, A Perea, J Gonzalo, CN Afonso, and J García López. *Thin Solid Films*, 500: 336, 2006.

[54] Xuerui Cheng, Zeming Qi, Guobin Zhang, Hongjun Zhou, Weiping Zhang, and Min Yin. *Physica B*, 404:146, 2009.

[55] SN Bagayev, VV Osipov, MG Ivanov, VI Solomonov, VV Platonov, AN Orlov, AV Rasuleva, and SM Vatnik. *Optical Materials*, 31: 740, 2009.

[56] JH Mun, A Jouini, A Novoselov, Y Guyot, A Yoshikawa, H Ohta, H Shibata, Y Waseda, G Boulon, and T Fukuda. *Optical Materials*, 29:1390, 2007.

[57] Hai Guo and Yan Min Qiao. *Optical Materials*, 31:583, 2009.

[58] RJ Gaboriaud, F Pailloux, P Guerin, and F Paumier. *Thin Solid Films*, 400:106, 2001.

[59] Trinh Tu Van and Jane P Chang. *Applied Physics Letters*, 87: 011907, 2005.

[60] Hirofumi Fukumoto, Takeshi Imura, and Yukio Osaka. *Applied Physics Letters*, 55:360, 1989.

[61] J Kwo, M Hong, AR Kortan, KT Queeney, YJ Chabal, JP Mannaerts, T Boone, JJ Krejewski, AM Sergent, and JM Rosamilia. *Applied Physics Letters*, 77:180, 2000.

[62] J Kwo, M Hong, AR Kortan, KL Queeney, YJ Chabal, RL Opila Jr, DA Muller, SNG Chu, BJ Sapjeta, TS Lay, JP Mannaerts, T Boone, HW Krautter, JJ Krajewski, AM Sergnt, and JM Rosamilia. *Journal of Applied Physics*, 89:3920, 2001.

[63] M-H Cho, D-H Ko, YK Choi, IW Lyo, K Jeong, TG Kim, JH Song, and CN Whang. *Journal of Applied Physics*, **89**:1647, 2001.

[64] M-H Cho, D-H Ko, YK Choi, IW Lyo, K Jeong, and CN Whang. *Thin Solid Films*, **402**, 2002.

[65] G Apostolopoulos, G Vellianitis, A Dimoulas, M Alexe, R Scholz, M Fanciulli, DT Dekadjevi, and C Wiemer. *Applied Physics Letters*, **81**:3549, 2002.

[66] CW Nieh, YJ Lee, WC Lee, ZK Yang, AR Kortan, M Hong, J Kwo, and C-H Hsu. *Applied Physics Letters*, **92**:061914, 2008.

[67] YJ Lee, WC Lee, CW Nieh, ZK Yang, AR Kortan, M Hong, J Kwo, and C-H Hsu. *Journal of Vacuum Science and Technology B*, **26**: 1124, 2008.

[68] C Borschel, C Ronning, H Hofsäss, A Giussani, P Zaumseil, Ch. Wenger, P Storck, and T Schroeder. *Journal of Vacuum Science and Technology B*, **27**:305, 2009.

[69] M Tsuchiya, N Bojarczuk, S Guha, and S Ramanathan. *Philosophical Magazine*, **90**:1123, 2010.

[70] WH Chang, P Chang, WC Lee, TY Lai, J Kwo, C-H Hsu, JM Hong, and M Hong. *Journal of Crystal Growth*, **323**:107, 2011.

[71] Wei Li, SE Webster, R Kumaran, S Penson, and T Tiedje. *Applied Optics*, **49**:586, 2010.

[72] SE Webster, R Kumaran, S Penson, and T Tiedje. *Journal of Vacuum Science and Technology B*, **28**:C3A20, 2010.

[73] BD Cullity. *Elements of x-ray diffraction*. Addison-Wesley, 2nd edition, 1978.

[74] E Chason and TM Mayer. *Critical Reviews in Solid State & Materials Sciences*, **22**:1, 1997.

[75] L Pham Van, O Kurnosikov, and J Cousty. *Surface Science*, **411**: 263, 1998.

[76] O Kurnosikov, L Van, and J Cousty. *Surface and Interface Analysis*, **29**:608, 2000.

[77] SC Wang and Gert Ehrlich. *Physical Review Letters*, **67**:2509, 1991.

[78] E Copland. *Journal of Chemical Thermodynamics*, **38**:443, 2006.

[79] CW Park, DY Yoon, JE Blendell, and CA Handwerker. *Journal of the American Ceramic Society*, **86**:603, 2003.

[80] JR Vig. Ultraviolet-ozone cleaning of semiconductor surfaces. In W Kern, editor, *Handbook of semiconductor wafer cleaning technology*, pages 233–273. Noyes Publications, 1993.

[81] M Suzuki, S Aoyama, T Futatsuki, AJ Kelly, T Osada, A Nakano, Y Sakakibara, Y Suzuki, H Takami, T Takenobu, and M Yasutake. *Journal of Vacuum Science and Technology A*, **14**:1228, 1996.

[82] RS Goldman, KL Kavanagh, HH Wieder, SN Ehrlich, and RM Feenstra. *Journal of Applied Physics*, **83**:5137, 1998.

[83] N Zangenberg, DA Beaton, T Tiedje, S Tixier, M Adamcyk, R Kumaran, JA MacKenzie, E Nodwell, EC Young, and GI Sproule. *Journal of Vacuum Science and Technology A*, **25**:850, 2007.

[84] JH Weaver, C Krafka, DW Lynch, and EE Koch. *Physics data: optical properties of metals*, volume 1. Fachinformationszentrum Energie, Physik, Mathematik GmbH, 1981.

[85] R Kumaran, SE Webster, S Penson, Wei Li, and T Tiedje. *Journal of Crystal Growth*, **311**:2191, 2009.

[86] YS Touloukian and DP DeWitt. *Thermophysical Properties of Matter*, volume 8. IFI/Plenum Press, 1972.

[87] J Humlíček. Polarized light and ellipsometry. In HG Tompkins and EA Irene, editors, *Handbook of Ellipsometry*, pages 3–91. William Andrew, 2005.

[88] T Lichtenstein. *Handbook of Thin Film Materials*. Academic Press, 1972.

[89] N Chand, R People, FA Baiocchi, KW Wecht, and AY Cho. *Applied Physics Letters*, **49**:815, 1986.

[90] ON Carlson. *Bulletin of Alloy Phase Diagrams*, **11**: 61, 1990.

[91] Iwao Teramoto. *Japanese Journal of Applied Physics*, **17**:103, 1978.

[92] *Inorganic Crystal Structure Database*, 2011, FIZ Karlsruhe Leibniz Institute for Information Infrastructure. URL http://www.fiz-karlsruhe.de

[93] O Yamaguchi, K Takeoka, K Hirota, H Takano, and A Hayashida. *Journal of Materials Science*, **27**:1261, 1992.

[94] B Walsh, JM McMahon, WC Edwards, NP Barnes, RW Equall, and RL Hutcheson. *Journal of the Optical Society of America B*, **19**: 2893, 2002.

[95] MRJ Gibbs, JE Evetts, and JA Leake. *Journal of Materials Science*, **18**:278, 1983.

[96] EG Moya, F Moya, B Lesage, MK Loudjani, and C Grattepain. *Journal of the European Ceramic Society*, **18**:591, 1998.

[97] RJ Gaboriaud. *Journal of Solid State Chemistry*, **35**:252, 1980.

[98] M LeGall, B Lesage, and J Bernardini. *Philosophical Magazine A*, **70**:761, 1994.

[99] Toshio Maruyama and Wazo Komatsu. *Journal of the American Ceramic Society*, **58**:338, 1975.

[100] G Triantafyllou, GN Angelopoulos, and P Nikolopoulos. *Journal of Materials Science*, **45**:2015, 2010.

[101] LG Parratt. *Physical Review*, **95**:359, 1954.

[102] PF Fewster. *X-ray Scattering from Semiconductors*. World Scientific, 2nd edition, 2003.

[103] A-L Barabási and HE Stanley. *Fractal Concepts in Surface Growth*. Cambridge University Press, 1995.

[104] JW Matthews and AE Blakeslee. *Journal of Crystal Growth*, **27**: 118, 1974.

[105] M Becht, F Wang, JG Wen, and T Morishita. *Journal of Crystal Growth*, **170**:799, 1997.

[106] X Castel, M Guilloux-Viry, A Perrin, J Lesueur, and F Lalu. *Journal of Crystal Growth*, **187**:211, 1998.

[107] AG Zaitsev, G Ockenfuss, D Guggi, R Wördenweber, and U Krüger. *Journal of Applied Physics*, **81**:3069, 1997.

[108] A Boulle, O Masson, R Guinebretière, and A Dauger. *Thin Solid Films*, **434**:1, 2003.

[109] A Boulle, F Conchon, and R Guinebretière. *Acta Crystallographica A*, **62**: 11, 2005.

[110] PF Miceli and CJ Palmstrøm. *Physical Review B*, **51**:5506, 1995.

[111] RI Barabash, W Donner, and H Dosch. *Applied Physics Letters*, **78**:443, 2001.

[112] VM Kaganer, R Köhler, M Schmidbauer, R Opitz, and B Jenichen. *Physical Review B*, **55**:1793, 1997.

[113] Vladimir M Kaganer and Karl K Sabelfeld. *Physical Review B*, **80**: 184105, 2009.

[114] N Herres, F Fuchs, J Schmitz, KM Pavlov, J Wagner, JD Ralston, P Koidl, C Gadaleta, and G Scamarcio. *Physical Review B*, **53**: 15688, 1996.

[115] S Takagi. *Journal of the Physical Society of Japan*, **26**:1239, 1969.

[116] D Taupin. *Bulletin de la Société Française de Minéralogie et de Cristallographie*, **87**:469, 1964.

[117] WJ Bartels, J Hornstra, and DJW Lobeek. *Acta Crystallographica A*, **42**:539, 1986.

[118] H Cole and NR Stemple. *Journal of Applied Physics*, **33**:2227, 1962.

[119] A Fingerland. *Acta Crystallographica A*, **27**:280, 1971.

[120] M Copel, MC Reuter, M Horn von Hoegen, and RM Tromp. *Physical Review B*, **42**:11682, 1990.

[121] S Tixier, M Adamcyk, EC Young, JH Schmid, and T Tiedje. *Journal of Crystal Growth*, **251**:449, 2003.

[122] Zhenyu Zhang and Max G Lagally. *Physical Review Letters*, **72**: 693, 1994.

[123] Lorne M Chanin and RD Steen. *Physical Review*, **132**:2554, 1963.

[124] Benjamin L Lev. *Magnetic microtraps for cavity QED, Bose-Einstein condensates, and atom optics*. PhD thesis, California Institute of Technology, 2006.

[125] R Kumaran, SE Webster, S Penson, Wei Li, T Tiedje, Peng Wei, and F Schiettekatte. *Optics Letters*, **34**:3358, 2009.

[126] R Kumaran, T Tiedje, SE Webster, S Penson, and Wei Li. *Optics Letters*, **35**:3793, 2010.

[127] M Yamaga, T Ishikawa, M Yoshida, T Hasegawa, EG Víllora, and K Shimamura. *physica status solidi c*, **8**:2621, 2011.

[128] R Rao, AM Rao, B Xu, J Dong, S Sharma, and MK Sunkara. *Journal of Applied Physics*, **98**:094312, 2005.

[129] Feng Zhu, Zhong Xue Yang, Wei Min Zhou, and Ya Fei Zhang. *Solid State Communications*, **137**:177, 2006.

[130] Emilio Nogales, José Ángel García, Bianchi Méndez, and Javier Piqueras. *Applied Physics Letters*, **91**:133108, 2007.

A Aluminum oxide

Sapphire, or Al_2O_3, is a commonly used substrate material and useful for many purposes. Homoepitaxy is a logical goal for MBE. I grew several Al_2O_3 films on C-plane sapphire substrates. Al_2O_3 proved to be more difficult to grow epitaxially than Y_2O_3. Films were successfully deposited with substrate temperatures between 600 °C and 1000 °C.

X-ray results from these samples are difficult to analyze because there is no difference between "perfect" growth and no growth at all; these results, therefore, were inconclusive. However, films *were* deposited as evidenced by changes seen in RHEED and AFM measurements, and by visual inspection. RHEED images showed rings, indicating polycrystalline growth. The films were likely porous, as they appeared cloudy. Subsequent to this work, Raveen Kumaran was able to grow high-quality single-crystal Al_2O_3 films. See reference [125] for details.

Al_2O_3 films were also deposited using the electron-beam evaporator system. Crystalline Al_2O_3 granules were heated using the electron beam and evaporated onto unheated glass substrates. Initial films had a brown tint. Annealing in air at temperatures around 1150 °C or introducing O_2 at pressures around 1×10^{-6} torr into the evaporation chamber during deposition caused the film to become clear. The films had an RMS roughness of 4 nm which increased to 16 nm after annealing, despite the AFM image appearing to be qualitatively smoother. Figure 66 shows AFM images of a film taken after e-beam deposition and after annealing.

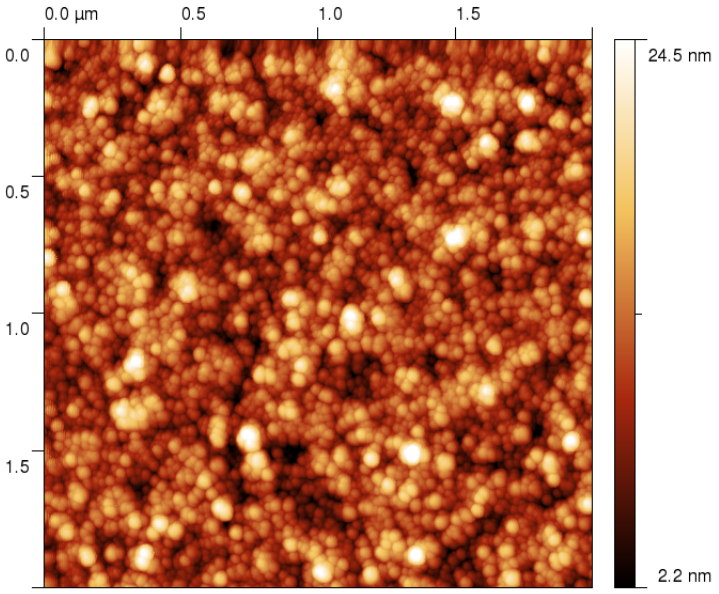

(a) Before

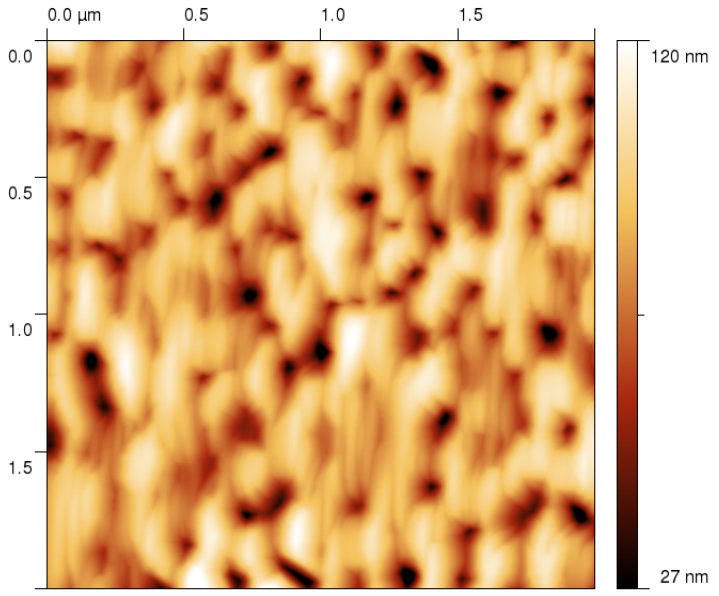

(b) After

Figure 66: AFM images of an electron-beam-deposited Al_2O_3 film (a) before and (b) after annealing at 1150 °C for several hours.

B Gallium oxide

Gallium oxide is a material with a wide range of potential uses, including in optics and as both a dielectric and transparent conductor, depending on sample preparation.[34, 127] Attempts were made to grow gallium oxide on C- and R-plane sapphire. AFM results confirmed the presence of a film. Growth temperatures of 600 °C or lower were required for a film to "stick." The use of the plasma source with oxygen and hydrogen also seemed to aid in film formation. After it proved difficult to achieve a high quality image with an AFM, measurements were made using a Hitachi S-4700 field-emission scanning electron microscope (SEM). The images showed nanowire structures as seen in figure 67. Nanowires are difficult to view properly with AFM because of their sharp features. β-Ga_2O_3 nanowires have been reported previously.[128–130] RHEED spots from our samples indicated a least some crystallinity, but x-ray diffraction measurements were inconclusive, with some films showing small peaks and others exhibiting no signs of crystallinity.

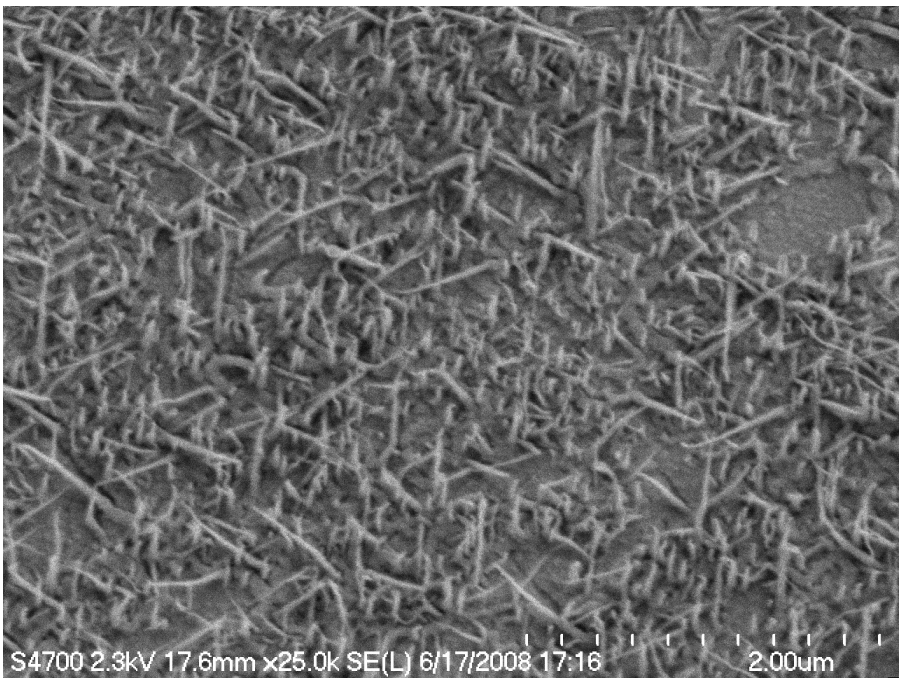

Figure 67: SEM image of a gallium oxide film showing nanowire structures. The wires appear to be tens of nanometres wide and up to several hundred nanometres long.

C Dynamical diffraction code

The source code for the computer program described in section 4.3 is reproduced below. The program was compiled using Python 2.5. The simulation is run by preparing a file containing input parameters and then specifying that file on the command line when invoking the program. An example parameter file follows the main program code. The code comments in green text provide additional specific details of the implementation of the algorithm.

```
#! /usr/bin/python
#
# This program performs dynamical x-ray simulations.
# It was written so that we could simulate oxide materials.
# Some inspiration from code (bartels.cpp)
# received from James Gupta at NRC on Oct. 28, 2009
#
# References:
# Bartels, W.J. et al., Acta Cryst. A42, p539 (1986).
# Wormington, M. et al., Phil. Trans. R. Soc. Lond. A, 357, p2827 (1999).
# Taupin, D., Bull. Soc. Franc. Miner. Crist., 87, p469 (1964).
#
# Scott Webster
# September 12, 2011
#
# Supply sample data file as first command line argument
# see sample.py for an example file, eg.:
# ./dynamical.py sample.py > output.txt

# Import required things, use complex math functions
from __future__ import division
from __future__ import with_statement
from math import *
from cmath import *
import sys

# Trivial class to create a crystal layer data type
class crystal:
    pass

substrate = crystal()
epi = crystal()

# Import simulation parameters from command line specified file
# See example.py for instructions
with open(sys.argv[1], 'r') as inputs:
    exec inputs

# Function to calculate the atomic scattering factor for a specific angle,
# wavelength and ion using Cromer and Mann fit, see ref below
def cromermann(theta, wavel, ff):
    f0 = 0
    for i in range(4):
        f0 += ff[2*i]*exp(-ff[2*i+1]*(sin(theta)/wavel)**2)
```

```
    f0 += ff[8]
    return f0

# Cromer-Mann coefficients (Acta Cryst A24 321) and anomalous
# scattering factors from
# http://skuld.bmsc.washington.edu/scatter/AS_form.html
# Anomalous values only for Cu Ka1!
# Assumed "O1-" data from paper was typo and should be "O2-
# Bi and In from http://www.ruppweb.org/Xray/comp/scatfac.htm
# Format:
# A1, B1, A2, B2, A3, B3, A4, B4, C, f', f''
# Note that the atomic form factor f = f0 + f' + jf''
formfactors = {
    'Y' : [[19.0567, 1.24615, 6.50783, 9.68019, 4.81524,
            18.8903, 2.84786, 121.353, 5.76121], -0.326, 1.948],
    'Y3+' : [[18.4202, 1.34457, 9.75213, 12.0631, 1.05270,
              25.1684, -33.4755, -0.01023, 40.2513], -0.326, 1.948],
    'O' : [[2.95648, 13.8964, 2.45240, 5.91765, 1.50510,
            0.34537, 0.78135, 34.0811, 0.30413], 0.04915, 0.03176],
    'O2-' : [[3.22563, 18.4991, 3.01717, 6.65680, 1.42553,
              0.40589, 0.90525, 61.1889, 0.42362], 0.04915, 0.03176],
    'Al' : [[5.35047, 3.48665, 2.92451, 1.20535, 2.27309,
             42.6051, 1.16531, 107.170, 1.28489], 0.2106, 0.2438],
    'Al3+' : [[4.17448, 1.93816, 3.38760, 4.13553, 1.20296,
               0.22875, 0.52814, 8.28524, 0.70679], 0.2106, 0.2438],
    'Ga' : [[15.3412, 3.63868, 5.74150, 0.65640, 3.10733,
             16.0719, 2.52764, 70.7609, 4.26842], -1.340, 0.7272],
    'As' : [[15.4043, 3.07517, 6.13723, 0.74113, 3.74679,
             21.0014, 3.01390, 57.7446, 4.69149], -0.9891, 0.9613],
    'Bi' : [[33.369, 0.704, 12.951, 2.924, 16.588,
             8.794, 6.469, 48.009, 13.578], -4.062, 8.755],
    'In' : [[19.162, 0.548, 18.560, 6.378, 4.295,
             25.850, 2.040, 92.803, 4.939], 0.01226, 5.005],
    'Nd3+' : [[49.4292, 0.05936, 23.6116, 2.48611, 11.6190,
               14.9366, 1.68986, 28.4515, -29.3493], -3.378, 10.66]}

# Functions to calculate cubic and hexagonal d-spacings and cell volumes
def cubicspacing(a,hkl):
    return sqrt(a**2/(hkl[0]**2+hkl[1]**2+hkl[2]**2))
def hexspacing(a,c,hkl):
    return sqrt(1/(4/3*((hkl[0]**2+hkl[0]*hkl[1]+hkl[1]**2)/a**2)
                   +hkl[2]**2/c**2))
def tetspacing(a,c,hkl):
    return sqrt(1/(((hkl[0]**2+hkl[1]**2)/a**2)+hkl[2]**2/c**2))
def rhomspacing(a,alphadeg,hkl):
    alpha = radians(alphadeg)
    return sqrt(1/(((hkl[0]**2+hkl[1]**2+hkl[2]**2)*sin(alpha)**2
                    +2*(hkl[0]*hkl[1]+hkl[1]*hkl[2]+hkl[0]*hkl[2])
                    *(cos(alpha)**2-cos(alpha)))
                   /(a**2*(1-3*cos(alpha)**2+2*cos(alpha)**3))))
def cubicvolume(a):
    return a**3
def hexvolume(a,c):
    return 0.866*c*a**2
def tetvolume(a,c):
    return a*a*c
def rhomvolume(a,alphadeg):
    alpha = radians(alphadeg)
    return (a**3)*sqrt(1-3*cos(alpha)**2+2*cos(alpha)**3)

# Functions to calculate various structure factors
```

```
# These functions look up the scattering factors based on the atom specified
# in the uvw file.  If you want to use the ion values, specify the ion in the
# uvw file.  This is unlikely to make a large difference however.
# Note that the bragg angle of the _layer_ is used for this calculation
# and that this value is used for all data points regardless of actual angle
# Does this make sense?
# Note that we define the structure factor as follows:
# F = F' + jF''
# Note that F' and F'' are both complex.  F' is calculated by ignoring the
# imaginary part of the anomalous scattering (f'' = 0) and F'' is calculated
# using by ignoring the real parts of the scattering factor (normal and
# anomalous (so f0 = f' = 0).
# See Bartels, and their reference, Cole and Stemple.
# F0 is just the number of electrons in the unit cell plus the anomalous
# scattering factor (real and imaginary).  This is equivalent to setting the
# plane to [0,0,0] and the angle to 0.
# F0 has to do with refraction and absorption (Bartels).

# This first function calculates F' the "real" part of the structure factor.
def structfreal(wavel, layer):
    with open(layer.uvwfile, 'r') as f:
        uvw = f.readlines()
    # remove header lines
    del uvw[0]
    del uvw[0]
    sf = 0
    # Loop over lines in data file, one atom per line
    for line in uvw:
        atom = line.split()
        phase = 2*pi*(layer.plane[0]*(float(atom[1]))
                     +layer.plane[1]*(float(atom[2]))
                     +layer.plane[2]*(float(atom[3])))
        # Note that we don't add the imaginary part of the anomalous scattering
        if layer == epi and epi.weighted == 'true' and atom[0] == epi.subatom:
            sf += ((1-epi.otherweight)*\
                  (cromermann(layer.bragg, wavel, formfactors[atom[0]][0])\
                   +formfactors[atom[0]][1])\
                  +epi.otherweight*\
                  (cromermann(layer.bragg, wavel,\
                              formfactors[epi.otheratom][0])\
                   +formfactors[epi.otheratom][1]))*exp(1j*phase)
        else:
            sf += (cromermann(layer.bragg, wavel, formfactors[atom[0]][0])
                   +formfactors[atom[0]][1])*exp(1j*phase)
    return sf

# This second function calculates F'' the "imaginary" part
def structfcomplex(wavel, layer):
    with open(layer.uvwfile, 'r') as f:
        uvw = f.readlines()
    # remove header lines
    del uvw[0]
    del uvw[0]
    sf = 0
    # Loop over lines in data file, one atom per line
    for line in uvw:
        atom = line.split()
        phase = 2*pi*(layer.plane[0]*(float(atom[1]))
                     +layer.plane[1]*(float(atom[2]))
                     +layer.plane[2]*(float(atom[3])))
        # Now we ONLY have the imaginary part of the anomalous scattering
```

```
        # Note that f'' (a real value) is NOT multiplied by j here
        # since, as stated above, F = F' + jF''
        if layer == epi and epi.weighted == 'true' and atom[0] == epi.subatom:
            sf += ((1-epi.otherweight)*(formfactors[atom[0]][2])\
                   +epi.otherweight*(formfactors[epi.otheratom][2]))\
                   *exp(1j*phase)
        else:
            sf += (formfactors[atom[0]][2])*exp(1j*phase)
    return sf

# This third function calculates F0 (see above)
def structfzero(wavel, layer):
    with open(layer.uvwfile, 'r') as f:
        uvw = f.readlines()
    # remove header lines
    del uvw[0]
    del uvw[0]
    sf = 0
    # Loop over lines in data file, one atom per line
    for line in uvw:
        atom = line.split()
        # Now the phase factor is 0 so the exp term in the structure
        # factor is just 1, so we don't have to multiply by it
        # Note that now f'' IS being multiplied by j since F0 is
        # never broken up into "real" and "imaginary" parts.
        if layer == epi and epi.weighted == 'true' and atom[0] == epi.subatom:
            sf += (1-epi.otherweight)\
                  *(cromermann(0, wavel, formfactors[atom[0]][0])\
                    +formfactors[atom[0]][1]+1j*formfactors[atom[0]][2])\
                  +epi.otherweight\
                  *(cromermann(0, wavel, formfactors[epi.otheratom][0])\
                    +formfactors[epi.otheratom][1]+1j*formfactors[epi.otheratom][2])
        else:
            sf += cromermann(0, wavel, formfactors[atom[0]][0])\
                  +formfactors[atom[0]][1]+1j*formfactors[atom[0]][2]
    return sf

# X-ray wavelength in angstroms
wavel = 1.540562
# Classical electron radius in angstroms
radius = 2.818e-5
# Beam polarization, sigma = perp, pi = parallel, doesn't really do much
# random polarization is arithmetic average of both ((sigcase + picase)/2)
pol = 'sigma'
#pol = 'pi'
# symmetry of reflection b = gamma_0/gamma_H
# gammas are cosines of beam angle wrt surface normal
# so -1 for a symmetric reflection
symm = -1

# Calculate some more required parameters based on input file
if substrate.type =='cubic':
    substrate.volume = cubicvolume(substrate.a)
    substrate.dspacing = cubicspacing(substrate.a, substrate.plane)
elif substrate.type == 'hexagonal':
    substrate.volume = hexvolume(substrate.a, substrate.c)
    substrate.dspacing = hexspacing(substrate.a, substrate.c, substrate.plane)
elif substrate.type == 'tetragonal':
    substrate.volume = tetvolume(substrate.a, substrate.c)
    substrate.dspacing = tetspacing(substrate.a, substrate.c, substrate.plane)
elif substrate.type == 'rhombohedral':
```

```
    substrate.volume = rhomvolume(substrate.a, substrate.alpha)
    substrate.dspacing = rhomspacing(substrate.a, substrate.alpha,
                                     substrate.plane)

if epi.type == 'cubic':
    epi.volume = cubicvolume(epi.a)
    epi.dspacing = cubicspacing(epi.a, epi.plane)
elif epi.type == 'hexagonal':
    epi.volume = hexvolume(epi.a, epi.c)
    epi.dspacing = hexspacing(epi.a, epi.c, epi.plane)
elif epi.type == 'tetragonal':
    epi.volume = tetvolume(epi.a, epi.c)
    epi.dspacing = tetspacing(epi.a, epi.c, epi.plane)
elif epi.type == 'rhombohedral':
    epi.volume = rhomvolume(epi.a, epi.alpha)
    epi.dspacing = rhomspacing(epi.a, epi.alpha, epi.plane)

# gamma is a factor defined in the Bartels paper
substrate.gamma = radius*wavel**2/pi/substrate.volume
substrate.bragg = asin(wavel/2/substrate.dspacing)
# Bragg angles
epi.gamma = radius*wavel**2/pi/epi.volume
epi.bragg = asin(wavel/2/epi.dspacing)

# Calculate the structure factors for the layers
# As explained in the comment above, these don't vary with angle,
# so we only need to calculate them once.
# F0 factors for substrate and epilayer (s and e)
F0s = structfzero(wavel, substrate)
F0e = structfzero(wavel, epi)
# Structure factors for substrate actual diffracting plane, p for prime (')
FHsp = structfreal(wavel,substrate)
FHspp = structfcomplex(wavel, substrate)
FHep = structfreal(wavel, epi)
FHepp = structfcomplex(wavel, epi)

# Define kappa for subs and epilayer
kappas = abs(FHspp/FHsp)
kappae = abs(FHepp/FHep)

# In Bartels, (FHFHbar)^(1/2) has a special meaning, defined later in the paper
# In the case of a centrosymmetric reflection we have, for subs and epi:
FHFHbarroots = abs(FHsp)*(1+1j*kappas)
FHFHbarroote = abs(FHep)*(1+1j*kappae)

# Loop over all angles in the simulation
# Each time we output one data point: angle, intensity
angles = [starttheta+stepsize*i for i in range(numsteps)]
for theta in angles:

    # SUBSTRATE

    # determine polarization factor C
    if pol == 'sigma':
        C = 1
    else:
        C = abs(cos(2*substrate.bragg))

    # Refraction correction, quite small
    deltatheta0 = (0.5*substrate.gamma*F0s.real/sin(2*substrate.bragg)
                   *(1+abs(1/symm)))
```

```
    # Calculate eta value, defined in Bartels paper
    eta = ((-symm*(theta-substrate.bragg-deltatheta0)*sin(2*substrate.bragg)
           -0.5*substrate.gamma*F0s*(1-symm))
           /(sqrt(abs(symm))*C*substrate.gamma*FHFHbarroots))

    # Use eqn. 9 from Bartels for the initial substrate X value,
    # sign is opposite of eta.real
    # assumes infinitely thick substrate
    if eta.real < 0:
        X = eta + sqrt(eta**2-1)
    else:
        X = eta - sqrt(eta**2-1)

    # EPILAYER

    # determine polarization factor C
    if pol == 'sigma':
        C = 1
    else:
        C = abs(cos(2*epi.bragg))

    # Refraction correction
    deltatheta0 = 0.5*epi.gamma*F0e.real/sin(2*epi.bragg)*(1+abs(1/symm))

    # Calculate eta and other values defined in paper for epilayer, using
    # substrate X
    # Note use of epilayer Bragg angle in eta and T...
    eta = ((-symm*(theta-epi.bragg-deltatheta0)*sin(2*epi.bragg)
            -0.5*epi.gamma*F0e*(1-symm))
           /(sqrt(abs(symm))*C*epi.gamma*FHFHbarroote))
    T = (pi*C*epi.gamma*FHFHbarroote*epi.thickness/
         (wavel*sqrt(sin(epi.bragg)*sin(epi.bragg))))
    S1 = (X-eta+sqrt(eta**2-1))*exp(-1j*T*sqrt(eta**2-1))
    S2 = (X-eta-sqrt(eta**2-1))*exp(1j*T*sqrt(eta**2-1))

    # Now calculate X for this layer using the recursion relation
    # If we had another layer this would be the input X value instead of the
    # substrate
    X = eta+sqrt(eta**2-1)*((S1+S2)/(S1-S2))

    # Write x-ray intensity to stdout, for centrosymmetric reflections
    # this is just the magnitude of X squared
    print degrees(theta), abs(X)**2
```

Example input file follows.

```
# This is an example input file for dynamical.py
# Scott Webster, October 12, 2011
# The following variables can be defined for the simulation...
# choose the appropriate ones...

substrate.type = 'cubic'
substrate.type = 'tetragonal'
substrate.type = 'hexagonal'
substrate.type = 'rhombohedral'
# (applicable) lattice parameters in angstroms or degrees for angles
# angle required for rhombohedral lattices
substrate.a = 1.234
substrate.c = 1.234
substrate.alpha = 12.345
substrate.plane = [0, 1, 2]
```

```
# uvw file containing atom positions, expects 2 header lines
# then lines containing: Atom_Symbol uvw
substrate.uvwfile = 'al2o3-hex.uvw'

epi.type = 'cubic'
epi.type = 'tetragonal'
epi.type = 'hexagonal'
epi.type = 'rhombohedral'
epi.a = 1.234
epi.c = 1.234
epi.alpha = 12.345
epi.plane = [2, 2, 2]
epi.uvwfile = 'y2o3.uvw'
# epilayer thickness in angstroms
epi.thickness = 210
# epilayer form factor weighting, subatom is the one from the uvw file to replace
# otheratom is what to replace it with, and otherweight is the fraction of the otheratom
# (so 1-otherweight is the fraction of the original specified atom)
# So in this example the form factor used for the cation will be a weighted average of
# the form factors for Y and Al, with 87% weighting for Y and 13% weighting for Al
epi.weighted = 'true'
epi.subatom = 'Y'
epi.otheratom= 'Al'
epi.otherweight = 0.13

# Set up the simulation size, as you can see, the angles are in radians
starttheta = 11.0/180*3.14159
stepsize = 0.001/180*3.14159
numsteps = 5000
```

D Substrate holder

Figures 68 and 69 show drawings of the substrate holder used for the film growths in this thesis. The holder is designed for (10.0 ± 0.2) mm square substrates. The substrate is attached to the holder by passing a length of Ta or W wire through each pair of holes at the corners and twisting the ends of the wire together underneath. The raised platform the substrate sits on is designed to decrease the chance of the RHEED beam being blocked by the holder. A Ta heat shield can be spot welded to the surface as shown in figure 25. This will reduce heater power consumption by approximately 10% at a substrate temperature of 800 °C. The back of the holder will likely need to be thinned at the spot weld locations for successful attachment.

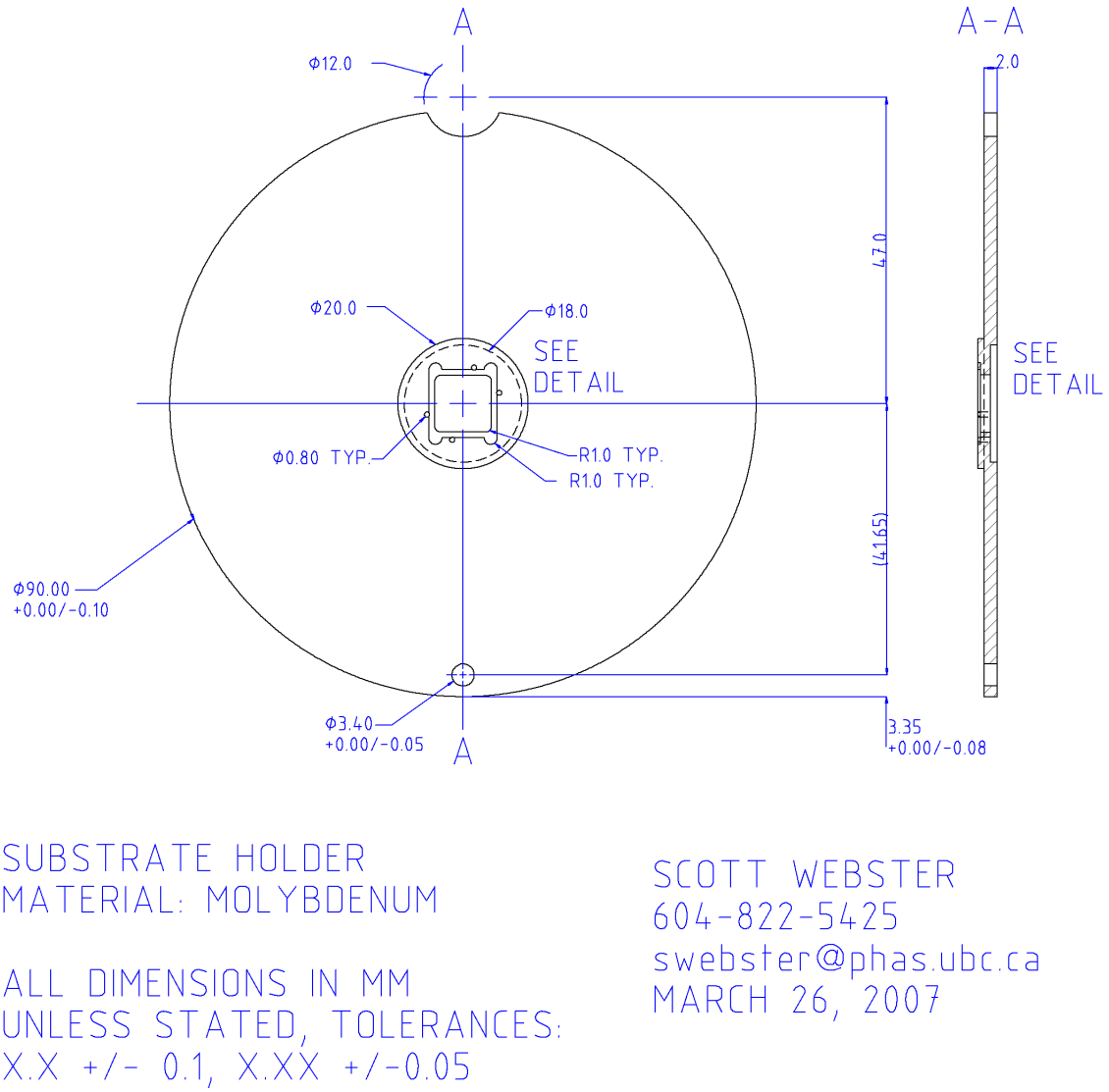

Figure 68: Drawing of the substrate holder. See figure 69 for the detail portion.

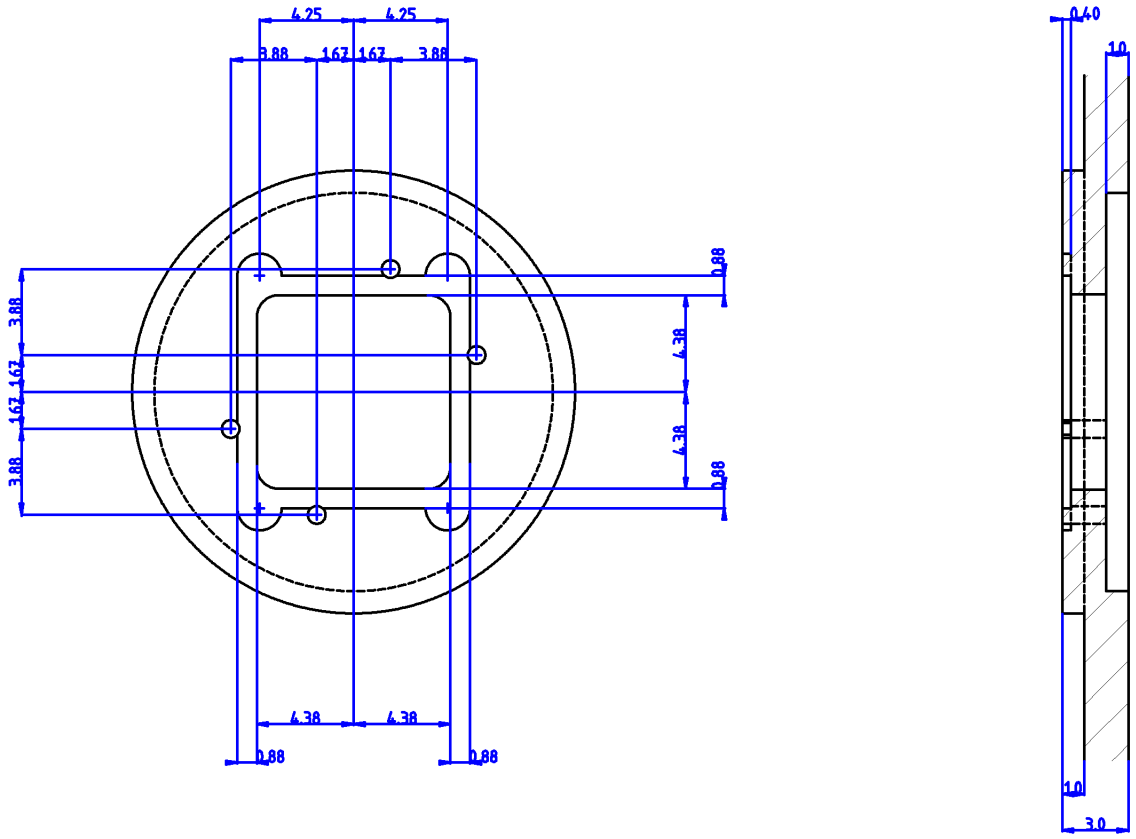

Figure 69: Detail for the substrate holder drawing in figure 68.